Uenzelmann-Neben, G., Bohaty, S.M., Childress, L.B., and the Expedition 392 Scientists
Proceedings of the International Ocean Discovery Program Volume 392
publications.iodp.org

Expedition 392 methods[1]

G. Uenzelmann-Neben, S.M. Bohaty, L.B. Childress, O.A. Archontikis, S.J. Batenburg, P.K. Bijl, A.M. Burkett, H.C. Cawthra, P. Chanda, J.J. Coenen, E. Dallanave, P.C. Davidson, K.E. Doiron, J. Geldmacher, D. Gürer, S.J. Haynes, J.O. Herrle, Y. Ichiyama, D. Jana, M.M. Jones, C. Kato, D.K. Kulhanek, J. Li, J. Liu, J. McManus, A.N. Minakov, D.E. Penman, C.J. Sprain, A.C. Tessin, T. Wagner, and T. Westerhold[2]

[1] Uenzelmann-Neben, G., Bohaty, S.M., Childress, L.B., Archontikis, O.A., Batenburg, S.J., Bijl, P.K., Burkett, A.M., Cawthra, H.C., Chanda, P., Coenen, J.J., Dallanave, E., Davidson, P.C., Doiron, K.E., Geldmacher, J., Gürer, D., Haynes, S.J., Herrle, J.O., Ichiyama, Y., Jana, D., Jones, M.M., Kato, C., Kulhanek, D.K., Li, J., Liu, J., McManus, J., Minakov, A.N., Penman, D.E., Sprain, C.J., Tessin, A.C., Wagner, T., and Westerhold, T., 2023. Expedition 392 methods. In Uenzelmann-Neben, G., Bohaty, S.M., Childress, L.B., and the Expedition 392 Scientists, Agulhas Plateau Cretaceous Climate. Proceedings of the International Ocean Discovery Program, 392: College Station, TX (International Ocean Discovery Program). https://doi.org/10.14379/iodp.proc.392.102.2023
[2] **Expedition 392 Scientists' affiliations.**

Contents

Keywords
International Ocean Discovery Program, IODP, *JOIDES Resolution*, Expedition 392, Agulhas Plateau Cretaceous Climate, Climate and Ocean change, Earth Connections, Site U1579, Site U1580, Site U1581, Site U1582, Cretaceous/Paleogene boundary, K/Pg boundary, Paleocene/Eocene Thermal Maximum, PETM, large igneous province, LIP, zeolite authigenesis, igneous sill intrusion, Campanian, Oligocene pelagic carbonates, paleoceanography, African–Southern Ocean gateway

Core descriptions

Supplementary material

References (RIS)

MS 392-102
Published 19 August 2023

Funded by NSF OCE1326927

1. Introduction

The procedures and tools employed in coring operations and in the various shipboard laboratories of the R/V *JOIDES Resolution* are documented here. This information applies only to shipboard work described in the Expedition Reports section of the Expedition 392 *Proceedings of the International Ocean Discovery Program* volume. Methods for shore-based analyses of Expedition 392 samples and data will be described in separate individual publications. This section describes procedures and equipment used for drilling, coring, core handling, sample registration, computation of depth for samples and measurements, and the sequence of shipboard analyses. Subsequent sections describe laboratory procedures and instruments in more detail.

Unless otherwise noted, all depths in this volume refer to the core depth below seafloor, Method A (CSF-A), scale, which is equivalent to meters below seafloor (mbsf).

1.1. Operations

1.1.1. Site location and holes

GPS coordinates (WGS84 coordinate system) from precruise site surveys were used to position the vessel at each site. A Knudsen CHIRP 3260 subbottom profiler was used to monitor the seafloor depth on the approach to each site. Once the vessel was positioned at the site, the thrusters were lowered. Dynamic positioning control of the vessel used navigational input from the GPS, weighted by the estimated positional accuracy. The final hole position was the mean position calculated from GPS data collected over a significant portion of the time the hole was occupied.

Drill sites are numbered according to the series that began with the first site drilled by *Glomar Challenger* in 1968. Starting with Integrated Ocean Drilling Program Expedition 301, the prefix "U" designates sites occupied by *JOIDES Resolution*.

When multiple holes are drilled at a site, hole locations are typically offset from each other by ~20 m unless otherwise noted. A letter suffix distinguishes each hole drilled at the same site. The first hole drilled is assigned the site number modified by the suffix "A," the second hole takes the site number and the suffix "B," and so forth. During Expedition 392, ten holes were drilled at four sites (U1579–U1582).

1.1.2. Coring and drilling strategy

The primary coring strategy for Expedition 392 was to core single or stratigraphically overlapping holes through Paleogene and Cretaceous sedimentary sequences to achieve high-resolution paleoceanographic objectives and to core deeper single records with the goal of penetrating deeper sedimentary and basement sequences. At four of the five primary sites, we planned to use the advanced piston corer (APC) system and possibly the half-length APC (HLAPC) system in the upper ~300 m, followed by the extended core barrel (XCB) system to ~600 m CSF-A or basement. The fifth site, Site U1582, called for a single rotary core barrel (RCB) hole to 300 m CSF-A. However, the RCB system was used more than planned (and the APC/XCB system used less than planned) due to the consistency of the formation (Figure **F1**). Site U1579 is the only site with overlapping APC cores in offset holes. At Site U1580, several additional RCB cores were taken in Hole U1580B to provide an additional copy of a critical interval. Logging was planned at four of the five primary sites, including use of the Ultrasonic Borehole Imager (UBI).

1.1.3. *JOIDES Resolution* standard coring systems

The APC and HLAPC coring systems cut soft-sediment cores with minimal coring disturbance relative to other International Ocean Discovery Program (IODP) coring systems and are typically suitable for the upper portion of each hole. After the APC core barrel is lowered through the drill pipe and lands near the bit, the inside of the drill pipe is pressured up until two shear pins that hold the inner barrel attached to the outer barrel fail. The inner barrel then advances into the formation at high speed and cuts a core with a diameter of 6.2 cm (2.44 inches). The driller can detect a successful cut, or "full stroke," from the pressure gauge on the rig floor. The depth limit of the APC system, often referred to as APC refusal, is indicated in two ways: (1) the piston fails to achieve a complete stroke (as determined from the pump pressure reading) because the formation is too hard or (2) excessive force (>60,000 lb; ~267 kN) is required to pull the core barrel out of the formation. When a full stroke is not achieved, additional attempts are typically made. The assumption is that the barrel penetrated the formation by the length of core recovered (nominal recovery of ~100%), so the bit is advanced by that length before cutting the next core. When a full or partial stroke is achieved but excessive force cannot retrieve the barrel, the core barrel is drilled over, meaning that after the inner core barrel is successfully shot into the formation, the drill bit is advanced by the length of the APC barrel (~9.6 m). Typically, nonmagnetic core barrels are used and a downhole orientation tool is deployed, except when refusal appears imminent. Formation temperature measurements can be taken with the advanced piston corer temperature (APCT-3) tool, embedded in the APC coring shoe, at specified intervals. These measurements can be used to obtain temperature gradients and heat flow estimates. Temperature measurements were collected using the APCT-3 tool at Sites U1579 and U1581.

The XCB system is a rotary system with a small cutting shoe that extends below the large rotary APC/XCB bit. The XCB shoe is able to cut a semi-indurated core with less torque and fluid circulation than the larger main bit, optimizing recovery. The XCB cutting shoe (bit) extends ~21.65 cm ahead of the main bit in soft sediment but retracts into the main bit when hard formations are encountered. The resulting cores have a nominal diameter of 5.87 cm (2.312 inches), slightly less than the 6.2 cm diameter of APC cores. XCB cores are often broken (torqued) into biscuits, which are disc-shaped pieces a few to several centimeters long with remolded sediment (including some drilling slurry) interlayering the discs in a horizontal direction and packing the space between the discs and the core liner in a vertical direction. This type of drilling disturbance may give the impression that XCB cores have the same thickness (6.2 cm) as APC cores. As with XCB coring, RCB coring generally leads to drilling disturbance in similar sedimentary material. Switching from coring a hole with the APC/XCB bottom-hole assembly (BHA) to coring a parallel hole with an RCB BHA requires a pipe trip and adds significant time to the coring operations on site.

The RCB system is a conventional rotary coring system suitable for lithified rock material. Like the XCB system, the RCB system cuts a core with a nominal diameter of 5.87 cm. RCB coring was performed with the same core liners used routinely with the APC/XCB soft-sediment systems. The BHA is the lowermost part of the drill string and is typically ~130–170 m long, depending on the coring system used and total drill string length. A typical APC/XCB BHA consists of a drill bit (outside diameter = 11⅞ inches), a bit sub, a seal bore drill collar, a landing saver sub, a modified

top sub, a modified head sub, a nonmagnetic drill collar (for APC/XCB), a number of 8¼ inch (~20.96 cm) drill collars, a tapered drill collar, 6 joints (two stands) of 5½ inch (~13.97 cm) drill pipe, and a crossover sub to the regular 5 inch drill pipe. A typical RCB BHA consists of a drill bit, a bit sub or mechanical bit release (for logging), a modified head sub, an outer core barrel, a modified top sub, a second modified head sub, a number of 8¼ inch drill collars, a tapered drill collar, 2 stands of standard 5½ inch drill pipe, and a crossover sub.

Cored intervals may not be contiguous if separated by intervals drilled but not cored. During Expedition 392, with both the APC/XCB and RCB systems, drilling ahead was applied to acceler-

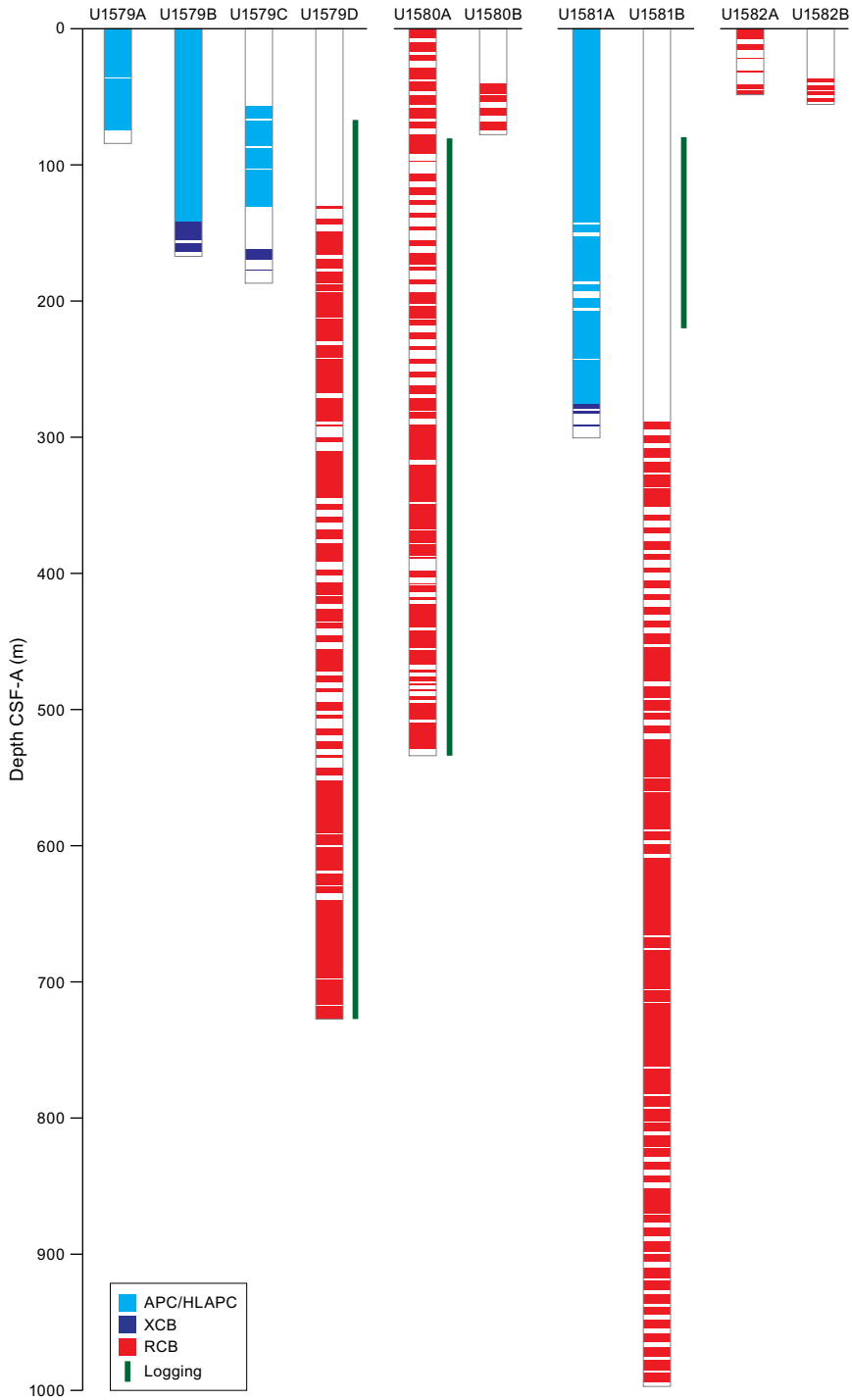

Figure F1. Coring systems used during Expedition 392.

ate penetration because an interval had already been cored in an adjacent hole (Hole U1579C = 93.5 m; Hole U1579D = 130.0 m; Hole U1580B = 40.0 m; Hole U1581B = 289.0 m; Hole U1582B = 36.3 m). Holes therefore consist of a sequence of cored and drilled intervals, or advancements, which are numbered sequentially from the top of the hole downward. Numbers assigned to physical cores correspond to advancements and may not be consecutive.

1.1.4. Drilling disturbance

Cores may be significantly disturbed by the drilling process and can contain extraneous material as a result of the coring and core handling process. In formations with loose granular layers (sand, ash, foraminiferal ooze, chert fragments, shell hash, etc.), drilling activity may allow granular material from intervals higher in the hole to settle and accumulate in the bottom of the hole. Such material could be sampled by the next core; thus, the uppermost 10–50 cm of each core must be assessed for potential fall-in.

Common coring-induced deformation includes the concave-downward appearance of originally horizontal bedding. Piston action may result in fluidization (flow-in) at the bottom of, or sometimes within, APC cores. Retrieval of unconsolidated (APC) cores from depth to the surface typically results to some degree in elastic rebound, and gas that is in solution at depth may become free and drive core segments in the liner apart. When gas content is high, pressure must be relieved for safety reasons before the cores are cut into segments. Holes are drilled into the liner, which forces some sediment and gas out of the liner. As noted above, XCB coring typically results in biscuits mixed with drilling slurry. RCB coring typically homogenizes unlithified core material and often fractures lithified core material.

Drilling disturbances are described in the Lithostratigraphy section of each site chapter and are indicated on graphic core summary reports, also referred to as visual core descriptions (VCDs) (see **Core descriptions**).

1.1.5. Seawater sampling

During Expedition 392, samples for phytoplankton and seawater analysis were collected at each drill site and during transits outside of the South African Exclusive Economic Zone (EEZ) to assess coccolithophorid species assemblage composition. Seawater samples (~20 L) were collected approximately every 6 h at ~0000, 0600, 1200, and 1800 h (all times are provided in local ship time: UTC + 2 h) using a plastic bucket with a nylon rope over the side of the starboard main deck. The sampling depth approximately represents a mixed upper 10 m of surface water. Upon retrieval, temperature and salinity were measured using a thermometer and a reflectometer, respectively, and then the sample was transferred to a 20 L plastic carboy. Latitude and longitude coordinates and the time and date of each collection were recorded (see 392_Plankton_Sampling_Shipboard_-Data.xlsx in SAMPLING in **Supplementary material**).

A 3 mL aliquot of each seawater sample was initially filtered through an Acrodisc syringe nylon filter (diameter = 25 mm; pore size = 0.2 µm) and then transferred to a 14 mL polypropylene round-bottom tube with a cap (Falcon). This aliquot was used for routine shipboard analysis of alkalinity and pH. An additional 15–30 mL split of the seawater sample was sealed in a 60 mL polypropylene round-bottom tube with a cap (Falcon) and stored in a –20°C freezer for postcruise analysis of major anions (sulfate, chloride, and bromide) and nutrients (phosphate, nitrate, and dissolved silica).

For each sampling station, 1 or 2 L of seawater was filtered onto two types of microfilter discs: Whatman cellulose nitrate filters (diameter = 47 mm; pore size = 0.4 µm) and Whatman Nuclepore polycarbonate track-etched filters (diameter = 47 mm; pore size = 0.4 µm). A low-pressure vacuum pump was used for filtration to avoid mechanical breakage of the coccosphere specimens. Salt was removed by washing the filters with ~3 mL of deionized water buffered to a pH of 8.5 with ammonium hydroxide. After filtration, the filters were placed individually in 47 mm plastic Millipore petri dishes and oven-dried at 50°C.

Once dry, a portion of cellulosic filter was cut out and mounted on a glass microscope slide using Norland optical adhesive Number 61 (refractive index = 1.56). Preliminary examination of the

sample was performed using a Zeiss Axiophot microscope with cross-polarized illumination and phase contrast light at 1000× magnification.

The shipboard Hitachi TM3000 scanning electron microscope (SEM) was used for preliminary coccosphere identifications and to identify smaller species that could not be identified using light microscopy. For SEM preparation, a portion of each polycarbonate filter was cut out and mounted onto twelve 10 mm aluminum stubs using double-sided adhesive tape. The stubs were then sputter-coated with gold-palladium for 1–2 min using a Leitz EM ACE2000 sputter coater.

1.2. Core and section handling

1.2.1. Whole core handling

All APC, XCB, and RCB cores recovered during Expedition 392 were extracted from the core barrel in plastic liners. In the case of shattered liners, the cores were initially curated into split liners on the catwalk and then closed using the other half of the liner and taped. All cores were then cut into ≤1.5 m sections. The exact section length was noted and entered into the database as "created length" using the Sample Master application. This number was used to calculate recovery. Subsequent processing differed for soft-sediment, lithified, and basement material.

1.2.2. Sediment section handling

Headspace samples were taken from selected section ends (typically one per core) using a syringe for immediate hydrocarbon analysis as part of the shipboard safety and pollution prevention program. Whole-round samples for interstitial water (IW) analysis also were taken immediately after the core was sectioned. Whole-round subsamples of the lowermost part of each core catcher (paleontology [PAL] samples) were taken for biostratigraphic analysis. When catwalk sampling was complete, liner caps (blue = top, colorless/white = bottom, and yellow = base of a section after a whole-round sample was removed) were glued with acetone onto liner sections, and sections were placed in core racks for analysis.

For sediment cores, the curated length was set equal to the created length and was updated on rare occasions (e.g., in cases of errors or when section length kept expanding by more than ~1–2 cm). Depth in hole calculations are based on the curated section length (see **Depth calculations**).

After completion of whole-round section analyses, the sections were split lengthwise from bottom to top into working and archive halves. The softer cores were split with a wire, and harder cores were split with a diamond saw. It is important to be aware that stratigraphically older material can be displaced upward on the split face of a section during splitting.

1.2.3. Rock piece handling

At Sites U1579, U1580, and U1582, we performed hard rock curation, in which individual pieces were separated with dividers and logged separately. Rock pieces were washed and arranged in section half liners. Plastic dividers made from core liner caps were inserted between core pieces to keep them in place for curation, which typically led to curated section lengths that exceeded created section lengths. As a result, curated core lengths, defined by the sum of curated section lengths, can exceed the length of the cored interval, resulting in recovery rates >100%. Adjacent core pieces that could be fitted together along fractures were curated as single pieces. These pieces are further labeled with letters to indicate the order within the bin; however, the subpieces are not recorded in the Laboratory Information Management System (LIMS) database. Core pieces that appeared susceptible to crumbling were encased in shrink wrap.

A splitting line was marked on each piece with a wax pencil so the piece could be split into representative working and archive halves, ideally maximizing the expression of structures on the cut face of the core in addition to maintaining representative features in both archive and working halves. To ensure a consistent protocol for whole-core imaging, the splitting line was drawn so that the working half was on the right side of the line with the core upright. The working half of each piece was marked with a "W" to the right of the splitting line (Figure **F2**).

Once the split line was drawn, the plastic spacers were secured with acetone, creating bins that constrained movement of pieces during core transport. Spacers were mounted into the liners with the angle brace facing upcore, ensuring that the top of each piece had the same depth as the top of the curated interval for each bin. The top and bottom offsets of each bin were uploaded to the LIMS database. Based on the calculated bin lengths, the cumulative length of all bins, including spacers, was computed as the curated length of the section. The empty split liner with spacers glued in was then placed over the split liner containing the pieces, and the two halves were taped together in a few places for temporary storage until core pieces were dry and equilibrated to laboratory conditions (usually <1 h after arrival from the catwalk).

1.3. Sample naming

Sample naming in this volume follows standard IODP procedure. A full sample identifier consists of the following information: expedition, site, hole, core number, core type, section number, section half, and offset in centimeters measured from the top of the core section. For example, a sample identification of "392-U1579A-1H-2W, 10–12 cm," represents a sample taken from the interval between 10 and 12 cm below the top of the working half of Section 2 of Core 1 ("H" designates that this core was taken using the APC system) of Hole U1579A during Expedition 392.

When working with data downloaded from the LIMS database or physical samples that were labeled on the ship, three additional sample naming concepts may be encountered: text ID, label ID, and printed labels.

1.3.1. Text ID

Samples taken on *JOIDES Resolution* are uniquely identified for use by software applications using the text ID, which combines two elements, sample type designation (e.g., SHLF for section half) and a unique sequential number for any sample and sample type, added to the sample type code (e.g., SHLF30495837). The text ID is not particularly helpful to most users but is critical for machine reading and troubleshooting.

1.3.2. Label ID

The label ID is used throughout the *JOIDES Resolution* workflows as a convenient, human-readable sample identity. However, a label ID is not necessarily unique. The label ID is made up of two parts: primary sample identifier and sample name.

1.3.2.1. Primary sample identifier

The primary sample identifier is very similar to the editorial sample name described above, with two notable exceptions:

- Section halves always carry the appropriate identifier (392-U1579B-25X-2-A versus 392-U1579B-25X-2-W for archive and working half, respectively).

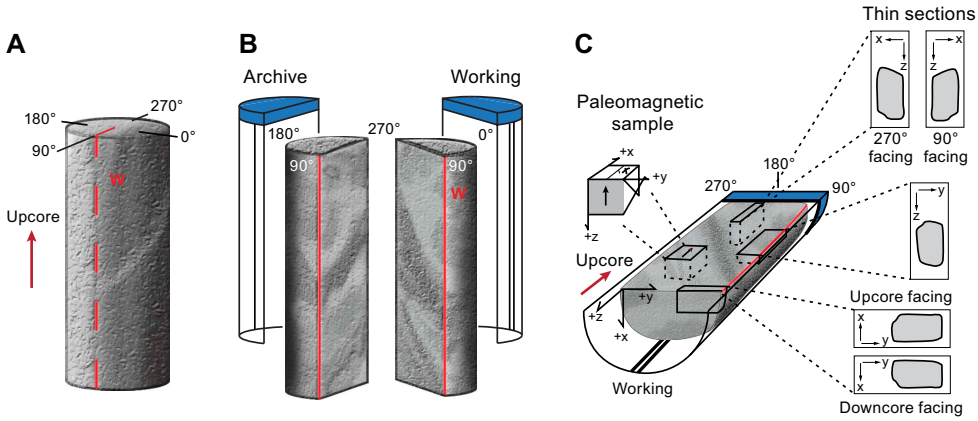

Figure F2. Core reference frame.

- Sample top and bottom offsets, relative to the parent section, are indicated as "35/37" rather than "35–37 cm."

Specific rules were set for printing the offsets at the end of the primary sample identifier:

- For samples taken out of the hole, core, or section before splitting, top offset/bottom offset is not added to the label ID. This has implications for the common process of taking samples out of the core catcher (CC), which technically is a section (relevant primarily for microbiology and PAL samples).
- The top offset/bottom offset is always added to the label ID for samples taken out of the section half. The rule is triggered when an update to the sample name, offset, or length occurs.
- The offsets are always rounded to the nearest centimeter before insertion into the label ID (even though the database stores higher precision positions with offsets reported to millimeter precision).

1.3.2.2. Sample name

The sample name is a free text parameter for subsamples taken from a primary sample or from subsamples thereof. It is always added to the primary sample identifier following a hyphen (-NAME) and populated from one of the following prioritized user entries in the Sample Master application:

1. Entering a sample type (-TYPE) is mandatory (same sample type code used as part of the text ID). By default, -NAME = -TYPE (examples include SHLF, CUBE, CYL, PWDR, and so on).
2. If the user selects a test code (-TEST), the test code replaces the sample type and -NAME = -TEST. The test code indicates the purpose of taking the sample but does not guarantee that the test was actually completed on the sample (examples include PAL, TSB, ICP, PMAG, MAD, and so on).
3. If the user selects a requester code (-REQ), it replaces -TYPE or -TEST and -NAME = -REQ. The requester code represents the name of the requester of the sample who will conduct post-cruise analysis.
4. If the user types any kind of value (-VALUE) in the -NAME field, perhaps to add critical sample information for postcruise handling, the value replaces -TYPE, -TEST, or -REQ and -NAME = -VALUE (examples include SYL-80deg, DAL-40mT, and so on).

In summary, and given the examples above, the same subsample may have the following label IDs:

- 392-U1579B-25X-2-W 35/37-CYL
- 392-U1579B-25X-2-W 35/37-PMAG
- 392-U1579B-25X-2-W 35/37-DAL
- 392-U1579B-25X-2-W 35/37-DAL-40mT

When subsamples are taken out of subsamples, the -NAME of the first subsample becomes part of the parent sample ID, and another -NAME is added to that parent sample label ID:

- Primary_sample_ID-NAME
- Primary_sample_ID-NAME-NAME

For example, a thin section billet (sample type = TSB) taken from the working half at 40–42 cm offset from the section top might result in a label ID of 392-U1579B-25X-4-W 40/42-TSB. After the thin section was prepared (~48 h later), a subsample of the billet might receive an additional designation of TS05, which would be the fifth thin section made during the expedition. A resulting thin section label ID might therefore be 392-U1579B-25X-4-W 40/42-TSB-TS_5.

1.4. Depth calculations

Sample and measurement depth calculations were based on the methods described in IODP Depth Scales Terminology v.2 at **https://www.iodp.org/policies-and-guidelines/142-iodp-depth-scales-terminology-april-2011/file** (Table **T1**). Due to the definition of multiple depth scale types and their distinction in nomenclature, a nominal depth value at two different depth scale types (and even two different depth scales of the same type) generally does not refer to

exactly the same stratigraphic interval in a hole (Figure **F3**). The SI unit for all depth scales is meters.

Depths of cored intervals were measured from the drill floor based on the length of drill pipe deployed beneath the rig floor and referred to as drilling depth below rig floor (DRF); this is traditionally referred to with custom units of meters below rig floor (mbrf). The depth of each cored interval, measured on the DRF scale, can be referenced to the seafloor by subtracting the seafloor depth measurement (on the DRF scale) from the cored interval (on the DRF scale). This seafloor-referenced depth of the cored interval is referred to as the drilling depth below seafloor (DSF) depth scale, and traditionally uses a custom unit designation of mbsf. In the case of APC coring, the seafloor depth was the length of pipe deployed minus the length of the mudline core recovered. In the case of RCB coring, the seafloor depth was adopted from a previous hole drilled at the site or by tagging the seafloor.

Depths of samples and measurements in each core were computed based on a set of rules that result in a depth scale type referred to as CSF-A. The two fundamental rules are that (1) the top depth of a recovered core corresponds to the top depth of its cored interval (top DSF = top CSF-A) regardless of type of material recovered or drilling disturbance observed and (2) the recovered material is a contiguous stratigraphic representation even when core segments are separated by voids when recovered, the core is shorter than the cored interval, or it is unknown how much

Table T1. Depth scales used during Expedition 392. mbrf = meters below rig floor, mbsf = meters below seafloor, mcd = meters composite depth. **Download table in CSV format.**

Depth scale type	Acronym	Unit	Historical reference	Figure axis labels	Text
Drilling depth below rig floor	DRF	m	mbrf	NA	NA
Drilling depth below seafloor	DSF	m	mbsf	Depth DSF (m)	x m DSF
Wireline log depth below rig floor	WRF	m	mbrf	NA	NA
Wireline log depth below seafloor	WSF	m	mbsf	NA	NA
Wireline log speed-corrected depth below seafloor	WSSF	m	mbsf	NA	NA
Wireline log matched depth below seafloor	WMSF	m	mbsf	Depth WMSF (m)	x m WMSF
Core depth below seafloor, Method A	CSF-A	m	mbsf	Depth CSF-A (m)	x m CSF-A
Core depth below seafloor, Method B	CSF-B	m	mbsf	NA	NA
Core composite depth below seafloor	CCSF	m	mcd	Depth CCSF (m)	x m CCSF

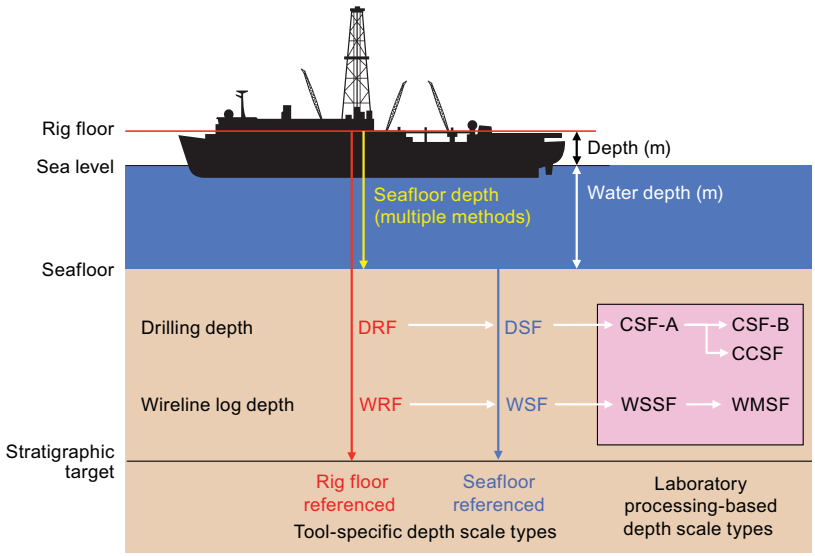

Figure F3. Depth scales used during Expedition 392. DRF = drilling depth below rig floor, DSF = drilling depth below seafloor, CSF = core depth below seafloor (Method A or B), CCSF = core composite depth below seafloor, WRF = wireline log depth below rig floor, WSF = wireline log depth below seafloor, WSSF = wireline log speed-corrected depth below seafloor, WMSF = wireline log matched depth below seafloor.

material is missing between core pieces. When voids were present in the core on the catwalk, they were closed by pushing core segments together whenever possible. The length of missing core should be considered a depth uncertainty when analyzing data associated with core material.

When core sections were given their curated lengths, they were also given a top and a bottom depth based on the core top depth and the section length. Depths of samples and measurements on the CSF-A scale were calculated by adding the offset of the sample (or measurement from the top of its section) to the top depth of the section.

Per IODP policy established after the introduction of the IODP Depth Scales Terminology v.2, sample and measurement depths on the CSF-A depth scale type can be referred to with the custom unit mbsf, just like depths on the DSF scale type. In this volume, we use the CSF-A depth scale type. For example, a soft-sediment core from less than a few hundred meters below seafloor often expands upon recovery (typically by a few percent to as much as 15%), and the length of the recovered core exceeds that of the cored interval. Therefore, a stratigraphic interval in a particular hole may not have the same depth on the DSF and CSF-A scales. When recovery in a core exceeds 100%, the CSF-A depth of a sample taken from the bottom of the core will be deeper than that of a sample from the top of the subsequent core (i.e., some data associated with the two cores overlap on the CSF-A scale). To overcome the overlap problem, core intervals can be placed on the core depth below seafloor, Method B (CSF-B), depth scale. The Method B approach scales the recovered core length back into the interval cored, from >100% to exactly 100% recovery. If cores had <100% recovery to begin with, they are not scaled. When downloading data using the *JOIDES Resolution* Science Operator (JRSO) LIMS Reports pages (**http://web.iodp.tamu.edu/LORE**), depths for samples and measurements are by default presented on both CSF-A and CSF-B scales. The CSF-B depth scale can be useful for data analysis and presentations at sites with a single hole.

A core composite depth below seafloor (CCSF) scale can be constructed to mitigate inadequacies of the CSF-A scale for scientific analysis and data presentation. The most common application is the construction of a CCSF scale from multiple holes drilled at a site using depth shifting of correlative features across holes. This method not only eliminates the CSF-A core overlap problem but also allows splicing of core intervals such that gaps in core recovery, which are inevitable in coring a single hole, are essentially eliminated and a continuous stratigraphic representation is established. This depth scale type was used at Sites U1579 and U1580 during Expedition 392.

A CCSF scale and stratigraphic splice are accomplished by downloading correlation data from the expedition (LIMS) database using the Correlation Downloader application, correlating stratigraphic features across holes using Correlator or any other application, depth-shifting cores to create an affine table with an offset for each core relative to the CSF-A scale, and creating a splice interval table that defines which core intervals from the participating holes make up the stratigraphic splice. Affine and splice interval tables can be uploaded to the LIMS database, where internal computations create a CCSF depth scale. The CCSF depth can then be added to all subsequent data downloads from the LIMS database, and data can be downloaded for a splice.

1.5. Shipboard core analysis

Whole-round core sections were immediately run through the Natural Gamma Radiation Logger (NGRL). For some holes, whole-round core sections were scanned using the X-ray Multisensor Logger (XMSL). After thermally equilibrating for at least 4 h, core sections were run through the Whole-Round Multisensor Logger (WRMSL), which measures *P*-wave velocity, density, and magnetic susceptibility (MS). For unconsolidated cores, thermal conductivity measurements were also taken before the cores were split lengthwise into working and archive halves. The working half of each core was sampled for shipboard analysis (routinely for paleomagnetism and physical properties and more irregularly for geochemistry and biostratigraphy). *P*-wave velocity was also measured on working halves and cubic samples using the Section Half Measurement Gantry (SHMG). The archive half of each core was passed through the Section Half Multisensor Logger (SHMSL) for measurement of point MS (MSP) and color reflectance, and a puck probe was used to measure thermal conductivity of consolidated sediments. The archive halves were described macroscopically and microscopically in smear slides. Finally, the archive halves were run through the cryo-

genic magnetometer. Both halves of the core sections were then put into labeled plastic tubes that were sealed and transferred to cold storage space aboard the ship.

A total of 4167 samples (which includes PAL and IW splits) were taken for shipboard analysis. At the end of Expedition 392, all core sections and thin sections were shipped to the Gulf Coast Repository for X-ray fluorescence (XRF) core scanning in June–August 2022, followed by a shore-based sampling party in August 2022. The sections and samples will then be transferred to and permanently stored in the Kochi Core Center.

1.6. Authorship of site chapters

All shipboard scientists contributed to this volume. However, the separate sections of the site chapters and Expedition 392 methods chapter were written by the discipline-based groups of scientists listed below (authors are listed in alphabetical order; no seniority is implied):

Background and objectives: S.M. Bohaty, L.B. Childress, G. Uenzelmann-Neben
Operations: L.B. Childress, W. Rhinehart
Lithostratigraphy: H.C. Cawthra, P. Chanda, D. Gürer, S.J. Haynes, D. Jana, D.E. Penman
Igneous petrology: P.C. Davidson, J. Geldmacher, Y. Ichiyama, J. Liu
Micropaleontology: O.A. Archontikis, P.K. Bijl, A.M. Burkett, J.J. Coenen, J.O. Herrle, D.K. Kulhanek
Paleomagnetism: E. Dallanave, C. Kato, C.J. Sprain
Stratigraphic correlation: S.J. Batenburg, T. Westerhold
Chronostratigraphy: O.A. Archontikis, S.J. Batenburg, P.K. Bijl, A.M. Burkett, J.J. Coenen, E. Dallanave, J.O. Herrle, D.K. Kulhanek, C.J. Sprain, T. Westerhold
Geochemistry: K.E. Doiron, J. McManus, A. Tessin, T. Wagner
Physical properties: S.J. Batenburg, M.M. Jones, J. Li, A. Minakov, T. Westerhold
Downhole measurements: M.M. Jones, A. Minakov

2. Lithostratigraphy

The lithology of material recovered during Expedition 392 was primarily determined using macroscopic core descriptions of split cores and observations from smear slides and thin sections. Descriptions were based primarily on examination of the archive halves of each core, supplemented by the working halves where appropriate. When necessary, digital core imaging, color reflectance spectrophotometry, X-ray diffraction (XRD), portable X-ray fluorescence (pXRF) spectrometry, physical properties (see **Physical properties**), and MS analyses were used to provide complementary description criteria. Percent $CaCO_3$ data (see **Geochemistry**) were also used to refine sediment descriptions. The methods employed during this expedition were modified from those used during IODP Expeditions 369 (Huber et al., 2019a) and 371 (Sutherland et al., 2019). The DESClogik application was used to record and upload descriptive data into the LIMS database. Spreadsheet templates were set up in DESClogik and customized for Expedition 392 before the first core was recovered. These templates were used to generate VCDs and record microscopic data from smear slides and thin sections. These additional data sets were used to describe the textures and relative abundances of biogenic and nonbiogenic components. The sampling positions of each smear slide and thin section were recorded using Sample Master software and are indicated on the VCDs.

The general workflow for description of Expedition 392 cores was as follows: (1) cores were split and the archive halves were prepared for sediment description (e.g., excess moisture removed and the split-core surface smoothed using a clean glass slide), (2) section halves were imaged and "barrel sheet" templates were generated, (3) smear slides were prepared using toothpick samples or scrapings from the split-core surface, (4) each section half was described (macroscopic) and the information handwritten onto the barrel sheet, (5) barrel sheet data were transcribed into DESClogik, and (6) electronic VCDs were generated.

The standard method of splitting cores into working and archive halves using a piano wire or a saw can disturb the split-core surface and obscure fine details of the lithology and sedimentary struc-

tures. Where necessary, core archive halves were scraped and smoothed with a glass or metal slide parallel to bedding for improved results during digital imaging and to prevent cross-stratigraphic contamination during sedimentological analyses. Imaging lithified clay-rich intervals is commonly distorted by moisture along cracks and bedding planes, which can take a great deal of time to dry in ambient laboratory conditions. To obtain high-quality images, the cores were air dried using a Super Quality Imager of Section Halves (SQUISH), which consists of a series of fans positioned along the track of the Section Half Imaging Logger (SHIL). Prepared section halves were scanned using the SHIL and the SHMSL (see **Physical properties**). Sediment/rock color was determined qualitatively for each core using a Munsell soil color chart and quantitatively for the entire section using the SHMSL (reflectance) and SHIL (red-green-blue color space [RGB]) to track downcore changes in lithology. A general characterization of color was also noted for each section. Because sediment color may change during drying and subsequent oxidization during storage, color was described shortly after the cores were split.

2.1. Section-half images

The SHIL uses three pairs of advanced illumination high-current-focused LED line lights to illuminate features of the core. A linescan camera made by JAI was used to image the split-core surface at a resolution of 20 lines/mm to create a high-resolution TIFF file, and two low-resolution JPEG files (cropped and uncropped) were subsequently created. The full-size TIFF images are 508 ppi (dpi). The camera height was adjusted so that the size of each pixel was 50 µm. However, the actual core width per pixel varied because of differences in surface height of each section half. Uncropped SHIL images include a grayscale and ruler. Foam placeholders were positioned within the cores to mark the locations of samples removed from the core before imaging (e.g., IW and paleontology) and to mark the positions of voids. Section-half depths were automatically included with images and stored in the LIMS database.

2.2. Macroscopic core descriptions

Macroscopic core descriptions were first made on handwritten description forms (barrel sheets) for each section and then entered into the Macroscopic template core description tabs in DESClogik. Standard sedimentological observations of lithology, sedimentary structures, color, bioturbation, and accessories were documented, as well as specific comments, when necessary. All handwritten sheets were digitally preserved as PDF files (see HAND_DESC in **Supplementary material**).

2.3. Visual core descriptions

VCDs are simplified graphical representations for each core within sediments/sedimentary rock intervals (Figure **F4**) and for each section within igneous and basement rock intervals (see **Igneous petrology**). VCDs were generated after core descriptions were entered into the DESClogik software and uploaded to the LIMS database. For stratigraphic intervals where both sedimentary and igneous rocks were encountered, two VCDs were produced to optimize the descriptive output (Figures **F4**, **F5**).

2.3.1. Core summary

Graphic lithology is displayed on each VCD with physical descriptions for each core, which include information on grain size, Munsell color, sedimentary structures, lithologic accessories, bioturbation intensity, and type and intensity of drilling disturbances. Depth and length of core sections are indicated along the left margin in the CSF-A, depth scale. Graphic patterns and symbols used in the VCDs are shown in Figure **F4**. In addition, VCDs display a preliminary subepoch age estimate, the types and locations of shipboard samples taken, and relevant physical properties data for that site (natural gamma radiation [NGR], color reflectance [L*, a*, b*], and MS).

2.3.2. Graphic lithology

Lithologies of the recovered core intervals are represented on the VCDs by graphic patterns in the Graphic lithology column using the patterns illustrated in Figure **F4**. All sedimentary beds thicker than 2 cm are represented in the Graphic lithology column on each VCD. Major modifiers (pre-

fixes) of a principal lithology are shown by an adjoining pattern on the left side of the graphic lithology column, and minor modifiers (suffixes) are shown on the right side of the column. Relative abundances of lithologic constituents reported in this way are useful for general characterization of the sediment but do not constitute precise quantitative observations.

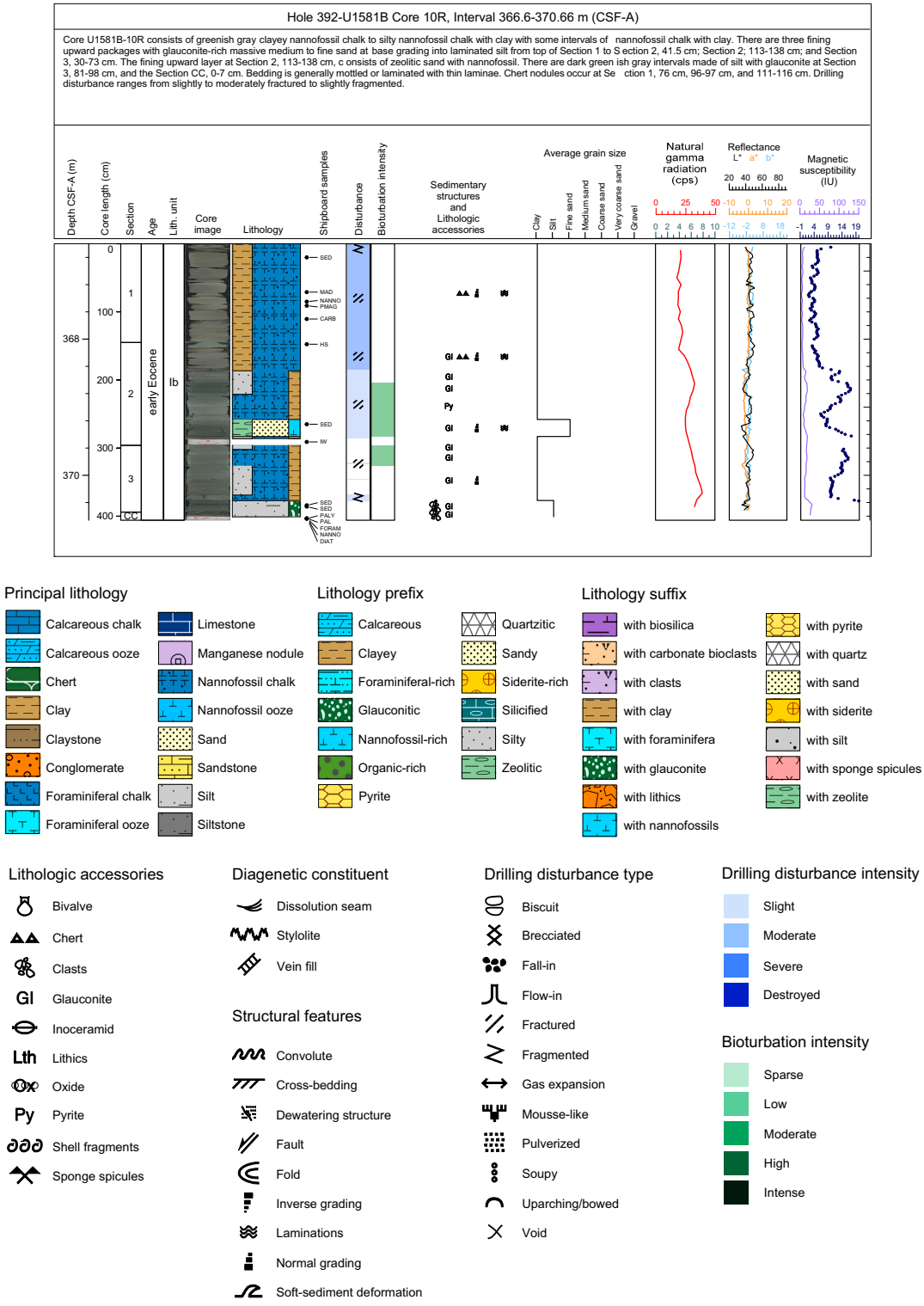

Figure F4. Example VCD and VCD legend used during Expedition 392. cps = counts per second.

2.3.3. Sedimentary structures

The locations and types of stratification and sedimentary structures visible on the prepared surfaces of the split cores are shown in the Sedimentary structures and lithologic accessories column of the VCD. Symbols in this column indicate lithologic accessories such as shell fragments and pyrite nodules, as well as other sedimentary features such as laminations (Figure **F4**). Terminology outlined in Stow (2005) was used to categorize stratification thickness (Table **T2**). Descriptive terms for bed boundaries, such as sharp, erosive, gradational, and bioturbated, were noted in

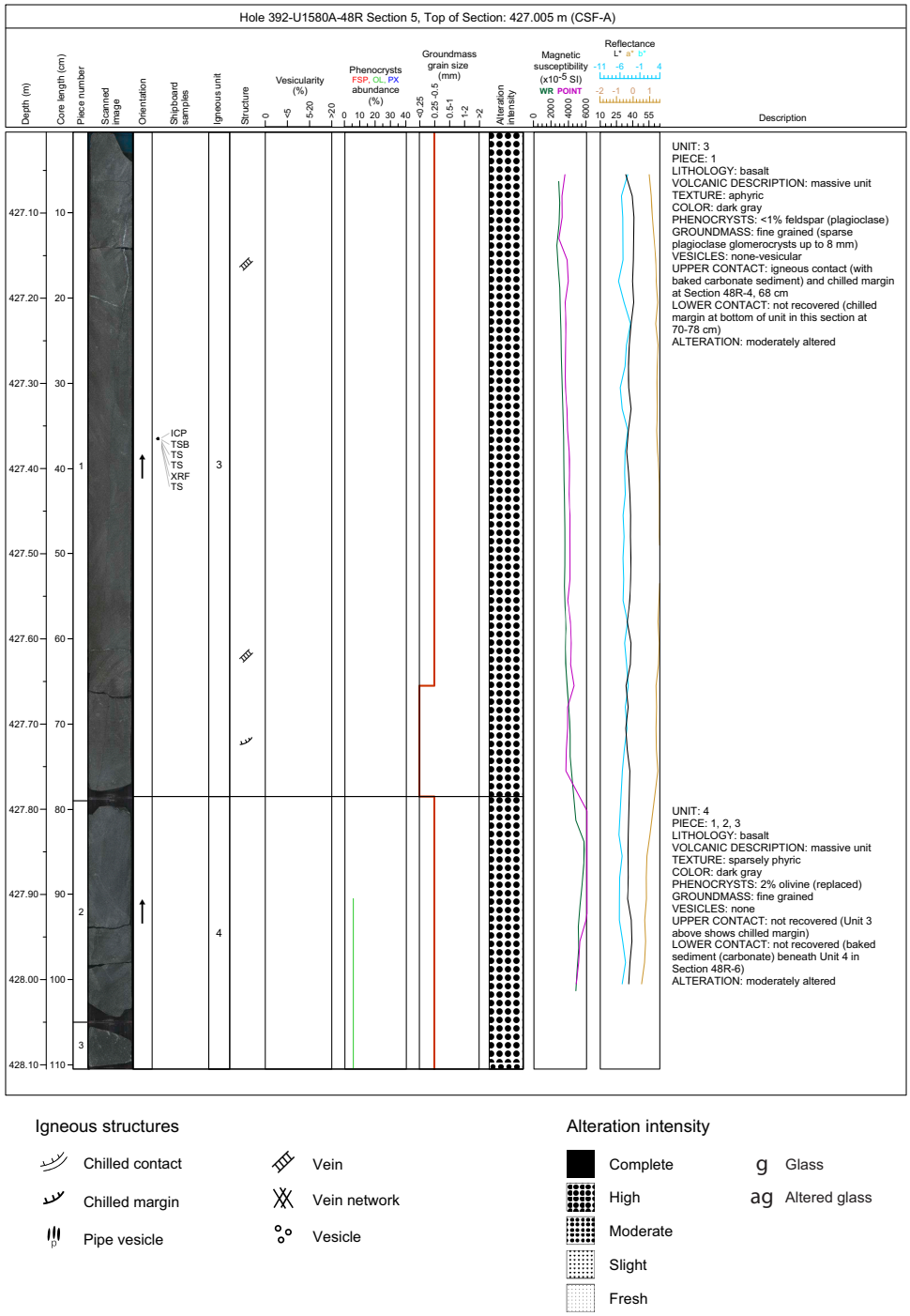

Figure F5. Example igneous core section VCD used during Expedition 392. Symbols and nomenclature used for igneous rock descriptions are shown. FSP = feldspar, OL = olivine, PX = pyroxene. WR = whole round MS, POINT = MSP. Color reflectance values: L* (perceptual lightness with black = 0 and white = 100), a* (green-red axis with negative values toward green and positive values toward red), and b* (blue-yellow axis with negative numbers toward blue and positive toward yellow).

DESClogik. Soft-sediment deformation was noted by a symbol on the VCD and specific types of soft-sediment deformation and microfaulting were noted in core summaries on the top of the VCD (e.g., convolute bedding, load casts, scours, and flame structures).

2.3.4. Deformation structures

Deformation of the core clearly identified as not related to drilling disturbance was recorded and included in the Sedimentary structures and lithologic accessories column using the symbols in Figure **F4**. These structures include synsedimentary deformation, such as dewatering structures, slump folds, or faults, and postdepositional features, such as fractures, faults, and folds. Although rarely resolvable, sense of deformation (e.g., reverse or normal; dextral versus sinistral strike-slip displacement) was recorded in the comment section of DESClogik. Interval thickness was recorded from the uppermost to the lowermost extension of the described feature on the archive section half.

The descriptive terminology used for deformation structures in hard and soft rocks follows Ramsay and Huber (1987), and terminology used for sediments follows Maltman (1994). For microstructures, we applied the terminology of Passchier and Trouw (1996).

Deformation structures were oriented in the core reference frame used for paleomagnetic analyses, but they were not oriented with respect to geographic ordinates (Figure **F2**). Formation MicroScanner (FMS) data collected during downhole logging in Hole U1580A are available for core reorientation.

2.3.5. Drilling disturbance

Cores can be significantly disturbed by the drilling process and contain extraneous material as a result of coring and core handling processes. In formations with loose granular layers (sand, ash, foraminiferal ooze, chert, shell fragments, etc.), granular material from intervals higher in the hole may settle and accumulate in the bottom of the hole as a result of drilling activity and be sampled with the next core. Therefore, the uppermost 10–50 cm of each core were examined critically for potential fall-in material.

Common piston coring-induced deformation includes the concave-downward appearance of originally horizontal bedding (uparching). Piston action may also result in fluidization (flow-in) at the bottom of APC cores. Retrieval of unconsolidated (APC) cores from depth to the surface typically results to some degree in elastic rebound, and gas that is in solution at depth may become free and drive core segments in the liner apart. When gas content is high, pressure must be relieved for safety reasons before the cores are cut into sections. Holes are drilled into the liner, which forces some sediment and gas out of the liner. XCB coring typically results in core material broken (torqued) into biscuits, which are disc-shaped pieces a few to several centimeters long surrounded by fluidized sediment mixed with drilling slurry. RCB coring typically homogenizes unlithified core material and often fractures lithified core material.

Drilling disturbance type and intensity was recorded in the Disturbance column of the VCD using the symbols shown in Figure **F4**. The type of drilling disturbance was described for soft and firm sediments using the terms described in Table **T3**. The intensity of drilling disturbance (slight,

Table T2. Bed thickness categories (Stow, 2005), Expedition 392. **Download table in CSV format.**

Classification	Thickness (cm)
Thin lamination	<0.3
Medium lamination	0.3–0.6
Thick lamination	0.6–1
Very thin bed	1–3
Thin bed	3–10
Medium bed	10–30
Thick bed	30–100
Very thick bed	>100

moderate, severe, and destroyed) is described using a color scale, and the criteria for these parameters are listed in Table T4.

2.3.6. Lithologic accessories

Lithologic, diagenetic, and paleontologic accessories, such as nodules, shell fragments, and pyrite nodules, are indicated in the Sedimentary structures and lithologic accessories column on the VCD and are also noted in the General interval comments column in DESClogik. The symbols used to designate these features are shown in Figure F4.

2.3.7. Bioturbation intensity

Description and intensity of bioturbation were classified using the scheme of Stow (2005) and are denoted with a color scale in the Bioturbation intensity column (Figure F4; Table T5). Identifiable ichnofossils were described in the Core summary text on the VCD.

Table T3. Drilling disturbance classification, Expedition 392. **Download table in CSV format.**

Drilling disturbance type	Description
Fall-in	Out of place material at the top of a core that has fallen downhole onto the cored surface
Bowed	Bedding contacts are slightly to moderately deformed but still subhorizontal and continuous
Uparching	Material retains its coherency, with material closest to the core liner being bent downward
Void	Empty space in the cored material (e.g., caused by gas or sediment expansion during core retrieval). To the extent possible, voids were closed on the core receiving platform by pushing the recovered intervals toward the top of the core before cutting the sections. The space left below all the recovered material due to incomplete recovery was not described.
Coring/drilling slurry, or along-core gravel/sand contamination	Soft-sediment stretching and/or compressional shearing structures when severe
Flow-in	Soft sediment at the base of an APC core that has flowed vertically into the core barrel during piston action
Soupy	Intervals are water saturated and have lost all aspects of original bedding
Mousse-like	Intervals have been water saturated and re-stiffened and have lost all aspects of original bedding. Does not contain firmer undisturbed intervals
Biscuit	Sediment of intermediate stiffness has vertical variations in the degree of disturbance, whereas firmer intervals are relatively undisturbed
Fractured	Firm sediment is broken during drilling but is not displaced or rotated
Fragmented	Firm sediment is broken during drilling that may be rotated but has retained its stratigraphic placement
Brecciated	Firm sediment is pervasively broken by drilling and may be displaced or rotated
Pulverized	Firm sediment with no clear placement or orientation within the interval

Table T4. Drilling disturbance intensities, Expedition 392. **Download table in CSV format.**

Degree of severity	Description
None	No disturbance noted
Slight	Core material is in place but broken or otherwise disturbed
Moderate	Core material is in place or partly displaced, but original orientation is preserved or recognizable
Severe	Core material is probably in correct stratigraphic sequence, but original orientation is lost
Destroyed	Core material is in incorrect stratigraphic sequence and original orientation is lost, or core is crushed and broken into many small pieces and original orientation and stratigraphic position are lost

Table T5. Index of bioturbation intensity (Stow, 2005), Expedition 392. **Download table in CSV format.**

Intensity	Description
Sparse	Bedding distinct, one or two traces and/or escape features are observed
Low	Bedding boundaries sharp, discrete traces with no overlap
Moderate	Bedding boundaries sharp, traces discrete, overlap is rare
High	Bedding boundaries obscured, traces overlap
Intense	Bedding boundaries indistinct or completely disturbed, high trace density with most traces overlapping
NA	No bioturbation or completely bioturbated with no bedding boundaries preserved

2.3.8. Lithostratigraphic unit and age

Lithostratigraphic units were defined at each site where successions of conformable units with similar sedimentary characteristics or phases were recognized. These successions were given consecutive downhole Roman numbers (Lithostratigraphic Units I, II, etc.) and are shown in the Lithostratigraphic unit column of the VCD (Figure **F4**). Where necessary, lithostratigraphic subunits were also defined (Lithostratigraphic Subunits Ia, Ib, etc.). Sediment age was based on the shipboard biostratigraphy (see **Micropaleontology**) and magnetostratigraphy (see **Paleomagnetism**) and is listed in the Age column to subepoch level.

2.3.9. Shipboard samples

Positions of shipboard samples used for microscopic descriptions (i.e., smear slides and thin sections; SED), mineralogical analyses (XRD), shipboard chemical analyses (IW, HS, ICP, and CARB; see **Geochemistry**), micropaleontological (PAL, NANNO, FORAM, PALY, and DIAT; see **Micropaleontology**), paleomagnetic (see **Paleomagnetism**) and physical properties analyses (MAD; see **Physical properties**) are indicated with an annotation adjacent to the graphic lithology column on each VCD (Figure **F4**).

2.4. Sediment classification

Recovered sediments are primarily composed of biogenic, siliciclastic, and volcaniclastic components and were described using a classification scheme derived from IODP Expeditions 369 (Huber et al., 2019a), 371 (Sutherland et al., 2019), and 349 (Li et al., 2015), Deep Sea Drilling Project (DSDP) Leg 26 (Luyendyk and Davies, 1974), Ocean Drilling Program (ODP) Leg 182 (Shipboard Scientific Party, 2000), and the classification of Stow (2005). The biogenic component includes open-marine calcareous and siliceous microfossils (e.g., foraminifera, calcareous nannofossils, diatoms, radiolarians, and sponge spicules) and macrofossils (e.g., shell and coral fragments). The siliciclastic component consists of mineral and rock fragments derived from physical weathering of igneous, sedimentary, and metamorphic rocks. The relative proportion of these two components are used to define the major classes of sediment in this scheme (Figure **F6**). For the purposes of classification, diagenetic metal oxides and silica minerals are included in the siliciclastic component.

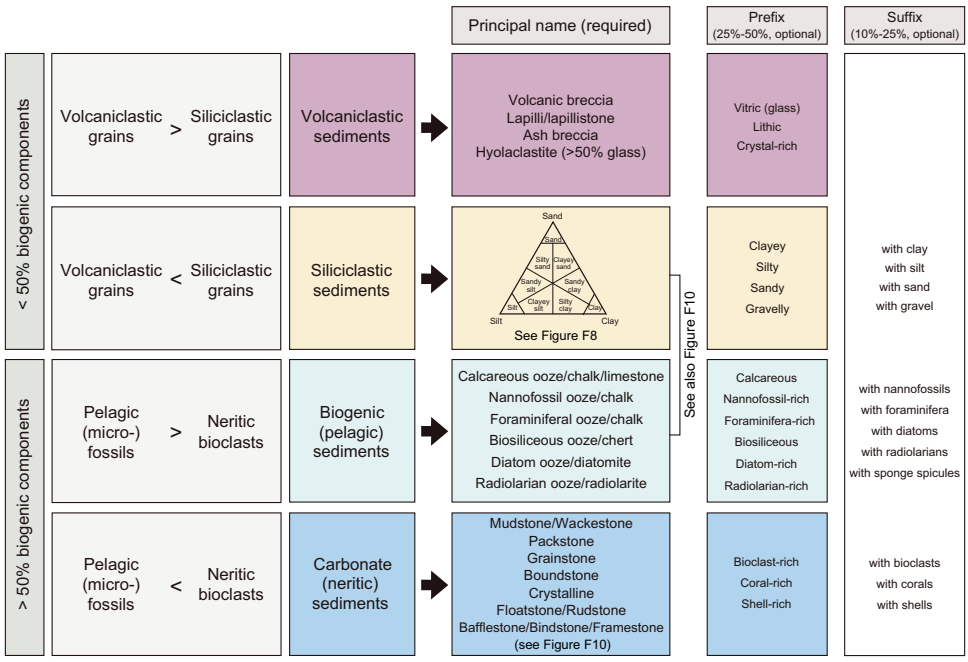

Figure F6. Sediment and sedimentary rock naming scheme used during Expedition 392. Adapted from Expedition 369.

Lithologic naming conventions used during Expedition 392 follow the general guidelines of the ODP sediment classification scheme (Mazzullo et al., 1988), but a separate "mixed sediment" category was not distinguished. As a result, biogenic sediments are those that contain >50% biogenic grains and <50% siliciclastic grains, whereas siliciclastic sediments are those that contain >50% siliciclastic grains and <50% biogenic grains (Figure **F6**). We follow the naming schemes of Shepard (1954), Pettijohn and Siever (1987), Folk (1962), Dunham (1962), and Stow (2005) for the detailed classification of sediments and sedimentary rocks. Sediment grain size divisions for both biogenic and siliciclastic components are based on the major textural categories of Wentworth (1922) (Figure **F7**). These categories are defined using the relative proportions of sand-, silt-, and clay-sized particles (Figure **F8**, modified after Shepard, 1954), which can be difficult (e.g., silty clay versus sandy clay) without quantitative grain size measurements. The term "clay" is only used to describe particle size (not mineralogy) and is applied to both clay minerals and all other nonbiogenic grains <4 µm.

Lithologic names assigned to these sediments consist of a principal name with major (prefix) and minor (suffix) modifiers that are based on composition and degree of lithification and/or texture as determined from visual description of the cores and from smear slide observations (Figure **F6**).

2.5. Naming of siliciclastic and biogenic sediments

2.5.1. Principal names

For sediments with >90% biogenic components, the name applied indicates the most common type of biogenic grains. For example, sediment composed of >90% calcareous nannofossils is called nannofossil ooze/chalk, and sediment composed of 50% foraminifera and 45% calcareous nannofossils is called nannofossil-rich foraminiferal ooze/chalk. For sediment with >90% siliciclastic grains, the principal name is based on the textural characteristics of all sediment particles (both siliciclastic and biogenic).

For a sediment sample that contains a significant mixture of siliciclastic and biogenic components (10%–90% of both siliciclastic and biogenic components), the principal name is determined by the more abundant component (Figures **F6**, **F8**, **F9**). If the siliciclastic component is more abundant (i.e., >50% siliciclastic components), the principal name is based on the textural characteristics such as silty clay or sandy silt. If the biogenic component is more abundant (i.e., <50% siliciclastic components), the principal name is based on the predominant biogenic component, such as calcareous ooze.

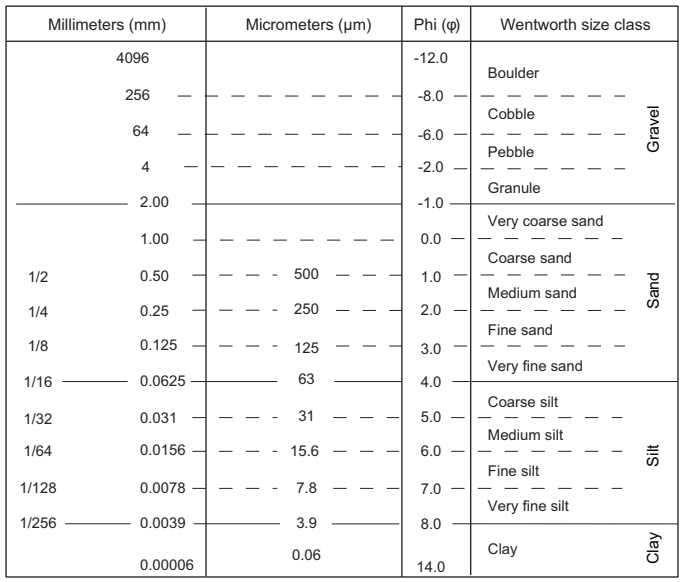

Figure F7. Udden-Wentworth grain size classification.

2.5.2. Major and minor modifiers

If a biogenic (or siliciclastic/volcaniclastic) group makes up 10%–50% of the sediment and this group is not included as part of the principal name, major (prefix) and/or minor (suffix) modifiers are generally used. When a microfossil group (e.g., diatoms, nannofossils, or foraminifera) comprises 25%–50% of the sediment (corresponding to "abundant" in smear slide description), a major

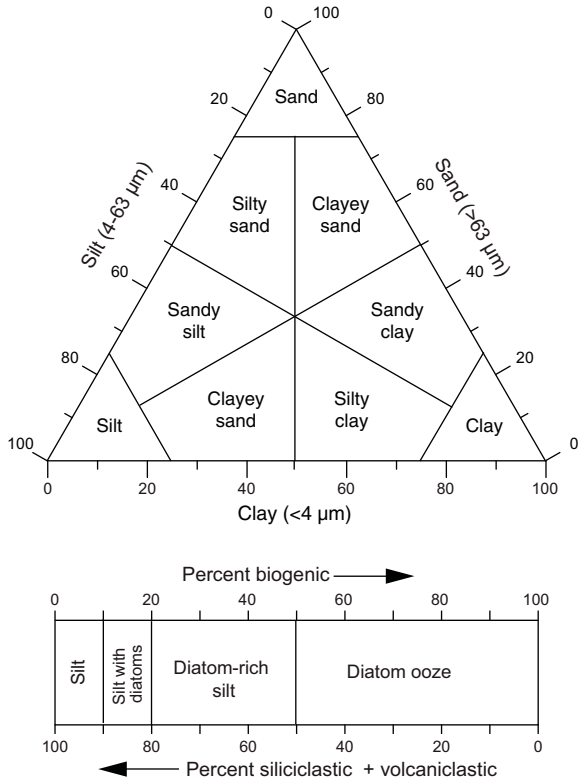

Figure F8. Ternary diagram for siliciclastic principal lithologies. For definition of grain sizes see Figure F7. Modified from Shepard, 1954.

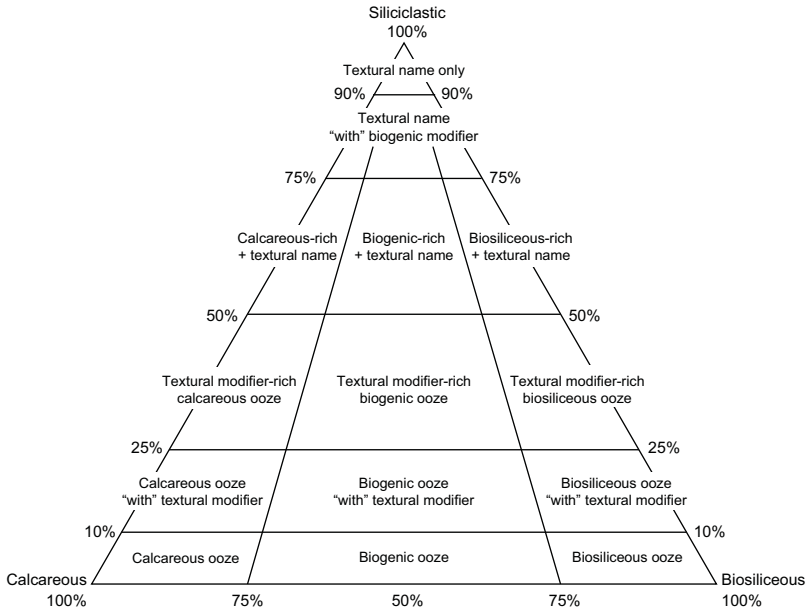

Figure F9. Calcareous-biosiliceous-siliciclastic ternary diagram. Modified after Shepard, 1954.

modifier consisting of the component name hyphenated with "-rich" (e.g., diatom-rich clay) is used. The principal name is followed by a minor modifier (e.g., with diatoms), which is the most abundant component among those making up 10%–20% of the sediment (corresponding to "common" in smear slide description). If the minor component is biogenic, then the modifier describes the group of biogenic grains that exceeds the 10% abundance threshold (e.g., silty clay with radiolarians). If the minor component is siliciclastic, the minor modifier is based on the texture of the siliciclastic fraction (e.g., diatom ooze with clay).

If the primary lithology for an interval of core has a major or minor modifier, that modifier is indicated in the Lithology column of the VCD by overlaying the pattern of the modifier on the left (major modifiers) or right (minor modifiers) of the Lithology column.

2.5.3. Primary lithologies by lithification grades

Each primary lithology indicates a composition and a degree of lithification (e.g., ooze versus chalk). The following terms describe lithification that varies depending on the dominant composition, and the degree of lithification is specified on the VCD:

- Sediment samples that are composed predominantly of calcareous, pelagic organisms (e.g., calcareous nannofossils and foraminifera): the lithification terms "ooze" and "chalk" reflect whether the sediment sample can be deformed with a finger (ooze) or scratched easily by a fingernail (chalk) or are too hard to be scratched easily by a fingernail (limestone).
- Siliceous sediment that is too hard to be scratched with a glass slide: the term "silicified limestone" is used.
- Sediment samples that are composed predominantly of siliciclastic material: if the sediment can be deformed easily with a finger, no lithification term is added and the sediment is named for the dominant grain size (i.e., sand, silt, or clay). For more consolidated material, the lithification suffix "-stone" is appended to the dominant size classification (e.g., claystone), except for gravel-sized sediment, when the terms "conglomerate" or "breccia" are used depending on whether the clasts are rounded or angular, respectively.

2.5.4. Classification of limestones

The principal names of well-lithified neritic carbonate sediments were assigned based on the classification by Dunham (1962) and Embry and Klovan (1971) (Figure **F10**). Following the terminology used for DSDP Site 258 (Luyendyk and Davies, 1974), the term "silicified limestone" was used for samples characterized by fine-grained calcareous biogenic sediments that were partially or fully cemented or replaced by silica. Silicified intervals and nodules with grains too fine to distinguish without magnification were described as chert.

2.6. Microscopic description

For unlithified sediments, at least one smear slide was made from the archive half of each core to determine the lithology. For well-cemented sediments, thin sections were made following stan-

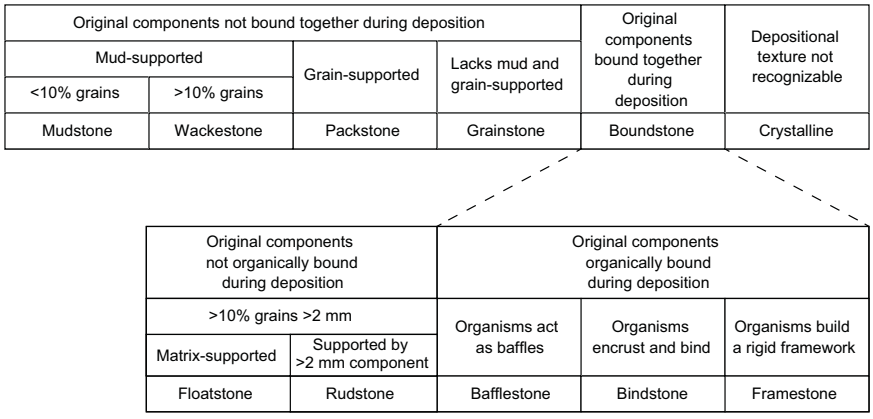

Figure F10. Dunham limestone classification scheme.

dard procedures. Additional samples were collected from intervals of interest (e.g., laminations and sedimentary contacts). For smear slides, a small amount of sediment was taken with a wooden toothpick and put on a 2.5 cm × 7.5 cm glass slide. The sediment sample was homogenized with a drop of deionized water and evenly spread across the slide to create a very thin (about <50 µm) uniform layer of sediment grains for qualitative estimation of relative abundance. The dispersed sample was dried on a hot plate. A drop of Norland optical adhesive No. 61 was added as a mounting medium to a coverslip, which was carefully placed on the dried sample to minimize air bubbles from being trapped in the adhesive. The optical adhesive was then cured in an ultraviolet light box.

Smear slides were examined with a transmitted light petrographic microscope equipped with a standard eyepiece micrometer. The texture of siliciclastic grains (relative abundance of sand-, silt-, and clay-sized grains) and the proportions and presence of biogenic and mineral components were visually estimated and recorded in DESClogik. The mineralogy of clay-sized grains could not be determined from smear slides. The abundance of all components was described using semiqualitative categories (Table **T6**) that correspond to the categories used in our sediment classification scheme. For example, >50% = "dominant" in smear slide abundance and determines the principal lithology, and 10%–25% = "common" and is indicated by a minor modifier in our classification scheme. Note that smear slide analyses tend to underestimate the amount of sand-sized and larger grains because these grains are difficult to incorporate into the preparation.

2.7. X-ray diffraction analyses

Samples were prepared for XRD analysis from selected intervals to identify the main mineral phases in bulk samples. For most of the samples, XRD analysis was performed on bulk sediment. In preparation for bulk mineralogy analysis, samples were freeze-dried and then ground using an agate mortar and pestle. However, a few samples were also prepared for XRD analysis of the clay mineral fraction. For these preparations, carbonate was removed by placing ~2 g of sample in a 50 mL centrifuge tube with 10% acetic acid, mixing it, and then letting it sit overnight. Acidified samples were centrifuged for 15 min at 1500 rpm, and then the acetic acid was decanted. To wash the samples, 25 mL of distilled water was added to the tube, the sample was centrifuged, and the water was decanted. This washing procedure was repeated four times to remove both the acid and salts from the sample. After decanting the final wash, 25 mL of 1% borax solution was added to the sample. The sample was then placed in a dismembrator to suspend the clays and then centrifuged for 4 min at 750 rpm to settle the >2 µm particles. The supernatant liquid containing clays in suspension (<2 µm fraction) was transferred into a clean centrifuge tube and centrifuged for 15 min at 1500 rpm to separate from the borax solution, which was then decanted. The sample was rinsed by adding 25 mL of distilled water, centrifuged, and then decanted. The washing procedure was repeated three times to remove all of the borax solution from the sample. The clays that remained in suspension were removed from the top ~1.5 cm of the centrifuge tube and pipetted onto three amorphous quartz sample discs. The sample discs were then left to air dry in a desiccator for 12 h. After drying, one disc was solvated with ethylene glycol for ~8 h at 65°C and one was heated in a furnace for 1–2 h at 550°C. All three discs were then analyzed to determine the presence of expandable clays. Prepared samples were top-mounted onto a sample holder and analyzed using a Bruker D4 Endeavor diffractometer mounted with a Vantec-1 detector using nickel-filtered CuKα radiation. The standard locked coupled scan settings are described in Table **T7**.

Shipboard bulk XRD results yielded only qualitative information for the presence of the most common mineral components. Diffractograms of bulk samples were processed (e.g., baseline

Table T6. Smear slide abundance classes, Expedition 392. **Download table in CSV format.**

Code	Name	% Abundance
T	Trace	<1
R	Rare	1–10
C	Common	10–25
A	Abundant	25–50
D	Dominant	>50

Table T7. XRD standard locked coupled scan settings, Expedition 392. **Download table in CSV format.**

Parameter	Setting
Voltage (kV)	40
Current (mA)	40
Goniometer scan (°2θ)	4–70
Step size (°2θ)	0.0087
Scan speed (s/step)	0.3
Divergence slit (mm)	0.3
Time per sample (min)	41

removal) with the software package DIFFRAC.EVA by Bruker, which allowed peak characterization and mineral identification. Detailed clay XRD, which is a semiquantitative analysis that provides percent abundances of major clay mineral groups, was based on maximum peak intensity and area under the peak preferentially from the glycolated samples. Overall, the shipboard XRD results were interpreted qualitatively based on relative occurrences and abundances of the most common clay mineralogical components because the samples were not calibrated with a known amount of mineral standard.

Processed files include d-spacing values, diffraction angles, and peak intensities with background removed. Muscovite/illite/glauconite and kaolinite/chlorite have similar diffraction patterns and could not be distinguished with bulk XRD results. The results were then compared to expected d-spacing values for minerals in the DIFFRAC.EVA software using aluminum oxide as a standard to monitor data quality. Digital files with the diffraction patterns are available from the LIMS database.

2.8. X-ray fluorescence analyses

An Olympus Delta handheld pXRF spectrometer was used to conduct rapid reconnaissance (qualitative) analysis of element compositions on the split surfaces of the archive halves. We primarily utilized the Geochemistry correction protocol in the Geochemistry and soil submenu, which analyzes for elements in three energy ranges (low = Al, Si, K, Ca, Ti, Mn, Fe, Cr, P, S, and Mg; main = Ca, Ti, Mn, Fe, Ni, Sr, Rb, Zr, Zn, and others; high = Sr, Rb, Zr, Ba, La, and Ce). In general, the high-energy elements did not provide reliable results, but the main and low-range groupings yielded results that were sufficiently precise when concentrations were above instrument detection limits.

3. Igneous petrology

3.1. Physical characteristics of volcanic units

The procedures for core description outlined here are essentially similar to those developed during Integrated Ocean Drilling Program Expeditions 324 and 330 and the very recent IODP Expedition 391 (Expedition 324 Scientists, 2010; Expedition 330 Scientists, 2012; Sager et al., 2023). Boundaries of lithologic units were defined by either visual identification of actual lithologic contacts or by inference of the position of such contacts using observed changes in volcanic characteristics and/or volcaniclastic features. This was followed by general description of the lithology, lithologic variation, and characteristic igneous textures and vesicle distributions. These macroscopic observations were combined with those from detailed petrographic microscopy of the key igneous units. When possible and appropriate, these observations were complemented by thin section examination and bulk rock chemical analyses of representative samples using inductively coupled plasma–atomic emission spectroscopy (ICP-AES) (see **Geochemistry**; see also Geochemistry in the **Site U1579** and **Site U1580** chapters [Bohaty et al., 2023a, 2023b] for results and data tables). For a preliminary assessment, the pXRF spectrometer was also used to measure chemical elements on the split core surface of certain (fine-grained) intervals. These measurements, however, were only conducted qualitatively, and no external rock standard calibrations were performed (and thus no quantitative data are reported). All observations and data were recorded in the LIMS database.

3.1.1. Background

Effusive basaltic volcanism in both the subaerial and submarine environment produces a range of common features associated with the development and inflation of flow lobes of varying sizes, pillow lavas, pahoehoe or rubbly flow surfaces, and, where lava interacts directly with seawater, hyaloclastites and breccias. Submarine eruptions are dominated by stacks of budding and anastomosing pahoehoe-like extrusions, which result in piles of rounded or tubular masses (Batiza and White, 2000), the most readily recognized of which is the pillow basalt, often referred to as pillow lava. However, large, massive inflation units several meters thick and more laterally extensive extrusions have also been observed resulting in sheet-like morphologies (e.g., Lonsdale and Spiess, 1980; Mitchell et al., 2008).

3.1.2. Submarine volcanism and intrusions

Submarine lavas are important because they represent the most abundant surficial igneous rock on the surface of the Earth, forming by far the greater proportion of the ocean floors. Eruptive styles are largely controlled by effusion rate and are sensitive to local topography and slope onto which the lava eruption takes place (e.g., Gregg and Fink, 1995; Mitchell et al., 2008, and references therein). Basaltic magma is typically erupted at relatively high temperatures and characteristically is fluid (low viscosity), allowing the relatively high gas content to be released effectively during lava emplacement. These gases may leave traces as vesicle layers and pipes, which are often characteristic for submarine basaltic eruptions. However, due to increasing hydrostatic pressure with increasing depth of seafloor, the degree of vesiculation decreases in deeper water eruptions (Dixon et al., 1995; Wallace, 1998).

3.1.2.1. Pillow lavas

Pillow lavas are subaqueous extrusions resulting from individual budding, inflation, and separation of lava "pods" from point sources along the advancing lava front. They can accumulate in a variety of styles depending upon effusion rate, number of point sources, and internal plumbing architectures within the growing volcanic edifice. However, pillow lavas typically consist of discrete subrounded units of relatively small size (diameter = ~0.2 to <1.0 m), and characteristically, their exteriors are entirely bounded by glassy rinds as a result of rapid cooling; their interiors typically display internally radiating vesicle and joint patterns. In drill cores, pillow lavas therefore can be recognized by curved chilled margins oblique to the vertical axis of the pillow core, radial fractures that emanate from the massive core, or outer surfaces coated with glass. At water depths deeper than 3 km, the hydrostatic pressure exceeds the critical pressure of water, effectively preventing steam explosions. Accordingly, pillow basalt formed in the upper 1000 m of the water column often consists of moderately to highly vesicular lava, whereas pillow basalts formed in much deeper water can usually be distinguished from shallower water examples by a significantly lower vesicularity (<5% volume) and often by the presence of pelagic rather than siliciclastic marine sediment preserved between the pillows. A very close morphological similarity exists between pillow lava formed under water and pahoehoe lava formed on land, although the latter typically lack or else have only a relatively thin glassy rind (i.e., glassy surface selvage).

3.1.2.2. Massive or sheet-like flows

Massive or sheet-like flows are thick (as thick as several meters or more), laterally extensive units forming sheet-like, internally massive basalt flows (van Andel and Ballard, 1979). In dimension and internal features, they can resemble those of larger subaerially erupted flows. These types of flows may be fed by lava tubes and develop by internal inflation and/or marginal budding. They often have texturally uniform massive cores as thick as several meters with grain sizes increasing toward the flow center. They are often characterized by sparse vesicle layering or vertical vesicle pipes containing late-stage melt segregation material. Glassy margins are thin and usually not preserved during coring. Massive or sheet-like flows may be a response to particularly high effusion rates and/or local slope and other controlling topographic conditions. These unit types have been termed "sheet flow" in previous IODP reports, although this term implies a significant degree of lateral extension, which cannot be readily determined from core alone. Therefore, if recovered units are significantly thicker than the normal dimensions expected for pillow lava or lobate flows (~0.2–1 m), we employ the nongenetic term "massive lava unit."

3.1.2.3. Intrusive sheets

Intrusive sheets include both dikes and sills. They are tabular bodies that are usually distinguished from lava flows by having relatively planar contacts and quenched margins on both their upper and lower contacts. Dikes are further distinguished by contacts that crosscut primary depositional layering. Intrusive sheets typically have fewer vesicles, are significantly coarser grained in their interiors than lavas, and may have granular or doleritic textures (subophitic to ophitic or hypidiomorphic granular textures, seriate grain size distribution). Intrusive units can interact with the sediments they intrude into, "baking" the sediments near the contacts during high temperature–low pressure contact metamorphism. This can be a particularly distinguishing feature that when seen in sediments at the upper contact of igneous units is a likely indication of their intrusive nature. In practice, however, it can be difficult to distinguish intrusive sheets from massive lava flows (see further discussion in Igneous petrology in the **Site U1579** and **Site U1580** chapters [Bohaty et al., 2023a, 2023b]).

3.1.3. Lava-sediment interaction and volcaniclastic deposits

3.1.3.1. Lava-sediment interactions

Lava-sediment interactions include features involving mixing or mingling of molten or plastic lava with sediment and soft-sediment deformation features where lava injects or intrudes into a substrate. In some instances, there is a lack of bedding or lamination in sediments adjacent to pillow lavas or the materials surrounding lava injections. A likely explanation is fluidization of the fine-grained sediment, which is attributable to flash heating and vaporization of sediment pore water during emplacement of the pillow lava (Kokelaar, 1982). Such momentary fluidization causes sediment reconstitution, localized transport, and redistribution and, hence, the destruction of any inherent bedding structures. The term "peperite" describes a volcanic-sediment facies that forms when submarine basaltic lava flows interact with unconsolidated sediment (Skilling et al., 2002). The mingling of basaltic lavas and wet sediments produces distinct volcanic textures (entrainment, baking, chilling, etc.) as well as physical and chemical fragmentation and alteration through steam-rock interaction during flash heating of the water. Common features include quenched lava flow margins of basaltic clasts surrounded by sediment and basaltic clasts with a variety of fragment morphologies including fluidal (e.g., where fragments remained plastic enough to deform after deposition) or jigsaw fit (e.g., where fragments crack apart in situ). Palagonite (devitrified glass) is a typical alteration product and is commonly associated with peperite volcanic facies where small fragments of lava have reacted with steam. The occurrence of peperites is taken as evidence that the sedimentation and the volcanism existed contemporaneously.

3.1.3.2. Volcaniclastic deposits

Volcaniclastic deposits include a range of materials from rubbly, in situ volcanic debris to resedimented materials such as volcanic sands or tuffs. Expedition 392 volcaniclastic sediments contain aspects of sedimentology and igneous petrology but in most cases were composed of predominantly sedimentary volcaniclastic deposits. Where there were alternating igneous and volcaniclastic intervals, the igneous intervals are presented on the igneous VCDs with gaps where there were sedimentary volcaniclastics, and vice versa on the sedimentary VCDs, where igneous intervals were left out. It is often not possible to distinguish between pyroclastic and epiclastic deposits in ancient volcaniclastic deposits retrieved by coring. During Expedition 392, however, no significant intervals of volcaniclastic material were encountered. For a thin (30 cm) interval of coarse-grained and poorly sorted volcaniclastic sediment recovered between pillow lavas in Hole U1582B, we applied the term "hyaloclastic breccia" (angular clasts) and used lithologic or structural modifiers for further description. When >50% of the volcaniclastics were composed of glass or devitrified glass, the term "hyaloclastite" was used. This means "glass-fragment rock" and includes all glassy fragmental debris formed by eruptions in which water has been involved. Hyaloclastite production may include shallow-water phreatomagmatic eruptions and volcaniclastic materials associated with the advancement of submarine lavas at greater water depths (Clague et al., 2009). Phreatomagmatic conditions can result in the fragmentation of gas bubbles inflated by steam, producing thick layers of glass shards. In particular, pillow lavas may contain an extensive matrix of intrapillow hyaloclastite, and hyaloclastite pillow breccias may grade into pillow lava flows as the proportion of pillows increases. The glassy ash portion of hyaloclastite pillow breccias typically consists

of flat glass shards spalled off expanding pillows with keystone-shaped fragments derived from the pillow rims.

In addition, the occurrence of palagonite is common in hyaloclastites given the ubiquity of glass in these deposits. Palagonite is an alteration product of volcanic glass because it interacts with seawater and is commonly found either partially or fully replacing volcanic glass in hyaloclastites or in the margins of pillow basalts. Palagonite often appears as yellow, orange, or red waxy rinds and can be highly angular.

3.2. Definition of lithologic units and volcanic successions

Our primary aim was to design an observational framework that permitted logging and recording of key data and that avoided nomenclature or terminologies that connote particular styles of basaltic volcanism. Most lava type classifications are based on field observations, which consider both the lateral and vertical variations of eruptive units and their stacking relationships. Such refined classifications are neither realistic nor justifiable from core observation alone and can only become achievable through integration of multiple data streams alongside the recorded core log data (e.g., petrography, downhole logging data, geochemical and paleomagnetic results, etc.). Lithofacies associations provide one such avenue of nongenetic description and have been successfully applied to a range of large igneous province (LIP) types (e.g., Jerram and Widdowson, 2005; White et al., 2009; Greene et al., 2010). Accordingly, we have employed the term "lithostratigraphic unit" to describe successions of similar volcanic facies types such as pillow lava stacks, packages of sills or sheet flows, or hyaloclastic successions. Such overarching units may often be petrogenetically or volcanically related within a single eruptive event. However, in the case of basaltic successions, these types of volcanic and petrogenetic relationships often only become apparent later, through examination of additional petrographic, geochemical, or downhole logging data. In most instances, only smaller volcanic (cooling) unit divisions can be identified in core material, so these are necessarily the basic unit of description.

Therefore, to aid efficient core description and enable the later collation of the observed volcanic elements into volcanically meaningful successions, we adopted a simple two-fold numerical hierarchy. We identified the smaller features, or igneous units, based on criteria that included the presence of lava contacts, chilled margins or identifiable flow tops, vesicle distributions, and the occurrence of intercalated volcaniclastic or sedimentary horizons. The igneous units were identified during core description and given consecutive downhole Arabic numbering (Igneous Units 1, 2, 3, etc.) irrespective of whether they are pillow, massive flow types, or sills (a nongenetic cataloging system). A quick assessment of geochemical similarity and variation using pXRF (see below) can further help to distinguish different lithologic units when their distinction is not apparent otherwise. In addition, igneous subunits were sometimes used when changes in texture in a single igneous unit were significant enough but did not represent a separate cooling unit. These subunits (which may or may not recur within a single unit) were given lowercase letters preceded by the main igneous unit number in which they were found (Igneous Subunits 1a, 1b, 1c, etc.).

The term lithostratigraphic unit is then applied where successions of consecutive cooling or inflation of units of similar or shared evolutionary characteristics can be identified. In effect, these stratigraphic units combine similar types of eruptive products and provide a first step toward considering the volcanic stratigraphy in terms of packages of genetically related lithologic features and, ultimately, the evolving volcanism. These packages are given consecutive downhole Roman numbering (Lithostratigraphic Units III, IV, V, etc.) and follow on consecutively from the overlying sedimentary units (e.g., Lithostratigraphic Units I and II). During Expedition 392, alternations of igneous successions and sedimentary rocks were encountered in two holes (Holes U1579D and U1580A), and in accordance with the practice of sedimentary unit division (see **Lithostratigraphy**), each of these transitions was considered as a new lithostratigraphic unit (and assigned a new Roman number). For minor sedimentary intervals associated with the pillow lavas stack in Holes U1582A and U1582B (interpillow sediments), we have deviated from this rule.

Within an entirely igneous succession, the term lithostratigraphic unit should not be considered as synonymous with an individual eruptive event but rather as a method of dividing core into

elements or sections displaying broadly similar volcanic characteristics (which could still have a common age/geochemical composition).

The most unequivocal evidence for dividing core into smaller igneous units is the presence of flow-to-flow contacts; unfortunately, these are rarely preserved in low-recovery sections. Alternatively, the presence of glassy material or finer grained chill zones can also provide a useful proxy for determining the presence, or estimating the position of, unit boundaries. However, the interpretation of grain size changes in core can be ambiguous. The changes in vesiculation that occur through inflation or cooling units of all sizes are of particular use in sections of poor core recovery. To identify and estimate the position of lithologic unit boundaries using this method, we paid special attention to vesiculation characteristics by measuring, estimating, and otherwise recording (1) the percentage volume of vesicles, (2) the average size range, and (3) the sphericity. The volume fraction of vesicles in the unit or section under consideration, together with modal sphericity of the vesicle populations, were estimated using appropriate comparison charts similar to those used by the sedimentology laboratory group and derived from the Wentworth (1922) classification scheme. It proved impractical to measure the minimum size because these are often below the limit of visual resolution.

Lithologic descriptions followed accepted conventions. Porphyritic basaltic rocks were named according to major phenocryst type, but only in those instances where the total abundance of phenocrysts was >1%; aphyric rocks were not assigned any mineralogical modifier and instead retained a textural description (e.g., aphyric basalt). The term "phenocryst" was used for any crystal that was significantly (typically 5×) larger than the average size of the groundmass crystals, larger than 1 mm, and euhedral or subhedral in shape. The phenocryst abundance descriptors were further modified by including the names of phenocryst phases in order of decreasing abundance. For example, an olivine-plagioclase phyric basalt may contain 10% olivine and 4% plagioclase phenocrysts.

3.3. Core and thin section descriptions

The first step in describing the recovered core was identification of unit boundaries based on lithology changes, color, grain size, the presence of volcaniclastic or sedimentary intercalations, volcanological features (e.g., presence of contacts and chilled margins), vesicle distribution patterns, changes in primary mineralogy (occurrence and abundance of plagioclase, pyroxene, olivine, and oxide minerals), and alteration. Unit boundaries of volcanic rocks were chosen to reflect different volcanic cooling or volcaniclastic units (see **Definition of lithologic units and volcanic successions**). In some cases, limited recovery required interpolation for positioning of unit boundaries.

3.4. Macroscopic visual core description

We used IODP's descriptive data capture application DESClogik to document each section of igneous rock cores. To provide consistency in approach, the procedure and templates that we designed closely follow the methods for core descriptions from previous volcanic basement expeditions including Expeditions 324 and 330 and the recent Expedition 391.

VCDs were generated to summarize each section of the igneous rock cores (Figure **F5**). The VCD components, from left to right, include the depth in meters using the CSF-A depth scale; a scale for core section length of 0–150 cm, or as appropriate, the sample piece number; a scanned digital image of the core archive half; an orientation column (with upward pointing arrow indicating the occurrence of oriented pieces); the position of shipboard samples; the igneous unit number; symbolized structural information; a line chart displaying the recorded percent vesicularity; a stacked line chart displaying phenocryst content percentage; a line chart displaying variation in the crystal size of modal groundmass and the presence of glass (g) or altered glass (ag); a graphical pattern indicating alteration intensity; MS data; and color reflectance data.

Additionally, the VCD contains written descriptions to accompany the schematic representation of each igneous unit for the specific core section. These include the following information:

- Expedition; site and hole; core, type, and section number (e.g., 392-U1579D-62R Section 3); and the depth of the top of the core section measured using the CSF-A depth scale.
- Igneous unit number and the piece number(s) belonging to this unit in this section.
- Lithology: rock description and name. Rock descriptions were based on the examination of hand specimens using eye, hand lens, and binocular microscope observations.
- Volcanic description: based on the type or part of unit (pillow lava, massive flow, etc.). Units were identified using, for example, the presence of glassy margins, groundmass grain size variations, and vesicle-rich bands.
- Texture: whether the rock was aphyric (<1% phenocrysts), sparsely phyric (1%–5% phenocrysts), moderately phyric (5%–10% phenocrysts), or highly phyric (>10% phenocrysts).
- Descriptive modal color based on dry rock surfaces.
- Phenocryst type(s) and abundance in percent based on minerals identifiable by eye, hand lens, or binocular microscope.
- Groundmass grain size categories: aphanitic (glassy to microcrystalline) (<0.25 mm), fine grained (0.25–0.5 mm), medium grained (0.5–1 mm), coarse grained (1–2 mm), and very coarse grained (>2 mm). The presence of fresh/altered glass is indicated by the letters "g"/"ag."
- Vesicles: nonvesicular (0%–1%), sparsely vesicular (<5%), moderately vesicular (5%–20%), and highly vesicular (>20%). Any other defining characteristics (e.g., shape and sphericity, changes in vesicle sizes [i.e., fining- or coarsening upward], or other arrangement patterns) are noted as well.
- Upper and lower unit contact relations and boundaries: based on the physical changes observed in the retrieved core material (i.e., presence of chilled margins, changes in vesicularity, alteration, and so on), and information regarding their position within the section. "Not recovered" is entered where there is no direct contact recovered (e.g., if igneous contact is otherwise inferred using proxy observations such as a chilled margin or changes in vesicularity).
- Alteration: based on percent of alteration products by volume and categorized as follows: unaltered (<2%), slight (2%–10%), moderate (10%–40%), high (40%–80%), and very high to complete (80%–100%) alteration. Includes comments regarding degree and type of vesicle infilling.
- Comment: included as appropriate

3.5. Microscopic visual core description

Thin section analyses of selected intervals sampled from the cores were used to complement and refine macroscopic core observations. Typically, at least one thin section was examined and logged per defined lithostratigraphic unit. Additional thin sections from individual igneous units were taken as needed. Thin section reports were created to summarize the most significant information for each thin section, which was extracted with a program from the extensive observation workbooks in DESClogik and exported as a single-page PDF (Figure **F11**). JRSO personnel created the report definition in the report builder custom tool, updated the definition with input from scientists during the expedition, and generated batches of PDF reports upon request using the report writer tool. As far as practically possible, the same terminology and nomenclature hierarchy employed for the visual core compositional descriptions was also used for the thin section descriptions. The textural terms used are those defined by MacKenzie et al. (1982). Phenocryst and groundmass assemblages and their modal percentages, sizes and shapes, and vesicles/alteration phases were determined, and textural descriptions were identified.

3.6. X-ray fluorescence analyses

An Olympus Delta handheld pXRF was used to conduct rapid (qualitative) reconnaissance analysis of igneous rock compositions (on the archive-half split surfaces; see above). In addition, all rock powders prepared for ICP-AES analysis were also measured using pXRF. All measurements were conducted with the instruments' Geochemistry correction protocol in the Geochemistry mode (see **Geochemistry**) and recorded in the LIMS database. Quantitative measurements, however, were conducted using ICP-AES, and the results are reported and displayed in the respective site chapters.

THIN SECTION LABEL ID: **392-U1580A-53R-2-W 75/77-TSB-TS 18** Thin section no.: 18
Observer: PD Piece no.:
Unit/subunit: 7

Thin section summary: Sample U1580A-53R-2W 75/77 is a plagioclase-phyric basalt. Two large plagioclase phenocrysts are present and show glomerocryst-like texture though they also appear to have a single crystal habit. Large clinopyroxenes show subophitic texture enclosing plagioclase laths. Olivine was likely also a groundmass phase but is completely replaced by clay minerals.

Plane-polarized: Cross-polarized:

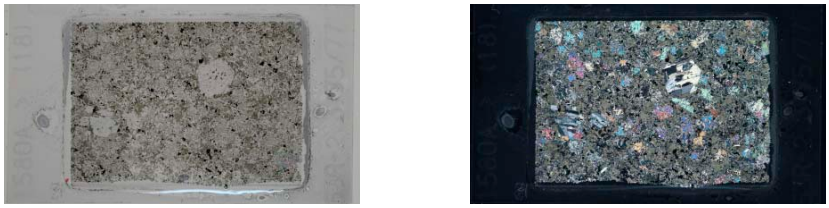

Igneous Petrology

Lithology: plagioclase phyric basalt
Groundmass grain size (avg.) medium-grained
Texture 1: subophitic
Texture 2: moderately phyric

Phenocrysts	Original (%)	Replaced (%)	Size mode (mm)	Size max. (mm)	Shape	Comments
Plagioclase	6	0	4.5	5	euhedral-subhedral	Shows glomerocryst-like texture though has a nice and singular habit

Groundmass	Original (%)	Replaced (%)	Size mode (mm)	Shape	Comments
Olivine	30	100	1	subhedral	
Plagioclase	35	5	0.6	euhedral-subhedral	
Clinopyroxene	30	10		anhedral	subophitic texture
Opaques	5	0	0.4	subhedral	

Vesicle	Original (%)	Filled (%)	Size mode (mm)	Size max. (mm)	Shape	Comments
Vesicle	0					

Figure F11. Example thin section report produced during Expedition 392. Data were recorded in the LIMS database using the DESClogik application and then compiled into these reports.

4. Micropaleontology

Calcareous nannofossils, planktonic and benthic foraminifera, marine diatoms, and organic-walled dinoflagellate cysts (dinocysts) and miospores provided preliminary shipboard biostratigraphy and paleoenvironmental information for the sediments recovered during Expedition 392. Biostratigraphic age assignments were primarily based on analyses of calcareous nannofossils, planktonic foraminifera, diatoms, and dinocysts. Microfossil samples were collected from most core catcher sections, and additional samples were occasionally taken both from section ends on the catwalk and split working-half sections to refine age estimates and to initially constrain critical time intervals.

Biostratigraphic zonation schemes for the microfossil groups analyzed in shipboard work are presented individually in the representative sections below and integrated in Figure **F12**. Age assignments are based on the 2020 Geologic Time Scale (GTS2020) of Gradstein et al. (2020) (Tables **T8**, **T9**, **T10**, **T11**). Biohorizons taken from other sources have been calibrated to GTS2020. Unless otherwise noted, biohorizon depths reported in the site chapter datum tables are given as the midpoint between the two samples bounding the biohorizon.

Data for each microfossil group are presented in the form of taxonomic distribution charts that record occurrences for samples examined from each hole. Relative abundance and preservation data were entered through the DESClogik application into the LIMS database for all identified microfossil taxa and paleontological data gathered during shipboard investigations. Shipboard biostratigraphic studies focused primarily on identifying biohorizons in the cores and are biased

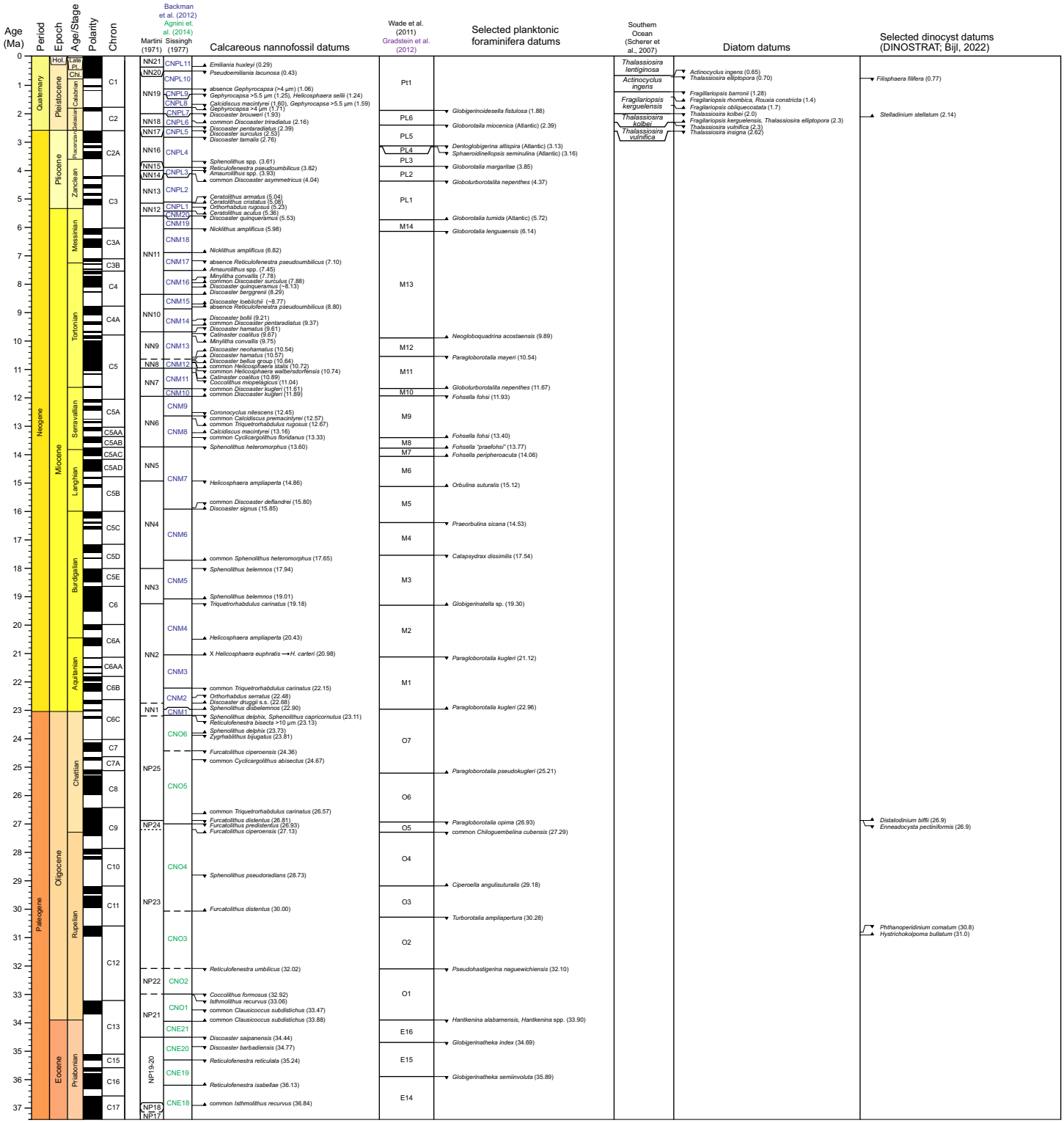

Figure F12. Microfossil datums used during Expedition 392, with calcareous nannofossil and planktonic foraminiferal zonation schemes for the Albian to recent and Southern Ocean diatom scheme for the Quaternary. (Continued on next two pages.)

toward reporting age-diagnostic species. Reported events include the top (T; last appearance datum) or base (B; first appearance datum) of a taxon's stratigraphic range, occasionally modified to identify the top common (Tc) or base common (Bc) occurrence within a taxon's range if it is more reliable for correlation and biostratigraphy. Additional biohorizons include crossovers in abundance (X) and acme events for taxa (base acme [Ba], top acme [Ta]). Tables in each site chap-

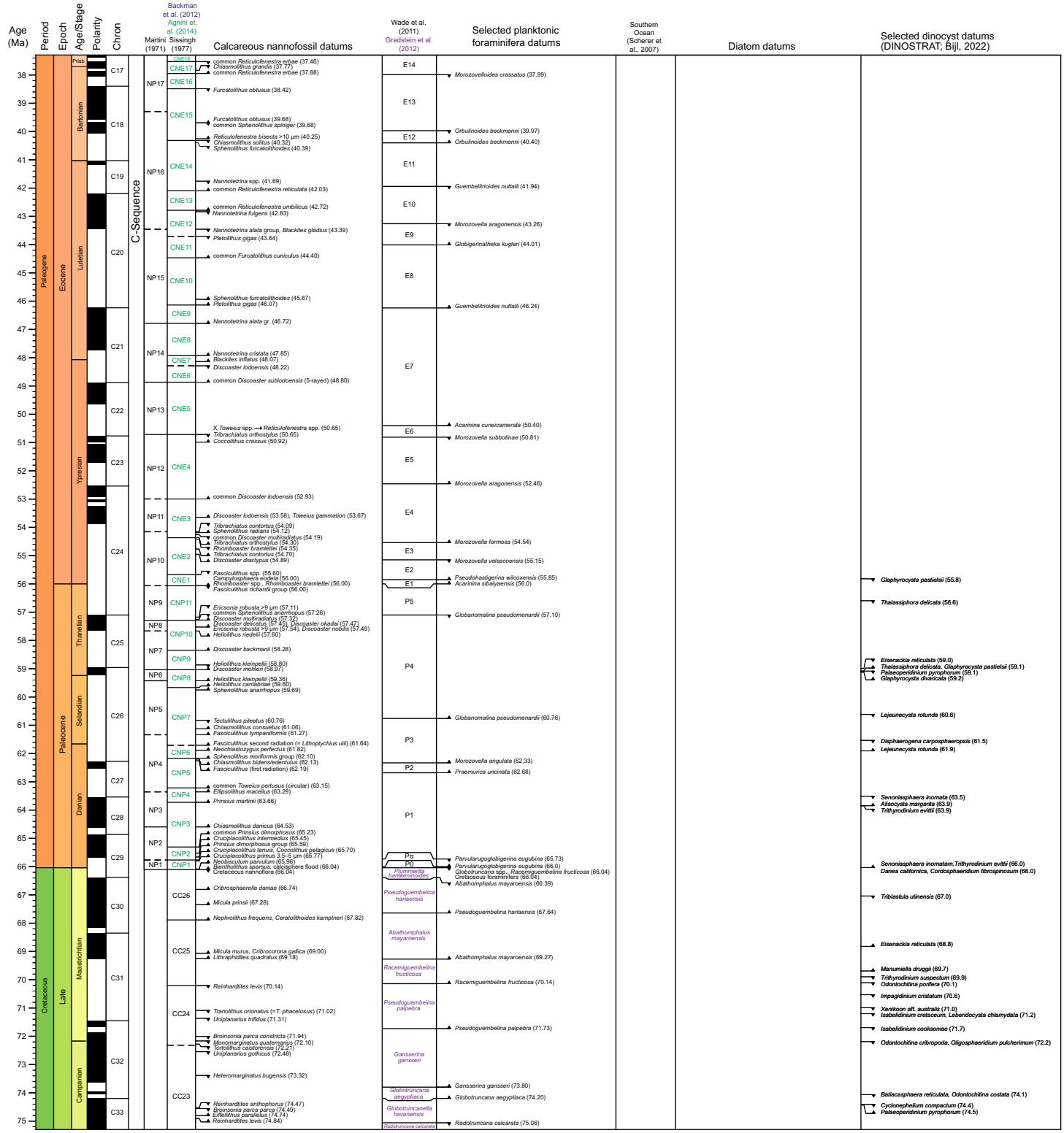

Figure F12 (continued). (Continued on next page.)

ter present the depth and age (with error/uncertainty for both, if available) of important biohorizons used to construct age-depth models. Biostratigraphic information is integrated with the magnetic polarity stratigraphy, if available, to produce an age model for each site that is presented in **Chronostratigraphy**. These age models are based on preliminary shipboard data and will be updated with postcruise research.

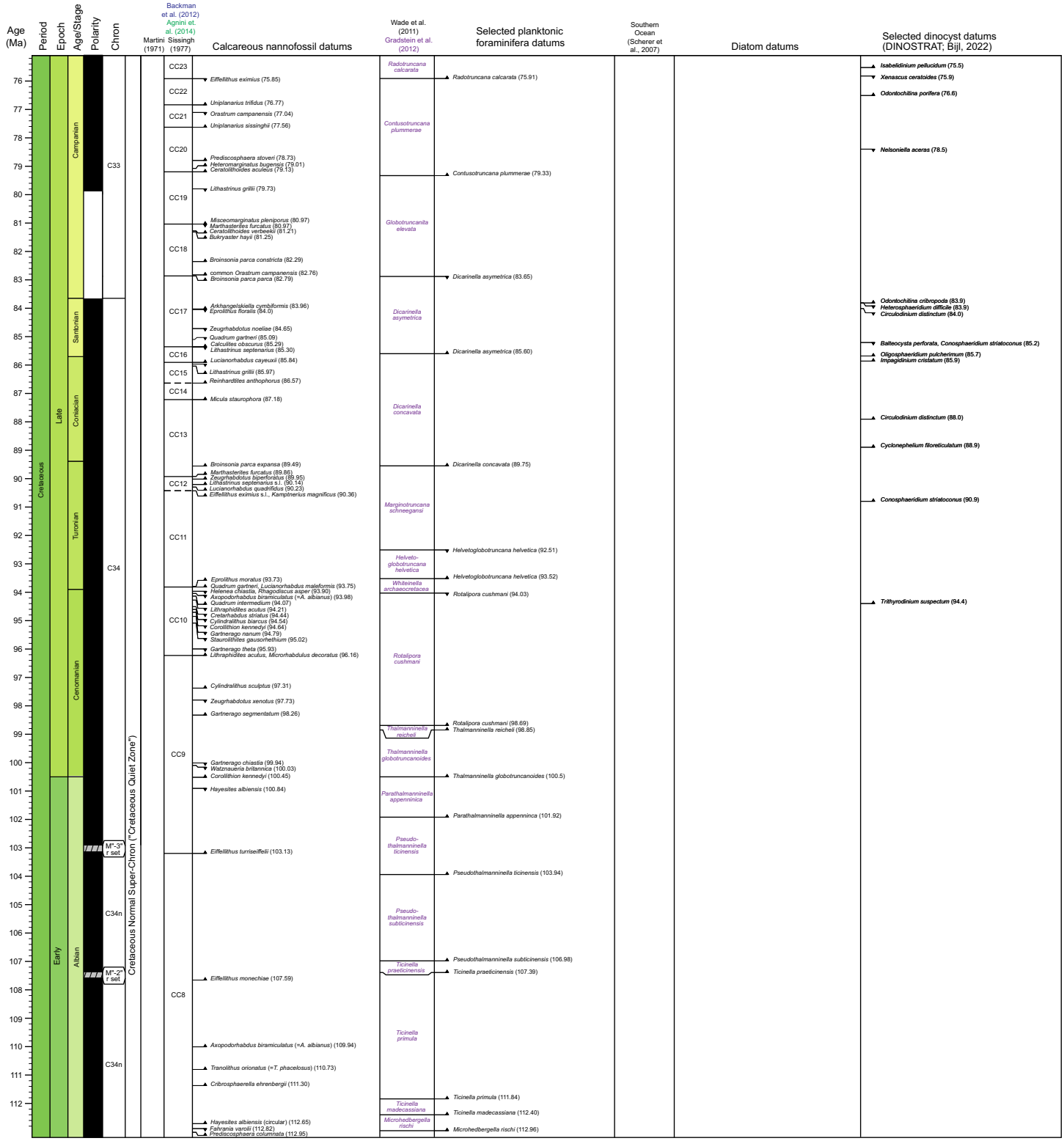

Figure F12 (continued).

4.1. Calcareous nannofossils

4.1.1. Calcareous nannofossil taxonomy and biostratigraphy

We primarily referred to the nannofossil taxonomy of Bown (1998, 2005) and Perch-Nielsen (1985a, 1985b) as compiled in the online Nannotax3 database (Young et al., 2022). The nannofossil biohorizons used for biostratigraphic classification are given in Table **T8**, together with the zonal scheme of Martini (1971) (zonal code numbers NP and NN). Additional biohorizons from the Paleogene and Neogene/Quaternary biozonation schemes of Agnini et al. (2014) (zonal code numbers CNP, CNE, and CNO) and Backman et al. (2012) (zonal code numbers CNM and CNPL) are also included, although they focus predominantly on mid- to low-latitude calcareous nannofossil assemblages. The compilation of Raffi et al. (2006) was also partially used to provide additional information on the reliability, definition, and timing of Quaternary bioevents. For the Mesozoic, the zonation of Sissingh (1977) (CC code) was used, as modified by Perch-Nielsen (1985b). However, many marker taxa are either absent or have different first or last appearance datums in Upper Cretaceous sediments of the high southern latitudes; this is particularly true for the upper Campanian and Maastrichtian (e.g., Wise, 1988; Pospichal and Wise, 1990; Crux, 1991; Watkins, 1992; Huber et al., 2019b; Watkins and Guerra, 2020; Petrizzo et al., 2022). Thus, ages derived from low- and middle-latitude sections, such as those included in Gradstein et al. (2020), may not be valid. Watkins et al. (1996) and do Monte Guerra et al. (2016) built on earlier studies to develop zonations for the Late Cretaceous southern high latitudes, although due to a paucity of magnetostratigraphic records, the zones and datums are not well dated. Here, we report Gradstein et al. (2020) ages for Cretaceous events when possible with the caveat that they generally represent Tethyan ages. This composite zonation scheme provides a general framework for calcareous nannofossil biostratigraphic classification (Figure **F12**).

Table T8. Age estimates of calcareous nannofossil datums based on low-latitude zonations, Expedition 392. TSC = Timescale Creator, UCL = UCL workshop on Late Cretaceous microfossil stratigraphy (June 2011). (Continued on next four pages.) **Download table in CSV format.**

Zone/Subzone base				
Martini, 1971	Backman et al., 2012; Agnini et al., 2014; Sissingh, 1977	Biohorizon	GTS2020 age (Ma)	Calibration reference
NN21		B *Emiliania huxleyi*	0.29	Thierstein et al., 1977; Rio et al., 1990
NN20	CNPL11	T *Pseudoemiliania lacunosa*	0.43	Thierstein et al., 1977; Backman et al., 2012
		Tc *Reticulofenestra asanoi*	0.91	Wei, 1993, Raffi, 2002
	CNPL10	T absence *Gephyrocapsa* >4 µm	1.06	Gartner, 1977; Raffi, 2002
		Bc *Reticulofenestra asanoi*	1.14	Wei, 1993, Raffi, 2002
		T *Helicosphaera sellii*	1.24	Raffi et al., 1993, Raffi et al., 2006 and references therein
	CNPL9	T *Gephyrocapsa* >5.5 µm	1.25	Raffi et al., 1993, Raffi et al., 2006 and references therein
		B *Gephyrocapsa* >5.5 µm	1.59	Raffi et al., 1993, Raffi et al., 2006 and references therein
		T *Calcidiscus macintyrei*	1.60	Raffi et al., 1993, Raffi et al., 2006 and references therein
	CNPL8	B *Gephyrocapsa* >4 µm	1.71	Raffi, 2002; Raffi et al., 2006
NN19	CNPL7	T *Discoaster brouweri*	1.93	Shipboard Scientific Party, 1995; Lourens et al., 2005
		Bc *Discoaster triradiatus*	2.16	Shipboard Scientific Party, 1995; Lourens et al., 2005
NN18	CNPL6	T *Discoaster pentaradiatus*	2.39	Shipboard Scientific Party, 1995; Lourens et al., 2005
NN17		T *Discoaster surculus*	2.53	Shipboard Scientific Party, 1995; Lourens et al., 2005
		Pliocene/Pleistocene boundary	2.59	Gradstein et al., 2020
	CNPL5	T *Discoaster tamalis*	2.76	Shipboard Scientific Party, 1995; Lourens et al., 2005
		T *Sphenolithus* spp.	3.61	Shipboard Scientific Party, 1995; Lourens et al., 2005
NN16	CNPL4	T *Reticulofenestra pseudoumbilicus* >7 µm	3.82	Shipboard Scientific Party, 1995; Lourens et al., 2005
NN15		T *Amaurolithus* spp.	3.93	Gradstein et al., 2020
NN14	CNPL3	Bc *Discoaster asymmetricus*	4.04	Backman et al., 2012
	CNPL2	T *Ceratolithus armatus* (=*Ceratolithus acutus*)	5.04	Backman and Raffi, 1997; Backman et al., 2012
NN13		B *Ceratolithus cristatus* (=*Ceratolithus rugosus*)	5.08	Backman and Raffi, 1997; Backman et al., 2012
		T *Orthorhabdus rugosus* (=*Triquetrorhabdulus rugosus*)	5.23	Backman and Raffi, 1997; Backman et al., 2012
		Miocene/Pliocene boundary	5.33	Gradstein et al., 2020
	CNPL1	B *Ceratolithus acutus*	5.36	Backman and Raffi, 1997; Backman et al., 2012
NN12	CNM20	T *Discoaster quinqueramus*	5.53	Backman and Raffi, 1997; Backman et al., 2012
	CNM19	T *Nicklithus amplificus*	5.98	Backman and Raffi, 1997; Backman et al., 2012
	CNM18	B *Nicklithus amplificus*	6.82	Raffi and Flores, 1995; Backman and Raffi, 1997; Backman et al. 2012
		T absence *Reticulofenestra pseudoumbilicus*	7.10	Raffi and Flores, 1995; Backman and Raffi, 1997; Backman et al. 2012
	CNM17	B *Amaurolithus* spp.	7.45	Raffi and Flores, 1995; Backman and Raffi, 1997; Zeeden et al., 2013
		T *Minylitha convallis*	7.78	Raffi et al., 2006

Table T8 (continued). (Continued on next page.)

Zone/Subzone base				
Martini, 1971	Backman et al., 2012; Agnini et al., 2014; Sissingh, 1977	Biohorizon	GTS2020 age (Ma)	Calibration reference
		Bc *Discoaster surculus*	7.88	Raffi et al., 1995; Raffi et al., 2006
		B *Discoaster quinqueramus*	8.13	Raffi et al., 1995; Gradstein et al., 2020
NN11	CNM16	B *Discoaster berggrenii*	8.29	Raffi et al., 2006; Zeeden et al., 2013
		B *Discoaster loeblichii*	8.77	Raffi et al., 1995; Gradstein et al., 2020
	CNM15	B absence *Reticulofenestra pseudoumbilicus*	8.80	Raffi et al., 2006; Backman et al., 2012
		T *Discoaster bollii*	9.21	Berggren et al., 1995a citing Gartner, 1992, and Miller et al., 1985
		Bc *Discoaster pentaradiatus*	9.37	Raffi et al., 1995; Raffi et al., 2003
NN10	CNM14	T *Discoaster hamatus*	9.61	Backman and Raffi, 1997; Zeeden et al., 2013
		T *Catinaster coalitus*	9.67	Backman and Raffi, 1997; Zeeden et al., 2013
		B *Minylitha convallis*	9.75	Backman and Raffi, 1997; Raffi et al., 2006; Backman et al., 2012
		B *Discoaster neohamatus*	10.54	Backman and Raffi, 1997; Zeeden et al., 2013
NN9	CNM13	B *Discoaster hamatus*	10.57	Backman and Raffi, 1997; Zeeden et al., 2013
		B *Discoaster bellus* group	10.64	Raffi et al., 1995; Zeeden et al., 2013
		Bc *Helicosphaera stalis*	10.72	Fornaciari et al., 1996; Hilgen et al., 2000
		Tc *Helicosphaera walbersdorfensis*	10.74	Theodoridis, 1984; Hilgen et al., 2000
NN8	CNM12	B *Catinaster coalitus*	10.89	Backman and Raffi, 1997; Zeeden et al., 2013
		T *Coccolithus miopelagicus*	11.04	Raffi et al., 1995; Backman and Raffi, 1997; Zeeden et al., 2013
	CNM11	Tc *Discoaster kugleri*	11.61	Raffi et al., 1995; Backman and Raffi, 1997; Backman et al., 2012; Zeeden et al., 2013
NN7	CNM10	Bc *Discoaster kugleri*	11.89	Raffi et al., 1995; Backman and Raffi, 1997; Backman et al., 2012; Zeeden et al., 2013
		T *Coronocyclus nitescens*	12.45	Raffi et al., 2006; Turco et al., 2002; Zeeden et al., 2013
	CNM9	Tc *Calcidiscus premacintyrei*	12.57	Raffi et al., 1993, Raffi et al., 2006; Backman et al., 2012
		Bc *Triquetrorhabdulus rugosus*	12.67	Raffi et al., 1995; Raffi et al. 2006
		B *Calcidiscus macintyrei*	13.16	Raffi et al., 1995; Turco et al. 2002; Zeeden et al., 2013
		Tc *Cyclicargolithus floridanus*	13.33	Raffi et al., 1995; Raffi et al. 2006; Zeeden et al., 2013
NN6	CNM8	T *Sphenolithus heteromorphus*	13.60	Backman and Raffi, 1997; Turco et al., 2002; Zeeden et al., 2013
NN5		T *Helicosphaera ampliaperta*	14.86	Shipboard Scientific Party, 1995; Backman et al., 2012
		Tc *Discoaster deflandrei*	15.80	Rio et al., 1990; Backman et al., 2012
	CNM7	B *Discoaster signus*	15.85	Rio et al., 1990; Backman et al., 2012
	CNM6	Bc *Sphenolithus heteromorphus*	17.65	Backman et al., 2012; Gradstein et al., 2020
NN4		T *Sphenolithus belemnos*	17.94	Backman et al., 2012
	CNM5	B *Sphenolithus belemnos*	19.01	Backman et al., 2012
NN3		T *Triquetrorhabdulus carinatus*	19.18	Backman et al., 2012
		B *Helicosphaera ampliaperta*	20.43	Shipboard Scientific Party, 1995; Backman et al., 2012
	CNM4	X *Helicosphaera euphratis*/*H. carteri*	20.98	Fornaciari, 1996; Backman et al. 2012; Gradstein et al., 2020
	CNM3	Tc *Triquetrorhabdulus carinatus*	22.15	Backman et al., 2012; Gradstein et al., 2020
		T *Orthorhabdus serratus*	22.48	Shipboard Scientific Party, 1993; Gradstein et al., 2020
NN2		B *Discoaster druggii* s.s.	22.68	Shipboard Scientific Party, 2002; Gradstein et al., 2020
	CNM2	B *Sphenolithus disbelemnos*	22.90	Rio et al., 1990; Fornaciari, 1996; Backman et al., 2012; Gradstein et al., 2020
		Oligocene/Miocene boundary	23.04	Gradstein et al., 2020
		T *Sphenolithus capricornutus*	23.11	Raffi, 1999; Liebrand et al., 2016
	CNM1	T *Sphenolithus delphix*	23.11	Raffi, 1999; Liebrand et al., 2016
NN1		T *Reticulofenestra bisecta* >10 µm	23.13	Shipboard Scientific Party, 1993; Gradstein et al., 2020
		B *Sphenolithus delphix*	23.73	Raffi, 1999; Liebrand et al., 2016
		T *Zygrhablithus bijugatus*	23.81	Miller et al., 1985; Berggren et al., 1995a; Gradstein et al., 2020
	CNO6	T *Furcatolithus ciperoensis*	24.36	Backman et al., 2012
		Tc *Cyclicargolithus abisectus*	24.67	Shipboard Scientific Party, 2002; Gradstein et al., 2020
		T *Chiasmolithus altus*	25.44	Wei and Thierstein, 1991; Berggren et al., 1995a
		Bc *Triquetrorhabdulus carinatus*	26.57	Blaj et al., 2009
NP25		T *Furcatolithus distentus*	26.81	Blaj et al., 2009
	CNO5	T *Furcatolithus predistentus*	26.93	Blaj et al., 2009
NP24		B *Furcatolithus ciperoensis*	27.13	Agnini et al., 2014
		early/late Oligocene boundary	27.82	
		T *Sphenolithus pseudoradians*	28.73	Poore et al., 1982; Berggren et al., 1995a; Gradstein et al., 2020
	CNO4	B *Furcatolithus distentus*	30.00	Blaj et al., 2009
NP23	CNO3	T *Reticulofenestra umbilicus* >14 µm	32.02	Blaj et al., 2009
NP22	CNO2	T *Coccolithus formosus*	32.92	Blaj et al., 2009
		T *Isthmolithus recurvus*	33.06	Gradstein et al., 2012; Villa et al., 2008; Gradstein et al., 2020
		Tc *Clausicoccus subdistichus*	33.47	Premoli Silva et al., 1987; Berggren et al., 1995a; Gradstein et al., 2020
	CNO1	Bc *Clausicoccus subdistichus*	33.88	Backman, 1987
		Eocene/Oligocene boundary	33.90	Gradstein et al., 2020
NP21	CNE21	T *Discoaster saipanensis*	34.44	Blaj et al., 2009
		T *Discoaster barbadiensis*	34.77	Blaj et al., 2009
	CNE20	T *Reticulofenestra reticulata*	35.24	Agnini et al., 2014
	CNE19	B *Reticulofenestra isabellae*	36.13	Agnini et al., 2014
NP19/NP20		Bc *Isthmolithus recurvus*	36.84	Forniaciari et al., 2010
	CNE18	Tc *Reticulofenestra erbae*	37.46	Forniaciari et al., 2010

Table T8 (continued). (Continued on next page.)

Zone/Subzone base				
Martini, 1971	Backman et al., 2012; Agnini et al., 2014; Sissingh, 1977	Biohorizon	GTS2020 age (Ma)	Calibration reference
		middle/late Eocene boundary	37.71	
		T *Chiasmolithus grandis*	37.77	Agnini et al., 2014
NP18		Bc *Chiasmolithus oamaruensis*	37.84	Agnini et al., 2014
	CNE17	Bc *Reticulofenestra erbae*	37.88	Forniaciari et al., 2010
	CNE16	T *Furcatolithus obtusus*	38.42	Forniaciari et al., 2010
		Tc *Sphenolithus spiniger*	39.68	Forniaciari et al., 2010
		B *Furcatolithus obtusus*	39.68	Forniaciari et al., 2010
	CNE15	B *Reticulofenestra bisecta* >10 µm	40.25	Agnini et al., 2014
NP17		T *Chiasmolithus solitus*	40.32	Exp. 320/321 Scientists, 2010; Berggren et al., 1995a; Gradstein et al., 2020
		T *Sphenolithus furcatolithoides*	40.39	Agnini et al., 2014
		T *Nannotetrina* spp.	41.69	Agnini et al., 2014
	CNE14	Bc *Reticulofenestra reticulata*	42.03	Agnini et al., 2014
	CNE13	Bc *Reticulofenestra umbilicus* >14 µm	42.72	Agnini et al., 2014
NP16		T *Nannotetrina fulgens*	42.83	Gradstein et al., 2020
		T *Nannotetrina alata* group	43.39	Backman, 1986
		T *Blackites gladius*	43.39	Berggren et al., 1995a; Gradstein et al., 2020
NP15c	CNE12	T *Pletolithus gigas*	43.64	Agnini et al., 2014
	CNE11	Bc *Furcatolithus cuniculus*	44.40	Agnini et al., 2014
		B *Sphenolithus furcatolithoides*	45.87	Agnini et al., 2014
NP15b	CNE10	B *Pletolithus gigas*	46.07	Agnini et al., 2006
NP15a	CNE9	B *Nannotetrina alata* group	46.72	Agnini et al., 2006
		early/middle Eocene boundary	47.80	
	CNE8	B *Nannotetrina cristata*	47.85	Agnini et al., 2006
NP14b		B *Blackites inflatus*	48.07	Gradstein et al., 2020
	CNE7	T *Discoaster lodoensis*	48.22	Agnini et al., 2006
NP14a	CNE6	Bc *Discoaster sublodoensis* (5-rayed)	48.80	Agnini et al., 2006
NP13	CNE5	T *Tribrachiatus orthostylus*	50.65	Agnini et al., 2006
		X *Toweius/Reticulofenestra*	50.65	Agnini et al., 2006
		B *Coccolithus crassus*	50.92	Agnini et al., 2014
	CNE4	Bc *Discoaster lodoensis*	52.93	Agnini et al., 2014
NP12		B *Discoaster lodoensis*	53.58	Agnini et al., 2007
		B *Toweius gammation*	53.67	Agnini et al., 2016
NP11		T *Tribrachiatus contortus*	54.09	Agnini et al., 2007
		B *Sphenolithus radians*	54.12	Agnini et al., 2007
		Tc *Discoaster multiradiatus*	54.19	Exp. 320/321 Scientists, 2010; Agnini et al., 2007; Gradstein et al., 2020
	CNE3	B *Tribrachiatus orthostylus*	54.30	Agnini et al., 2007
		T *Rhomboaster bramlettei*	54.35	Agnini et al., 2007
		B *Tribrachiatus contortus*	54.70	Berggren et al., 1995a; Agnini et al., 2007; Gradstein et al., 2020
		B *Discoaster diastypus*	54.89	Agnini et al., 2007
	CNE2	T *Fasciculithus* spp.	55.60	Agnini et al., 2007
NP10		B *Rhomboaster bramlettei*	56.00	Aubry et al., 2007; Gradstein et al., 2020
		B *Rhomboaster* spp.	56.00	Agnini et al., 2007
		B *Campylosphaera eodela*	56.00	Berggren et al., 1995a; Agnini et al., 2007; Gradstein et al., 2020
		Paleocene/Eocene boundary	56.00	Gradstein et al., 2020
	CNE1	T *Fasciculithus richardii* group	56.00	Agnini et al., 2007
		T *Ericsonia robusta* >9 µm	57.11	Agnini et al., 2007
		Tc *Sphenolithus anarrhopus*	57.26	Gradstein et al., 2020
NP9	CNP11	B *Discoaster multiradiatus*	57.32	Agnini et al., 2007
		B *Discoaster okadai*	57.47	Agnini et al., 2007
		B *Discoaster delicatus*	57.45	Agnini et al., 2007
		B *Ericsonia robusta* >9 µm	57.54	Agnini et al., 2007
		B *Discoaster nobilis*	57.49	Agnini et al., 2007
NP8		B *Heliolithus riedelii*	57.60	Agnini et al., 2007
	CMP10	B *Discoaster backmanii*	58.28	Gradstein et al., 2020
		T *Heliolithus kleinpellii*	58.80	Berggren et al., 1995a; Agnini et al., 2007; Gradstein et al., 2020
NP7	CNP9	B *Discoaster mohleri*	58.97	Agnini et al., 2007
		middle/late Paleocene boundary	59.20	
NP6		B *Heliolithus kleinpellii*	59.36	Agnini et al., 2007
	CNP8	B *Heliolithus cantabriae*	59.60	Agnini et al., 2007
		B *Sphenolithus anarrhopus*	59.69	Agnini et al., 2007
		T *Tectulithus pileatus*	60.76	Berggren et al., 1995a; Gradstein et al., 2020
		B *Chiasmolithus consuetus*	61.06	Berggren et al., 1995a; Gradstein et al., 2020
NP5		B *Fasciculithus tympaniformis*	61.27	Agnini et al., 2007
		early/middle Paleocene boundary	61.60	

Table T8 (continued). (Continued on next page.)

Zone/Subzone base				
Martini, 1971	Backman et al., 2012; Agnini et al., 2014; Sissingh, 1977	Biohorizon	GTS2020 age (Ma)	Calibration reference
	CNP7	B *Fasciculithus* second radiation (= B *Lithoptychius ulii*)	61.64	Agnini et al., 2007
		B *Neochiastozygus perfectus*	61.82	Agnini et al., 2007
	CNP6	B *Sphenolithus moriformis* group	62.10	Agnini et al. 2014
		B *Chiasmolithus bidens/edentulus*	62.13	Gradstein et al., 2020
		B *Fasciculithus* first radiation	62.19	Gradstein et al., 2020
	CNP5	Bc *Toweius pertusus* (circular)	63.15	Agnini et al., 2014
NP4		B *Ellipsolithus macellus*	63.29	Gradstein et al., 2020
	CNP4	B *Prinsius martinii*	63.66	Agnini et al. 2014
NP3		B *Chiasmolithus danicus*	64.53	Gradstein et al., 2020
	CNP3	Bc *Prinsius dimorphosus* group	65.23	Agnini et al. 2014
		B *Cruciplacolithus intermedius*	65.45	Gradstein et al., 2020
		B *Prinsius dimorphosus* group	65.59	Agnini et al., 2014
NP2		B *Cruciplacolithus tenuis*	65.70	Gradstein et al., 2020
	CNP2	B *Coccolithus pelagicus*	65.70	Agnini et al., 2014
		B *Cruciplacolithus primus* 3.5–5 µm	65.77	Gradstein et al., 2020
		B *Neobiscutum parvulum*	65.96	Gradstein et al., 2020
NP1	CNP1	B *Biantholithus sparsus*, Ba Calcispheres	66.04	Gradstein et al., 2020
		Cretaceous/Paleogene boundary	66.04	Gradstein et al., 2020
		T *Micula murus* and other Cretaceous nannofossils	66.04	Agnini et al., 2014, Gradstein et al., 2020
		B *Cribrosphaerella daniae*	66.74	Burnett, 1998; Voigt et al., 2012
	CC26b	B *Micula prinsii*	67.28	Gradstein et al., 2020
		B *Ceratolithoides kamptneri*	67.82	Gradstein et al., 2020
	CC26a	B *Nephrolithus frequens*	67.82	Gradstein et al., 2020
	CC25c	B *Micula murus*	69.00	Huber et al., 2008
	CC25	B *Cribrocorona gallica*	69.00	von Salis, 1998 (SEPM chart)
	CC25b	B *Lithraphidites quadratus*	69.18	Huber et al., 2008; Voigt et al., 2012
	CC25a	T *Reinhardtites levis*	70.14	Voigt et al., 2012; Watkins (pers. comm., 2011)
	CC24	T *Tranolithus orionatus* (=*Tranolithus phacelosus*)	71.02	Gradstein et al., 2020
		T *Uniplanarius trifidus*	71.31	Burnett, 1998
		T *Broinsonia parca constricta*	71.94	Gradstein et al., 2020
		T *Monomarginatus quaternarius*	72.10	Gradstein et al., 2020
		Campanian/Maastrichtian boundary	72.17	Gradstein et al., 2020
		T *Tortolithus caistorensis*	72.21	Gradstein et al., 2020
		T *Uniplanarius gothicus*	72.48	Gradstein et al., 2020
		T *Heteromarginatus bugensis*	73.32	Gradstein et al., 2020
		T *Reinhardtites anthophorus*	74.47	Gradstein et al., 2020
		T *Broinsonia parca parca*	74.49	Gradstein et al., 2020
		B *Eiffellithus parallelus*	74.74	Burnett, 1998
		B *Reinhardtites levis*	74.84	von Salis, 1998 (SEPM chart)
	CC23	T *Eiffellithus eximius*	75.85	Gradstein et al., 2020
	CC22	B *Uniplanarius trifidus*	76.77	Gradstein et al., 2020
		T *Orastrum campanensis*	77.04	Gradstein et al., 2020
	CC21	B *Uniplanarius sissinghii*	77.56	Gradstein et al. 2020
		B *Prediscosphaera stoveri*	78.73	Gradstein et al., 2020
		B *Heteromarginatus bugensis*	79.01	Burnett, 1998
	CC20	B *Ceratolithoides aculeus*	79.13	Gradstein et al., 2020
		T *Lithastrinus grillii*	79.73	Burnett, 1998
		T *Marthasterites furcatus*	80.97	von Salis, 1998 (SEPM chart)
	CC19	B *Misceomarginatus pleniporus*	80.97	Burnett, 1998
		B *Ceratolithoides verbeekii*	81.21	Burnett, 1998
		B *Bukryaster hayi*	81.25	Burnett, 1998
		B *Broinsonia parca constricta*	82.29	Gradstein et al., 2020
		Bc *Orastrum campanensis*	82.76	Burnett, 1998
	CC18	B *Broinsonia parca parca*	82.79	Gradstein et al., 2020
		Santonian/Campanian boundary	83.65	Gradstein et al., 2020
		B *Arkhangelskiella cymbiformis*	83.96	Gradstein et al., 2020
		T *Eprolithus floralis*	84.0	von Salis, 1998 (SEPM chart); Watkins and Guerra, 2020
		T *Zeugrhabdotus noeliae*	84.65	Gradstein et al., 2020
		T *Quadrum gartneri*	85.09	Gradstein et al., 2020
	CC17	B *Calculites obscurus*	85.29	Gradstein et al., 2020
		T *Lithastrinus septenarius*	85.30	Gradstein et al., 2020
		Coniacian/Santonian boundary	85.70	Gradstein et al., 2020
	CC16	B *Lucianorhabdus cayeuxii*	85.84	Gradstein et al., 2020
		B *Lithastrinus grillii*	85.97	Gradstein et al., 2020
	CC15	B *Reinhardtites anthophorus*	86.57	Gradstein et al., 2020

Table T8 (continued).

Zone/Subzone base				
Martini, 1971	Backman et al., 2012; Agnini et al., 2014; Sissingh, 1977	Biohorizon	GTS2020 age (Ma)	Calibration reference
	CC14	B *Micula staurophora*	87.18	Gradstein et al., 2020
		B *Broinsonia parca expansa*	89.49	Gradstein et al., 2020
		Turonian/Coniacian boundary	89.83	Gradstein et al., 2020
	CC13	B *Marthasterites furcatus*	89.86	von Salis, 1998 (SEPM chart); Gradstein et al., 2020
		B *Zeugrhabdotus biperforatus*	89.95	Gradstein et al., 2020
		B *Lithastrinus septenarius* (sensu lato)	90.14	Gradstein et al., 2020
		B *Lucianorhabdus quadrifidus*	90.23	Gradstein et al., 2020
	CC12	B *Eiffellithus eximius* (sensu lato)	90.36	Gradstein et al., 2020
		B *Kamptnerius magnificus*	90.36	Gradstein et al., 2020
		B *Marthasterites furcatus* (high latitude)	93.64	Burnett, 1998; Gradstein et al., 2020
		B *Eprolithus moratus*	93.73	Gradstein et al., 2020
	CC11	B *Quadrum gartneri*	93.75	Gradstein et al., 2020
		B *Lucianorhabdus maleformis*	93.75	Gradstein et al., 2020
		Cenomanian/Turonian boundary	93.90	Gradstein et al., 2020
	CC10b	T *Helenea chiastia*	93.90	UCL
		T *Rhagodiscus asper*	93.90	Gradstein et al., 2020
		T *Axopodorhabdus biramiculatus* (=*Axopodorhabdus albianus*)	93.98	Gradstein et al., 2020
		B *Quadrum intermedium*	94.07	Gradstein et al., 2020
		T *Lithraphidites acutus*	94.21	Gradstein et al., 2020
		T *Cretarhabdus striatus*	94.44	Burnett, 1998
		T *Cylindralithus biarcus*	94.54	Burnett, 1998
		T *Corollithion kennedyi*	94.64	Burnett, 1998
		T *Gartnerago nanum*	94.79	Burnett, 1998
		T *Staurolithites gausorhethium*	95.02	Burnett, 1998
		T *Gartnerago theta*	95.93	Burnett, 1998
	CC10a	B *Lithraphidites acutus*, *Microrhabdulus decoratus*	96.16	Burnett, 1998
		B *Cylindralithus sculptus*	97.31	Burnett, 1998
		T *Zeugrhabdotus xenotus*	97.73	Burnett, 1998
		B *Gartnerago segmentatum*	98.26	Burnett, 1998
		T *Gartnerago chiasta*	99.94	Burnett, 1998
		T *Watznaueria britannica*	100.03	Burnett, 1998
		B *Corollithion kennedyi*	100.45	UCL
		Albian/Cenomanian boundary	100.50	Gradstein et al., 2020
	CC9b	T *Hayesites albiensis*	100.84	Kanungo, 2005
	CC9a	B *Eiffellithus turriseiffelii*	103.13	Gale et al., 2011
		B *Eiffellithus monechiae*	107.59	Bralower et al., 1997
		B *Axopodorhabdus biramiculatus* (=*Axopodorhabdus albianus*)	109.94	Grippo et al., 2004
	CC8b	B *Tranolithus orionatus* (=*Tranolithus phacelosus*)	110.73	Bralower et al., 1997; Grippo et al., 2004
		B *Cribrosphaerella ehrenbergii*	111.30	von Salis, 1998 (SEPM chart)
		B *Hayesites albiensis*	112.65	Grippo et al., 2004; Huang et al., 2010
		T *Fahrania varolii*	112.82	(from TSC graph)
	CC8a	B *Prediscosphaera columnata* (circular)	112.95	Gradstein et al. 2020

Several biohorizons approximate critical events and chronostratigraphic boundaries as follows:

- Pliocene/Pleistocene boundary (2.588 Ma): recognized between biohorizon top *Discoaster tamalis* (2.76 Ma) and biohorizon top *Discoaster surculus* (2.53 Ma).
- Miocene/Pliocene boundary (5.33 Ma): identified between biohorizon base *Ceratolithus acutus* (5.36 Ma) and biohorizon top *Orthorhabdus rugosus* (=*Triquetrorhabdulus rugosus*; 5.23 Ma).
- Oligocene/Miocene boundary (23.04 Ma): recognized between biohorizon top *Sphenolithus delphix* (23.11 Ma) and biohorizon base *Sphenolithus belemnos* (22.90 Ma).
- Eocene/Oligocene boundary (33.90 Ma): falls between biohorizon top *Discoaster saipanensis* (34.44 Ma) and biohorizon base common *Clausicoccus subdistichus* (33.88 Ma).
- Paleocene/Eocene boundary (56.00 Ma) and Paleocene/Eocene Thermal Maximum (PETM): recognized between biohorizon top *Fasciculithus richardii* group (base of Zone CNE1; 56.00 Ma) and biohorizon base *Rhomboaster* spp. (including *Rhomboaster bramlettei*; 56.00 Ma).

- Cretaceous/Paleogene (K/Pg) boundary (66.04 Ma): recognized by biohorizon top Cretaceous nannoflora (top of Zone NC23, base of Zone NP1) together with biohorizon base *Biantholithus sparsus* (base of Zone NP1) and acme of calcispheres.
- Campanian/Maastrichtian boundary (72.17 Ma): approximated by biohorizon top *Monomarginatus quaternarius* (72.10 Ma).
- Santonian/Campanian boundary (83.65 Ma): approximated by biohorizon top *Eprolithus floralis* (84.00 Ma).
- Coniacian/Santonian boundary (85.70 Ma): approximated by biohorizon top *Lithastrinus septenarius* (85.30 Ma).
- Turonian/Coniacian boundary (89.83 Ma): recognized between biohorizon base *Marthasterites furcatus* (89.86 Ma) and biohorizon base *Micula staurophora* (87.18 Ma).
- Cenomanian/Turonian boundary (93.90 Ma) and Oceanic Anoxic Event (OAE) 2: recognized between biohorizon tops *Axopodorhabdus biramiculatus* (=*Axopodorhabdus albianus*; 93.98 Ma) and *Helenea chiastia* (93.90 Ma) and biohorizon bases *Quadrum gartneri* (93.75 Ma) and *Eprolithus moratus* (93.73 Ma).

Members of *Gephyrocapsa* dominate Pleistocene assemblages; however, this group demonstrates a large range of variation in size and morphology, causing problems in identification (e.g., Samtleben, 1980; Su, 1996; Bollmann, 1997). Early work by Samtleben (1980), Rio (1982), and Matsuoka and Okada (1990) established the utility of biometric variations in *Gephyrocapsa* for Pleistocene biostratigraphy. Since then, many studies have confirmed biometric subdivisions of *Gephyrocapsa* as reliable biostratigraphic markers (e.g., Raffi et al., 1993, 2006; Young, 1998; Raffi, 2002; Maiorano and Marino, 2004; Lourens et al., 2005), and we have elected to use this biometric classification. We used the following divisions for shipboard identification of *Gephyrocapsa*:

- *Gephyrocapsa* spp. <4 µm (small): includes a number of different species (e.g., *Gephyrocapsa ericsonii* and *Gephyrocapsa ornata*, as well as small specimens of *Gephyrocapsa oceanica* and *Gephyrocapsa caribbeanica*).
- Medium-sized *Gephyrocapsa* (4–5.5 µm): identified to species level based on the size and morphology of the central area: *G. oceanica* (large central area with bridge angle <90° to the minor axis) and *G. caribbeanica* (small central area nearly filled by a bridge). *Gephyrocapsa omega* and *Gephyrocapsa muellerae* were included with *G. oceanica*.
- *Gephyrocapsa* spp. >5.5 µm (large): includes large specimens of both *G. oceanica* and *G. caribbeanica*.

Reticulofenestra evolved in the early Eocene and quickly dominated nannoplankton assemblages throughout the world's oceans for the remainder of the Paleogene and Neogene. Species within this genus are distinguished based on the size and shape of the coccolith as well as the size and structure of the central area; however, these parameters show considerable variations within and between "species," which can make differentiation difficult (e.g., Backman, 1980; Su, 1996; Young, 1998). Although some species are easily distinguishable, elliptical forms are particularly problematic, especially because different names have been applied to similar morphologies from the Paleogene and the Neogene. Here we define the taxonomy we applied for members of this genus.

Elliptical forms <3 µm with variable central opening size are defined as follows:

- *Reticulofenestra minuta*.

Elliptical forms >3 µm with open central area are defined as follows:

- *Reticulofenestra minutula*: open central area 3–5 µm in length.
- *Reticulofenestra pseudoumbilicus*: used for Neogene sediments; divided into two size categories following the definition of Young (1998) for biostratigraphic utility:
  - *R. pseudoumbilicus* (5–7 µm).
  - *R. pseudoumbilicus* (>7 µm); the top (3.70 Ma) of this form marks the Zone NN15/NN16 boundary.
- *Reticulofenestra dictyoda*: used for Paleogene sediments; an open central area 5–14 µm in length.

- *Reticulofenestra umbilicus*: forms >14 µm with open central area. The base of this taxon marks the base of Zone NP16 and its top marks the base of Zone NP23 in low and middle latitudes. In the southern high latitudes, the top of *R. umbilicus* is in Zone NP23.

Elliptical forms >3 µm with closed central area are defined as follows:

- *Reticulofenestra producta*: closed central area 3–5 µm in length.
- *Reticulofenestra perplexa*: closed central area 5–8 µm in length.
- *Reticulofenestra scrippsae*: closed central area 8–10 µm in length.
- *Reticulofenestra bisecta*: closed central area >10 µm in length; The top of this taxon (23.13 Ma) is very close to the Oligocene/Miocene boundary.

4.1.2. Methods of calcareous nannofossil study

Most samples for examination of calcareous nannofossils were prepared as standard smear slides (Bown and Young, 1998). For sandy or organic-rich sediments, strewn slides were prepared by thoroughly mixing a few cubic millimeters of sediment in 5–25 mL of deionized water buffered to a pH of ~8.5 with ammonium hydroxide and Triton X to lower the surface tension. After mixing, the sample was allowed to sit for 30–60 s for larger particles to settle out. A pipette was used to transfer the overlying suspension to a cover glass, which was dried on a low temperature on a warming plate. Once dry, cover glasses were affixed to the microscope slide using Norland optical adhesive Number 61 (refractive index = 1.56) and then cured under ultraviolet light. Samples were analyzed using a Zeiss Axioplan, Axiophot, or AxioImager microscope with cross-polarized, plane-transmitted, and/or phase-contrast light at 630×, 1000×, or 1250× magnification. Abundance estimates were made at 1000× magnification. When necessary, additional toothpick samples were taken between core catcher samples from split core sections to refine the stratigraphic position of biohorizons. All light microscope images were taken using a Spot RTS imaging system with the IODP Image Capture and Spot commercial software. Selected samples were observed using a Hitachi TM3000 bench-top SEM to verify the preservation state of calcareous nannofossils and confirm the presence of small forms such as *Emiliania huxleyi*, which are difficult to confidently identify using transmitted-light microscopy. All light microscope and SEM images were uploaded to the LIMS database.

Total calcareous nannofossil group abundance in the sediment was recorded as follows:

- D = dominant (>90% of sediment particles).
- A = abundant (>50%–90% of sediment particles).
- C = common (>10%–50% of sediment particles).
- F = few (1%–10% of sediment particles).
- R = rare (<1% of sediment particles).
- B = barren (no specimens).

Individual calcareous nannofossil taxa abundance was recorded as follows:

- D = dominant (>100 specimens per field of view [FOV]).
- A = abundant (>10–100 specimens per FOV).
- C = common (>1–10 specimens per FOV).
- Fr = frequent (1 specimen per 1–5 FOVs; used for Sites U1580–U1582).
- F = few (1 specimen per 5–10 FOVs; for Site U1579 defined as 1 specimen per 1–10 FOVs).
- R = rare (1 specimen per >10 FOVs).
- ? = questionable occurrence.
- rw = reworked occurrence.

Shipboard observations of calcareous nannofossil assemblages focused on the presence of age-diagnostic species. Distribution data therefore do not represent the full nannofossil assemblage. All nannofossil semiquantitative abundance data produced on board *JOIDES Resolution* were entered into DESClogik and are available from the LIMS database.

Calcareous nannofossil preservation was recorded as follows:

- G = good (little or no evidence of dissolution or recrystallization, primary morphological characteristics only slightly altered, and specimens identifiable to the species level).
- M = moderate (specimens exhibit some etching or recrystallization, primary morphological characteristics somewhat altered, and most specimens identifiable at species level).
- P = poor (specimens were severely etched or overgrown, primary morphological characteristics largely destroyed, fragmentation has occurred, and specimens often could not be identified at the species or genus level).

4.2. Foraminifera

4.2.1. Planktonic foraminiferal taxonomy and biostratigraphy

We used the biostratigraphic zonation scheme of Wade et al. (2011) for the Cenozoic. For the Cretaceous, we followed the zonation in Gradstein et al. (2012), which is a composite from Huber et al. (2008), Huber and Leckie (2011), and Petrizzo et al. (2011), updated to the GTS2020. The planktonic foraminifera zonal scheme used during Expedition 392 is illustrated in Figure **F12**, and age estimates for foraminifera datums are listed in Table **T9**.

Table T9. Age estimates of planktonic and benthic foraminifera datums, Expedition 392. * = benthic foraminifera species, LAD = last appearance datum, UCL = UCL workshop on Late Cretaceous microfossil stratigraphy (June 2011). (Continued on next three pages.) **Download table in CSV format.**

Wade et al. (2011)	Gradstein et al. (2012)	Species event	GTS2020 age (Ma)	Calibration reference (2020)
		T *Globorotalia flexuosa*	0.07	Berggren et al., 1995b
		B *Globigerinella calida*	0.22	Chaproniere et al., 1994
		B *Globorotalia flexuosa*	0.4	Berggren et al., 1995b
		B *Globorotalia hirsuta*	0.45	Pujol and Duprat, 1983
Pt1b		T *Globorotalia tosaensis*	0.61	Mix et al., 1995
		B *Globorotalia hessi*	0.74	Chaproniere et al., 1994
		X random to dextral in *Pulleniatina*	0.8	Pearson, 1995
		T *Globoturborotalita obliquus*	1.3	Chaisson and Pearson, 1997
		T *Globoturborotalita apertura*	1.64	Chaisson and Pearson, 1997
Pt1a		T *Globigerinoidesella fistulosa*	1.88	Chaisson and Pearson, 1997
		B *Globorotalia truncatulinoides*	1.93	Chaisson and Pearson, 1997
		T *Globigerinoides extremus*	1.98	Chaisson and Pearson, 1997
		B *Pulleniatina finalis*	2.04	Chaisson and Pearson, 1997
		T *Globorotalia exilis* (Atl.)	2.09	Chaisson and Pearson, 1997
		B *Pulleniatina* (reappearance) (Atl.)	2.26	Chaisson and Pearson, 1997
		T *Globorotalia pertenuis*	2.3	Chaisson and Pearson, 1997
		T *Globoturborotalita woodi*	2.3	Chaisson and Pearson, 1997
PL6		T *Globorotalia miocenica* (Atl.)	2.39	Chaisson and Pearson, 1997
		T *Globorotalia limbata*	2.39	Chaisson and Pearson, 1997
		Pliocene/Pleistocene boundary	2.588	
		T *Globoturborotalita decoraperta*	2.75	Chaisson and Pearson, 1997
		T *Globorotalia multicamerata*	2.98	Chaisson and Pearson, 1997
PL5		T *Dentoglobigerina altispira* (Atl.)	3.13	Chaisson and Pearson, 1997
PL4		T *Sphaeroidinellopsis seminulina* (Atl.)	3.16	Chaisson and Pearson, 1997
		B *Globigerinoides fistulosus*	3.33	Berggren et al., 1995b
		B *Globorotalia tosaensis*	3.35	Berggren et al., 1995b
		T *Pulleniatina* (disappearance) (Atl.)	3.41	Chaisson and Pearson, 1997
		B *Globorotalia pertenuis*	3.52	Chaisson and Pearson, 1997
		B *Globorotalia miocenica* (Atl.)	3.77	Chaisson and Pearson, 1997
		T *Globorotalia plesiotumida*	3.77	Chaisson and Pearson, 1997
PL3		T *Globorotalia margaritae*	3.85	Chaisson and Pearson, 1997
		X *Pulleniatina* coiling sinistral to dextral	4.08	Chaisson and Pearson, 1997
		B *Globorotalia crassaformis* sensu lato	4.31	Chaisson and Pearson, 1997
PL2		T *Globoturborotalita nepenthes*	4.37	Chaisson and Pearson, 1997
		B *Globorotalia exilis*	4.45	Chaisson and Pearson, 1997
		T *Sphaeroidinellopsis kochi*	4.53	Chaisson and Pearson, 1997
		T *Globorotalia cibaoensis*	4.61	Berggren et al., 1995a
		Miocene/Pliocene boundary	5.33	Gradstein et al., 2020
		B *Sphaeroidinella dehiscens* sensu lato	5.53	Chaisson and Pearson, 1997
PL1		B *Globorotalia tumida* (Atl.)	5.72	Chaisson and Pearson, 1997
		B *Turborotalita humilis*	5.81	Chaisson and Pearson, 1997
		T *Globoquadrina dehiscens*	5.91	Berggren et al., 1995b

Table T9 (continued). (Continued on next page.)

Wade et al. (2011)	Gradstein et al. (2012)	Species event	GTS2020 age (Ma)	Calibration reference (2020)
		B *Globorotalia margaritae*	6.08	Chaisson and Pearson, 1997
M14		T *Globorotalia lenguaensis*	6.14	Berggren et al., 1995b
		B *Globigerinoides conglobatus*	6.2	Chaisson and Pearson, 1997
		B *Pulleniatina primalis*	6.56	Berggren et al., 1995a
		X *Neogloboquadrina atlantica* coiling dextral to sinistral	6.97	Berggren et al., 1995a
M13		B *Neogloboquadrina acostaensis*	9.89	Berggren et al., 1995a
M12		T *Paragloborotalia mayeri*	10.54	Chaisson and Pearson, 1997
M11		B *Globoturborotalita nepenthes*	11.67	Turco et al., 2002
M10		T *Fohsella fohsi*	11.93	Chaisson and Pearson, 1997
M9		B *Fohsella fohsi*	13.4	Chaisson and Pearson, 1997
M8		B *Fohsella praefohsi*	13.77	Chaisson and Pearson, 1997
M7		B *Fohsella peripheroacuta*	14.06	Turco et al., 2002
M6		B *Orbulina suturalis*	15.12	Berggren et al., 1995a
M5		T *Praeorbulina sicana*	14.53	Shackleton et al., 1999
M4		T *Catapsydrax dissimilis*	17.54	Shackleton et al., 1999
M3		B *Globigerinatella* sp.	19.3	Pearson and Chaisson, 1997
M2		T *Paragloborotalia kugleri*	22.96	Shackleton et al., 1999
		B *Globoquadrina dehiscens*	22.50	Berggren et al., 1995a
M1		B *Paragloborotalia kugleri*	22.96	Shackleton et al., 1999
		Oligocene/Miocene boundary	23.04	Gradstein et al., 2020
		Tc *Trilobatus primordius*	23.50	Berggren et al., 1995a
		T *Tenuitella gemma*	23.53	Berggren et al., 1995a
O7		B *Paragloborotalia pseudokugleri*	25.21	Berggren et al., 1995a
		B *Trilobatus primordius*	26.12	Berggren et al., 1995a
O6		T *Paragloborotalia opima* sensu stricto	26.93	Wade et al., 2007
O5		Tc *Chiloguembelina cubensis*	28.09	Wade et al., 2007
O4		B *Ciperoella angulisuturalis*	29.18	Berggren et al., 1995a
		T *Subbotina angiporoides*	29.84	Berggren et al., 1995a
O3		T *Turborotalia ampliapertura*	30.28	Berggren et al., 1995a
		T Subbotina utilisindex	29.18	Wade et al. 2018
		B Subbotina utilisindex	30.28	Wade et al. 2018
		B *Paragloborotalia opima*	30.71	Berggren et al., 1995a
O2		T *Pseudohastigerina naguewichiensis*	32.10	Berggren et al., 1995a
		B *Cassigerinella chipolensis*	33.89	Gradstein et al., 2020
		Eocene/Oligocene boundary	33.90	Gradstein et al., 2020
O1		T *Hantkenina* spp., *Hantkenina alabamensis*	33.90	Berggren and Pearson, 2005
		T common *Pseudohastigerina micra*	33.90	Wade and Pearson, 2008
		T *Turborotalia cerroazulensis*	34.07	Berggren and Pearson, 2005
E16		T *Globigerinatheka index*	34.69	Berggren and Pearson, 2005
		B *Turborotalia cunialensis*	35.58	Berggren and Pearson, 2005
E15		T *Globigerinatheka semiinvoluta*	35.89	Berggren and Pearson, 2005
		B *Bolivina pontis**	36.29	Gradstein et al., 2020
		T *Acarinina* spp.	37.39	Gradstein et al., 2020
		T *Acarinina collactea*	37.95	Gradstein et al., 2020
		T *Subbotina linaperta*	37.96	Gradstein et al., 2020
E14		T *Morozovelloides crassatus*	37.99	Wade, 2004
		B *Globigerinatheka semiinvoluta*	38.40	Wade, 2004
		T *Planorotalites* spp.	38.40	Gradstein et al., 2020
		T *Acarinina primitiva*	38.99	Gradstein et al., 2020
		T *Turborotalia frontosa*	39.35	Berggren et al., 1995a
E13		T *Orbulinoides beckmanni*	39.97	Wade, 2004
E12		B *Orbulinoides beckmanni*	40.40	Berggren et al., 1995a
		T *Acarinina bullbrooki*	40.40	Berggren et al., 1995a
E11		T *Guembelitrioides nuttalli*	41.94	Berggren and Pearson, 2005
		B *Globigerinatheka index*	42.57	Berggren et al., 1995a
E10		T *Morozovella aragonensis*	43.26	Berggren et al., 1995a
E9		B *Globigerinatheka kugleri*	44.01	Pearson et al., 2004
		B *Hantkenina singanoae*	44.74	Payros et al., 2009
E8		B *Guembelitrioides nuttalli*	46.24	Payros et al., 2009
E7b		B *Turborotalia frontosa*	48.62	Payros et al., 2009
		B *Elphidium saginatum**	49.66	Gradstein et al., 2020
		B *Acarinina pentacamerata*	49.89	Gradstein et al., 2020
E7a		B *Acarinina cuneicamerata*	50.40	Hancock et al., 2002
		B *Planorotalites palmerae*	50.40	Berggren et al., 1995a
E6		T *Morozovella subbotinae*	50.81	Berggren and Pearson, 2005
E5		B *Morozovella aragonensis*	52.46	Berggren et al., 1995a
		T *Morozovella marginodentata*	52.74	Berggren et al., 1995a
		T *Morozovella lensiformis*	52.98	Berggren et al., 1995a
		T *Morozovella aequa*	54.12	Berggren et al., 1995a

Table T9 (continued). (Continued on next page.)

Wade et al. (2011)	Gradstein et al. (2012)	Species event	GTS2020 age (Ma)	Calibration reference (2020)
		B *Elphidium hampdenense**	54.53	Gradstein et al., 2020
E4		B *Morozovella formosa*	54.54	Gradstein et al., 2020
		B *Morozovella lensiformis*	54.54	Berggren et al., 1995a
E3		T *Morozovella velascoensis*	55.15	Berggren and Pearson, 2005
		T *Morozovella acuta*	55.34	Berggren et al., 1995a
		B *Morozovella gracilis*	55.34	Berggren et al., 1995a
		B *Muricella broedermanni*	55.34	Berggren et al., 1995a
		B *Morozovella marginodentata*	55.50	Berggren et al., 1995a
E2		B *Pseudohastigerina wilcoxensis*	55.85	Berggren and Pearson, 2005
E1		B *Acarinina sibaiyaensis*	56.00	Berggren and Pearson, 2005
		Paleocene/Eocene boundary	56.00	Gradstein et al., 2020
		B *Morozovella subbotinae*	57.10	Berggren et al., 1995a
		B *Acarinina coalingensis*	57.79	Berggren et al., 1995a
		B *Morozovella aequa aequa*	57.79	Berggren et al., 1995a
P5		T *Globanomalina pseudomenardii*	57.10	Berggren et al., 1995a
P4		B *Globanomalina pseudomenardii*	60.76	Berggren et al., 2000
P3		B *Morozovella angulata*	62.33	Berggren et al., 1995a
P2		B *Praemurica uncinata*	62.68	Berggren and Pearson, 2005
P1		T *Parvularugoglobigerina eugubina*	65.73	Berggren et al., 1995a
P_		B *Parvularugoglobigerina eugubina*	66.00	Gradstein et al., 2020
		Cretaceous/Paleogene boundary	66.04	Gradstein et al., 2020
P0		T *Globotruncana* spp., T *Racemiguembelina fructicosa*; LADs of other Cretaceous foraminifera	66.04	Berggren et al., 1995a; Berggren and Pearson, 2005
	Plummerita hantkeninoides	T *Abathomphalus mayaroensis*	66.39	Huber et al., 2008; Robaszynski, 1998 (SEPM chart)
		T *Gansserina gansseri*	66.47	Huber et al., 2008
		T *Contusotruncana patelliformis*	66.70	Huber et al., 2008
	Pseudoguembelina hariaensis	B *Pseudoguembelina hariaensis*	67.64	Huber et al., 2008
		T *Globotruncana bulloides*	68.35	Huber et al., 2008
		T *Globotruncana linneiana*	68.37	Huber et al., 2008
		T *Contusotruncana fornicata*	69.13	Huber et al., 2008
	Abathomphalus mayaroensis	B *Abathomphalus mayaroensis*	69.27	Huber et al., 2008
		B *Pseudotextularia elegans*	69.55	Huber et al., 2008
		B *Planoglobulina acervulinoides*	70.06	Huber et al., 2008
	Racemiguembelina fructicosa	B *Racemiguembelina fructicosa*	70.14	Huber et al., 2008
		T *Globotruncana ventricosa*	70.14	Robaszynski, 1998 (SEPM chart)
		B *Contusotruncana contusa*	71.02	Huber et al., 2008
		B *Racemiguembelina powelli*	71.48	Huber et al., 2008
	Pseudoguembelina palpebra	B *Pseudoguembelina palpebra*	71.73	Huber et al., 2008
		B *Pseudoguembelina kempensis*	71.89	Huber et al., 2008
		Campanian/Maastrichtian boundary	72.17	Gradstein et al., 2020
		B *Planoglobulina acervulinoides*	72.93	Huber et al., 2008; Robaszynski, 1998 (SEPM chart)
	Gansserina gansseri	B *Gansserina gansseri*	73.80	Huber et al., 2008; Robaszynski, 1998 (SEPM chart)
		B *Pseudoguembelina excolata*	74.00	Huber et al., 2008; Robaszynski, 1998 (SEPM chart)
	Globotruncana aegyptiaca	B *Globotruncana aegyptiaca*	74.20	Huber et al., 2008; Robaszynski, 1998 (SEPM chart)
	Globotruncanella havanensis	T *Radotruncana calcarata*	75.06	Huber et al., 2008
		B *Pseudotextularia elegans*	75.06	Robaszynski, 1998 (SEPM chart)
		B *Globigerinelloides impensus*	75.36	Huber et al., 2018
		B *Globotruncanella havanensis*	75.48	Robaszynski, 1998 (SEPM chart)
	Radotruncana calcarata	B *Radotruncana calcarata*	75.91	Huber et al., 2008
	Contusotruncana plummerae	B *Contusotruncana plummerae*	79.33	Huber et al., 2008
		B *Globotruncana ventricosa* (rare)	79.90	Robaszynski, 1998 (SEPM chart); Petrizzo et al., 2011
		B *Pseudoguembelina costulata*	81.54	Robaszynski, 1998 (SEPM chart)
		T *Ventilabrella eggeri*	82.13	Robaszynski, 1998 (SEPM chart)
		Santonian/Campanian boundary	83.65	Gradstein et al., 2020
	Globotruncanita elevata	T *Dicarinella asymetrica*	83.65	Robaszynski, 1998 (SEPM chart)
		T *Dicarinella concavata*, *Sigalia deflaensis*	83.65	Robaszynski, 1998 (SEPM chart)
		B *Globotruncanita elevata*	84.14	Robaszynski, 1998 (SEPM chart)
		T *Sigalia decoratissima decoratissima*	84.29	Robaszynski, 1998 (SEPM chart)
		T *Sigalia carpathica*	85.07	Robaszynski, 1998 (SEPM chart)
	Dicarinella asymetrica	B *Dicarinella asymetrica*	85.60	Gale et al., 2007
		Coniacian/Santonian boundary	85.70	Gradstein et al., 2020
		B *Sigalia carpathica*	85.77	Gradstein et al., 2020
		T *Whiteinella archaeocretacea*	85.79	Gale et al., 2007
		T *Whiteinella paradubia*	85.79	Gale et al., 2007
		B *Pseudotextularia nuttalli*	89.39	Robaszynski, 1998 (SEPM chart)
	Dicarinella concavata	B *Dicarinella concavata*	89.75	Shipboard Scientific Party, 1998

Table T9 (continued).

Wade et al. (2011)	Gradstein et al. (2012)	Species event	GTS2020 age (Ma)	Calibration reference (2020)
		Turonian/Coniacian boundary	89.83	Gradstein et al., 2020
	Marginotruncana schneegansi	T *Helvetoglobotruncana helvetica*	92.51	UCL
	Helvetoglobotruncana helvetica	B *Helvetoglobotruncana helvetica*	93.52	UCL
		Cenomanian/Turonian boundary	93.90	Gradstein et al., 2020
	Whiteinella archaeocretacea	T *Rotalipora cushmani*	94.03	Robaszynski, 1998 (SEPM chart)
		B *Whiteinella archaeocretacea*, *Heterohelix globulosa* (=*reussi*)	94.13	Robaszynski, 1998 (SEPM chart)
		T *Thalmanninella reicheli*, *Parathalmanninella appenninica*, *Thalmanninella globotruncanoides*	98.69	Robaszynski, 1998 (SEPM chart)
	Rotalipora cushmani	B *Rotalipora cushmani*	98.69	Robaszynski, 1998 (SEPM chart)
	Thalmanninella reicheli	B *Thalmanninella reicheli*	98.85	Robaszynski, 1998 (SEPM chart)
		Albian/Cenomanian boundary	100.50	Gradstein et al., 2020
		T *Pseudothalmanninella ticinensis*, *Ticinella primula*	100.50	Robaszynski, 1998 (SEPM chart)
		T *Planomalina buxtorfi*	100.85	Robaszynski, 1998 (SEPM chart)
	Parathalmanninella appenninica	B *Parathalmanninella appenninica*	101.92	Grippo et al., 2004; Gale et al., 2011
		B *Planomalina buxtorfi*	101.92	Grippo et al., 2004; Gale et al., 2011
		T *Pseudothalmanninella subticinensis*	102.42	Robaszynski, 1998 (SEPM chart)
	Pseudothalmanninella ticinensis	B *Pseudothalmanninella ticinensis*	103.94	Grippo et al., 2004; Gale et al., 2011
	Pseudothalmanninella subticinensis	B *Pseudothalmanninella subticinensis*	106.98	Robaszynski, 1998 (SEPM chart)
	Ticinella praeticinensis	B *Ticinella praeticinensis*	107.39	Grippo et al., 2004
		B *Biticinella breggiensis*	107.59	Robaszynski, 1998 (SEPM chart)
	Ticinella primula	B *Ticinella primula*	111.84	Grippo et al., 2004; Huang et al., 2010
	Ticinella madecassiana	B *Ticinella madecassiana*	112.40	Huber and Leckie, 2011
	Microhedbergella rischi	B *Microhedbergella rischi*	112.96	Huber and Leckie, 2011

Planktonic foraminiferal taxonomy follows Huber (1991), Olsson et al. (1999), Pearson et al. (2006), and Wade et al. (2018). Biohorizons approximating critical events and chronostratigraphic boundaries are as follows:

- Eocene/Oligocene boundary (33.90 Ma): falls at the base of Zone O1, defined by biohorizon tops *Hantkenina alabamensis* and *Hantkenina* spp. (33.90 Ma).
- PETM (Paleocene/Eocene boundary) (56.00 Ma): coincides with the base of Zone E1 and biohorizon bases *Acarinina sibaiyaensis* and *Globanomalina australiformis* (56.00 Ma).
- K/Pg boundary (66.04 Ma): coincides with the *Planohedbergella impensa* interval as described in Huber et al. (2018, 2022).

4.2.2. Benthic foraminiferal taxonomy

Species identifications for benthic foraminifera were conducted on the >150 µm size fraction examined under a Zeiss Discovery V8 stereomicroscope. Genera were assigned following Loeblich and Tappan (1988), and the standard foraminifera literature was consulted for species identification. Taxonomic assignments mainly follow Van Morkhoven et al. (1986), Hornibrook et al. (1989), Jones and Brady (1994), and Kaminski and Gradstein (2005).

4.2.3. Methods of study for foraminiferal assemblages

All sediment samples were wet sieved over a series of 63 and 150 µm size wire mesh sieves. For samples suspected to contain assemblages with very small foraminifera, for example, after an extinction event such as in the PETM for benthic foraminifera (Schmidt et al., 2018) and planktonic foraminifera in the Maastrichtian (e.g., Abramovich and Keller, 2003), a 20 and/or 45 µm size wire mesh was added to the set of sieves. The samples were subsequently dried over filter paper in a low-temperature (<60°C) oven and analyzed using standard stereomicroscope techniques using a Zeiss Discovery V8. The sieves were ultrasonicated at regular intervals to avoid contamination of samples. Lithified sediment samples that did not disaggregate after soaking in water alone were soaked in a 10% hydrogen peroxide solution for 30–60 min before wet sieving. Disaggregation in water with borax (or Calgon) and/or 10% H_2O_2 was applied in strongly lithified samples when needed. After removal from the sediment and identification to the species level whenever possible,

well-preserved specimens were photographed using a Hitachi TM3000 SEM. All images were uploaded to the LIMS database.

The preservation status of planktonic and benthic foraminifera was estimated as follows:

- VG = very good (no evidence of overgrowth, dissolution, or abrasion).
- G = good (little evidence of overgrowth, dissolution, or abrasion).
- M = moderate (calcite overgrowth, dissolution, or abrasion are common but minor).
- P = poor (substantial overgrowth, dissolution, or fragmentation).

Planktonic foraminiferal abundance relative to total sediment in the 20–45, 45–63, 63–150, and/or >150 µm fraction was estimated from visual examination of the sieved residue as follows:

- D = dominant (>30% of sediment particles).
- A = abundant (>10%–30% of sediment particles).
- F = few (>5%–10% of sediment particles).
- R = rare (>1%–5% of sediment particles).
- P = present (<1% of sediment particles).
- B = barren.

Benthic foraminiferal abundance relative to total sediment in the 20–45, 45–63, 63–150, and/or >150 µm fraction was estimated from visual examination of the sieved residue as follows:

- D = dominant (>30% of sediment particles).
- A = abundant (>10%–30% of sediment particles).
- F = few (>5%–10% of sediment particles).
- R = rare (>1%–5% of sediment particles).
- P = present (<1% of sediment particles).
- B = barren.

Planktonic to benthic ratio (P/[P + B]) determinations were made for as many samples as possible to evaluate relative changes in paleobathymetry (Ingle, 1980). Notes were also made about significant presences of fish teeth, radiolarians, ostracods, and other sedimentary and biogenic particles. These observations were entered in DESClogik in the planktonic foraminifera template using the same abundance codes.

4.3. Siliceous microfossils

4.3.1. Siliceous microfossils zonal scheme and taxonomy

Diatoms and silicoflagellates were analyzed to assist in preliminary age and paleoenvironmental assessment. Diatoms were identified to the species level where possible. Additionally, the occurrence of radiolarians and sponge spicules were documented at the group level for those interested in postcruise analysis and shore-based studies.

The initial shipboard diatom-based ages of Neogene, Paleogene, and Cretaceous samples were based on identification of primary and secondary datum events. Diatom zonal schemes and relevant papers for taxonomic studies for the Neogene/Quaternary, Paleogene, and Cretaceous are discussed separately in the sections below. The global zonation presented in Scherer et al. (2007) was used for general assessment, but detailed analysis/zonal schemes from the sections below provided a more robust framework that was used to build a biostratigraphic framework for Expedition 392. Where possible, biostratigraphic zones were also defined utilizing schemes derived from Southern Ocean and mid-latitude studies, primarily using the zonal scheme of Harwood and Maruyama (1992). Biostratigraphically useful taxa and datum age calibrations are listed in Table **T10**.

4.3.1.1. Neogene and Quaternary

For the Neogene, the Harwood and Maruyama (1992) zonal scheme was used with some updates from the northern belt of the Southern Ocean (Zielinski and Gersonde, 2002). Ages from all previously described Neogene and Quaternary zonal schemes were updated to the GTS2020 (Table **T10**). Age calibrations of Cody et al. (2008) and Florindo et al. (2013) were used for Miocene–

Pleistocene sediments, and we followed the taxonomic concepts of marker species specified comprehensively in appendices 1a and 1b of Cody et al. (2008).

4.3.1.2. Paleogene and Cretaceous

Recent advancements in biostratigraphy in the Atlantic extend calibrated records into the Paleogene for global distributions of both diatoms and silicoflagellates (Barron et al., 2015; Renaudie et al., 2018). Ages of taxa from supplemental table 1 of Barron et al. (2015), updated to the GTS2020, were used for Eocene marker species from Southern Ocean and South Atlantic records. Additionally, for the Cretaceous–Paleogene transition, the compilation of diatom datums following Renaudie et al. (2018) was used. Cretaceous zonal schemes and diatom occurrence data from Southern Hemisphere sites including Seymour Island (Santonian to Danian; Harwood et al., 1988), DSDP Site 275 (Santonian to Campanian; Hajós and Stradner, 1975), and ODP Hole 748B (Maastrichtian; Harwood and Nikolaev, unpubl. data) were used for Late Cretaceous diatom biostratigraphy. Because species-level identification was not possible for the Paleogene–Cretaceous pyritized diatoms found in Site U1581 sediments, zonal schemes were not applied.

Table T10. Age estimates of diatom datums used during Expedition 392. LAD = last appearance datum, FAD = first appearance datum. **Download table in CSV format.**

Southern Ocean events zone	Diatom event	Type	GTS2020 Age (Ma)
	Thalassiothrix longissima	LAD	Extant
	Actinocyclus octonarius	LAD	Extant
	Thalassiosira oliverana	LAD	Extant
	Thalassiosira lentiginosa	LAD	Extant
	Dactyliosolen antarcticus	LAD	Extant
	Fragilariopsis kerguelensis	LAD	Extant
	Fragilariopsis ritscheri	LAD	Extant
	Rhizosolenia hebetata	LAD	Extant
	Thalassiosira antarctica	LAD	Extant
	Actinocyclus actinochilus	LAD	Extant
	Shionodiscus tetraoestrupii	LAD	Extant
	Porosira pseudodenticulata	LAD	Extant
	Chaetoceros bulbosum	LAD	Extant
	Azpeitia tabularis	LAD	Extant
	Asteromphalus hookeri	LAD	Extant
	Thalassiosira tumida	LAD	Extant
	Asteromphalus parvulus	LAD	Extant
	Fragilariopsis obliquecostata	LAD	Extant
	Fragilariopsis rhombica	LAD	Extant
	Thalassionema nitzschioides	LAD	Extant
	Eucampia antarctica	LAD	Extant
	Fragilariopsis separanda	LAD	Extant
	Fragilariopsis cylindrus	LAD	Extant
	Shionodiscus gracilis	LAD	Extant
	Fragilariopsis sublinearis	LAD	Extant
	Fragilariopsis curta	LAD	Extant
	Corethron pennatum	LAD	Extant
Thalassiosira lentiginosa	*Rouxia leventerae*	LAD	0.1
	Hemidiscus karstenii	LAD	0.2
	Rouxia constricta	LAD	0.3
Actinocyclus ingens	*Actinocyclus ingens*	LAD	0.65
	Thalassiosira elliptopora	LAD	0.7
	Thalassiosira fasciculatus	LAD	0.8
Fragilariopsis kerguelensis	*Fragilariopsis barronii*	LAD	1.28
	Thalassiosira maculata	FAD	1
	Fragilariopsis rhombica, Rouxia constricta	FAD	1.4
	Rouxia antarctica	LAD	1.5
	Thalassiosira tetraoestrupii v. *reimeri*	LAD	1.6
	Fragilariopsis obliquecostata	FAD	1.7
	Thalassiosira inura	LAD	1.8
	Thalassiosira torokina	LAD	1.9
	Fragilariopsis separanda	FAD	1.9
Thalassiosira vulnifica	*Thalassiosira kolbei*	LAD	2
Thalassiosira kolbei	*Fragilariopsis kerguelensis*	FAD	2.3

4.3.2. Methods of study for siliceous microfossils

Diatoms (marine and freshwater), silicoflagellates, and sponge spicules were analyzed from smear slides mounted with Norland optical adhesive No. 61 (refractive index = 1.56). Samples with rare to common overall abundance of siliceous microfossils were either disaggregated in distilled water or processed with H_2O_2 and/or 10%–30% HCl. Strewn slides were prepared from these samples, and, when necessary, the cleaned material was washed over a 15 µm sieve to improve viewing. Species identification was carried out with a Zeiss AxioImager microscope using brightfield illumination at 400×, 630× (oil), and 1000× (oil) magnification. The counting method of Schrader and Gersonde (1978) was utilized for all diatom specimens.

Abundance of individual taxa was quantified by a count tallied over a 40 mm traverse of smear and strewn slides using 630× magnification. Photomicrographs were taken using a Spot FLEX imaging system with IODP Image Capture and commercial Spot software and a Hitachi TM3000 SEM. All images were uploaded to the LIMS database. Qualitative siliceous microfossil group abundances were also determined from smear and strewn slides using 630× magnification. These observations were entered into DESClogik using the diatom template. Radiolarian occurrences were also noted in this database for those interested in postcruise work on radiolarians. The relative abundance of diatoms was qualitatively estimated at 630× magnification using the following codes:

- A = abundant (>5 complete valves per FOV).
- C = common (2–5 complete valves per FOV).
- F = few (1 complete valve in 1–5 FOVs).
- R = rare (1 complete valve in 6–30 FOVs).
- Tr = trace (very rare valves or diatom fragments).
- B = barren (no diatom valves or fragments observed).

Relative abundances of individual diatom taxa were estimated at 630× magnification (one transect = 40 mm) using the following codes:

- D = dominant (>10 valves per FOV).
- A = abundant (>5 and <10 valves per FOV).
- C = common (1–5 valves per FOV).
- F = few (1 valve in every 10 FOVs).
- R = rare (<5 valves per transect).
- ? = questionable occurrence.
- rw = reworked occurrence.

The degree of siliceous microfossil fragmentation often mirrors dissolution, but the two factors are not always directly correlated. Diatoms with well-preserved fine structures can be highly fragmented. Dissolution is a wholly chemical process (Warnock and Scherer, 2015), but fragmentation can be dominantly or entirely due to mechanical processes such as compaction or subglacial processes (Scherer et al., 2004). Preservation of diatoms, therefore, was qualitatively assessed with regard to both the degree of dissolution and fragmentation. The degree of dissolution was qualitatively graded as follows:

- L = low (slight to no apparent dissolution [fine structures generally preserved]).
- M = moderate (moderate dissolution [fine structures may be lost]).
- H = high (severe effects of dissolution, including widened areolae, fusion of neighboring areolae, relatively abundant margins and cingula compared with valves, and notably higher proportions of heavily silicified forms).

The degree of fragmentation was graded as follows:

- L = low (>50% of identifiable diatoms are intact).
- M = moderate (>50% of diatom valves are broken, but most are identifiable).
- H = high (valves highly fragmented and very few complete valves present, hampering identification).

4.4. Palynology

4.4.1. Taxonomy and zonation scheme

Dinocyst taxonomy follows that presented in Williams et al. (2017), except for the subfamily *Wetzelielloideae*, for which we follow recommendations in Bijl et al. (2017). Diachroneity of dinocyst ranges is a commonly recognized issue (e.g., Williams et al., 2004). For dinocyst biostratigraphy, the DINOSTRAT database (Bijl, 2022) was used, which contains a comprehensive overview of regionally calibrated first and last occurrence datums of dinocysts for the Mesozoic–Cenozoic. We used version 2.0 of DINOSTRAT (**https://github.com/bijlpeter83/DINOSTRAT**), which was updated to GTS2020 (Gradstein et al., 2020). Dinocyst ranges from DINOSTRAT that were calibrated at nearby sites (the Southern Ocean or equatorial Atlantic) were preferentially used, where available. For the Cenomanian–Maastrichtian, we used predominantly biohorizon ages from Kerguelen Plateau (ODP Site 748; Mao and Mohr, 1992), Ivory Coast (ODP Site 959; Masure et al., 1998), Australia (Helby et al., 1987), and Norfolk, UK (Pearce, 2000; Pearce et al., 2020). For the interval around the K/Pg boundary, we used biohorizon ages of dinocysts from expanded successions such as those at El Kef, Tunisia (Brinkhuis et al., 1998), and New Zealand (Crouch et al., 2014). For the Paleocene, biohorizons from sections in New Zealand (Crouch et al., 2014), Tasmania (Bijl et al., 2013), and the North Sea (Powell, 1992) were used. Biohorizon ages are compiled in Table **T11**, along with the calibrations to the independent age constraints (in fraction from the base of the biostratigraphic zone, stage, or magnetochron they were calibrated to) and site and/or section at which they were calibrated (following the approach as outlined in Bijl, 2022).

For taxonomy of miospores, we relied on Atta-Peters and Salami (2004), Contreras et al. (2014), Helby et al. (1987), Masure et al. (1998), Morgan (1978), and references therein.

4.4.2. Methods for palynology study of sediments

Approximately 5–15 g of sediment from core catcher samples were processed for shipboard palynology analysis. However, time limited the ability to process all core catchers. Hence, a selection of core catcher samples was processed for palynology. The processing procedure depended on the lithologic characteristics of the sample. Two basic approaches were used: one involving disaggregation of material without the use of hydrofluoric acid (HF), and one involving digestion of siliciclastic material using HF. At the start of both methods, where presence of calcium carbonate was expected, an overload 30% HCl was added to decalcify the sample. The next step in the processing depended on the outcome of that first step:

- Samples that were sufficiently disaggregated in the decalcification procedure were subsequently sieved (see below for the sieving process).
- If success of disaggregation of samples (through HCl digestion) was a priori deemed unlikely to be successful or when the abundance of detrital material started to prevent adequate sieving of the samples, HF treatment was applied to subsequent samples. In the HF procedure, samples were digested with cold 48% HF to dissolve silicates, followed by 30% HCl to remove silicate gels. Centrifuging and decanting were carried out after each step.

The processing method applied to each sample was recorded in the results table as follows:

- HCl: removal of calcium carbonate.
- HF: digestion with HF.

4.4.3. Sieving, slide preparation, and microscopy

All samples were sieved through a 15 µm mesh to remove small amorphous organic matter. An ultrasonic bath was used to further disaggregate material left on the 15 µm sieve. Further concentration of palynofacies and removal of leftover detrital material was done using a swirling method, which takes advantage of the lower specific density of palynofacies compared to detrital material. All samples were mounted on glass microscope slides using glycerin jelly as the mounting medium. Species identification and data collection were carried out with a ZEISS AxioScope microscope using brightfield illumination at 400×, 630× (oil), and 1000× (oil) magnification. Photomicrography was conducted using a SPOT Flex 64 imaging system. All images were uploaded to the LIMS database.

4.4.4. Palynomorph abundance and preservation

Palynofacies were grouped into the following broad categories as follows:

- In situ marine organic-walled dinocysts.
- Reworked marine organic-walled dinocysts.
- Foraminiferal test linings.
- Prasinophytes.
- Acritarchs.
- Miospores (pollen and spores).

Table T11. Age estimates of dinocyst datums used during Expedition 392. Source: Bijl, 2022. **Download table in CSV format.**

Location of calibration	Datum	Source	Calibration	GTS2020 Age (Ma)
Southern North Sea	T *Filisphaera filifera*	Kuhlmann et al., 2006	0 in mag_C1n	0.8
ODP Site 1168	B *Stelladinium stellatum*	Brinkhuis et al., 2004a	0 in mag_C2r.1n	2.1
ODP Site 1168	B *Distatodinium biffii*	Brinkhuis et al., 2004a	0.5 in mag_C9n	26.9
IODP Site 1411	T *Enneadocysta pectiniformis*	Egger et al., 2016	0.5 in mag_C9n	26.9
ODP Site 1168	T *Phthanoperidinium comatum*	Brinkhuis et al., 2004a	0.5 in mag_C12n	30.8
IODP Site U1356A	B *Hystrichokolpoma bullatum*	Bijl et al., 2018	1 in mag_C12r	31.0
ODP Site 1172	T *Glaphyrocysta pastielsii*	Bijl et al., 2013	0.4 in mag_C24r	55.8
ODP Site 959	T *Thalassiphora delicata*	Awad and Oboh-Ikuenobe, 2016	0.5 in nan_c_CP8a	56.6
Angora Road, Tawanui	T *Eisenackia reticulata*	Crouch et al., 2014	1 in nan_n_NP6	59.0
ODP Site 1172	T *Palaeoperidinium pyrophorum*	Bijl et al., 2013	0.5 in mag_C26n	59.1
ODP Site 1172	B *Thalassiphora delicata*	Bijl et al., 2013	0.5 in mag_C26n	59.1
ODP Site 1172	B *Glaphyrocysta pastielsii*	Brinkhuis et al., 2004b	0.5 in mag_C26n	59.1
Disko Island	B *Glaphyrocysta divaricata*	Piasecki et al., 1992	0.5 in nan_n_NP6	59.2
ODP Site 959	B *Spiniferella cornuta*	Masure et al., 1998	0.8 in stage_Selandian	59.7
ODP Site 1172	T *Lejeunecysta rotunda*	Bijl et al., 2021	0.5 in mag_C26r	60.6
North Sea Compilation	T *Disphaerogena carposphaeropsis*	Powell, 1992	1 in plfor_B_P3a	61.5
ODP Site 1172	B *Lejeunecysta rotunda*	Bijl et al., 2021	0 in mag_C26r	61.9
Synthesis N Germany	T *Senoniasphaera inornata*	Köthe, 2012	0.8 in nan_n_NP3	63.5
Scotian Margin	B *Alisocysta margarita*	Williams et al., 1993	0.5 in stage_Danian	63.9
Mid-Waipara	T *Trithyrodinium evittii*	Crouch et al., 2014	0.5 in nan_n_NP3	63.9
El Kef	B *Cordosphaeridium fibrospinosum*	Brinkhuis et al., 1998	0.75 in plfor_B_P0	66.0
Mid-Waipara	B *Danea californica*	Willumsen, 2012	0 in plfor_A_P0	66.0
Mid-Waipara	B *Senoniasphaera inornata*	Willumsen, 2012	0 in plfor_A_P0	66.0
Mid-Waipara	B *Trithyrodinium evittii*	Willumsen, 2012	0 in plfor_A_P0	66.0
Scotian Margin	T *Triblastula utinensis*	Williams et al., 1993	0.85 in stage_Maastrichtian	67.0
ODP Site 1172	B *Eisenackia reticulata*	Brinkhuis et al., 2004b	0.5 in mag_C31n	68.8
Australia Synthesis	B *Manumiella druggii*	Helby et al., 1987	0.4 in stage_Maastrichtian	69.7
North Sea Compilation	T *Trithyrodinium suspectum*	Costa and Davey, 1992	1 in amm_b_Nostoceras hyatti	69.9
ODP Site 748	T *Odontochitina porifera*	Mao and Mohr, 1992	1 in nan_n_CC24	70.1
ODP Site 748	T *Impagidinium cristatum*	Mao and Mohr, 1992	0.8 in nan_n_CC24	70.6
ODP Site 748	T *Xenikoon australis*	Mohr and Mao, 1997	0.6 in nan_n_CC24	71.0
ODP Site 748	T *Leberidocysta chlamydata*	Mao and Mohr, 1992	0.5 in nan_n_CC24	71.2
ODP Site 748	T *Isabelidinium cretaceum*	Mohr and Mao, 1997	0.5 in nan_n_CC24	71.2
ODP Site 748	T *Isabelidinium cooksoniae*	Mohr and Mao, 1997	0.25 in nan_n_CC24	71.7
ODP Site 959	T *Oligosphaeridium pulcherrimum*	Masure et al., 1998	1 in stage_Campanian	72.2
ODP Site 748	T *Odontochitina cribropoda*	Mao and Mohr, 1992	1 in nan_n_CC23	72.2
ODP Site 748	T *Batiacasphaera reticulata*	Mohr and Mao, 1997	0.5 in nan_n_CC23	74.1
ODP Site 748	T *Odontochitina costata*	Mohr and Mao, 1997	0.5 in nan_n_CC23	74.1
ODP Site 748	T *Cyclonephelium compactum*	Mao and Mohr, 1992	0.4 in nan_n_CC23	74.4
Scotian Margin	B *Palaeoperidinium pyrophorum*	Williams et al., 1993	0.8 in stage_Campanian	74.5
ODP Site 748	B *Isabelidinium pellucidum*	Mohr and Mao, 1997	0.1 in nan_n_CC23	75.5
ODP Site 748	T *Xenascus ceratioides*	Mohr and Mao, 1997	0 in nan_n_CC23	75.9
ODP Site 748	B *Odontochitina porifera*	Mao and Mohr, 1992	0.2 in nan_n_CC22	76.6
Australia Synthesis	T *Nelsoniella aceras*	Helby et al., 1987	0.45 in stage_Campanian	78.5
ODP Site 748	B *Odontochitina cribropoda*	Mohr and Mao, 1997	0.9 in stage_Santonian	83.9
North Sea Compilation	T *Heterosphaeridium difficile*	Costa and Davey, 1992	1 in amm_b_Placenticeras polyopsis	83.9
East Kent	T *Circulodinium distinctum*	Prince et al., 2008	0.92 in amm_b_Placenticeras polyopsis	84.0
Australia Synthesis	T *Balteocysta perforata*	Helby et al., 1987	0.25 in stage_Santonian	85.2
Australia Synthesis	T *Conosphaeridium striatoconus*	Helby et al., 1987	0.25 in stage_Santonian	85.2
ODP Site 959	B *Oligosphaeridium pulcherrimum*	Masure et al., 1998	0 in stage_Santonian	85.7
ODP Site 748	B *Impagidinium cristatum*	Mohr and Mao, 1997	0.5 in nan_e_Broinsonia parca expansa	85.9
East Kent	B *Circulodinium distinctum*	Prince et al., 2008	0.2 in amm_b_Gauthiericeras margae	88.0
East Kent	B *Cyclonephelium filoreticulatum*	Prince et al., 2008	0.4 in amm_b_Peroniceras tridorsatum	88.9
Australia Synthesis	B *Conosphaeridium striatoconus*	Helby et al., 1987	0.67 in stage_Turonian	90.9
North Sea Compilation	B *Trithyrodinium suspectum*	Costa and Davey, 1992	0.38 in amm_b_Metoicoceras geslinianum	94.4

- Black phytoclasts.
- Brown phytoclasts.
- Fungal spores.
- Amorphous organic matter.

For semiquantitative estimates of the abundance of these palynofacies groups, the following scale was used:

- D = dominant (>90% of palynomorphs).
- A = abundant (>50%–90% of palynomorphs).
- C = common (>10%–50% of palynomorphs).
- F = few (1%–10% of palynomorphs).
- R = rare (<1% of palynomorphs).
- B = barren (not present).

Dinocysts in each sample were identified to the genus or species level, where possible. For biostratigraphic and paleoenvironmental purposes, shipboard analysis of palynomorphs focused primarily on determining the presence of age-diagnostic dinocyst taxa and characterizing the palynological assemblage in terms of paleoenvironment.

The following qualitative indication of their occurrence is used to present abundance of individual species:

- D = dominant (>90% of palynomorphs).
- A = abundant (>50%–90% of palynomorphs).
- C = common (>10%–50% of palynomorphs).
- F = few (1%–10% of palynomorphs).
- R = rare (<1% of palynomorphs).
- ? = questionable assignment.
- rw = reworked.

Miospores identified during these counts followed the same abundance scheme as the dinocysts, and this provided a preliminary assessment of the yield. Where time constraints allowed, miospores were identified to genus and species level.

Palynomorph preservation was qualitatively classified as follows:

- G = good (little or no evidence of degradation or oxidation).
- M = moderate (some evidence of degradation or oxidation).
- P = poor (major degradation or oxidation has occurred).

4.4.5. Palynology-based paleoenvironmental analysis

Three indicators were used to infer aspects of the depositional environment. The palynofacies composition provides a general characterization of the composition of organic matter (terrestrial or marine), the level of oxidation of the sediment (Keil et al., 1994), and the level of maturity. Miospore assemblages provide qualitative information on hinterland climate conditions, mainly precipitation and seasonality. The abundance of insect-pollinated versus wind-pollinated miospores provides information on proximity to shore and runoff intensity (e.g., Sánchez Goñi et al., 2018).

The use of dinocysts as paleoenvironmental indicators derives from two broad lines of evidence:

- Information on their present-day global distribution, including in southern high latitudes (Esper and Zonneveld, 2007; Prebble et al., 2013; Zonneveld et al., 2013). These studies showed dinoflagellate distribution in the modern ocean is strongly influenced by sea-surface temperature (SST), sea ice, surface productivity, and salinity. Other aquatic palynomorphs, in particular acritarchs and prasinophytes, were used to infer information on riverine input/water stratification. Miospore assemblages can provide quantitative and semiquantitative information about terrestrial conditions at the time the source vegetation grew (e.g., Contreras et al., 2014).
- A second line involves empirical information on the paleoecological affinity of now-extinct dinocyst taxa (e.g., Sluijs et al., 2005; Frieling and Sluijs, 2018) through comparison with other

indicators of paleoenvironmental conditions. This resulted in qualitative, and even steps toward quantitative, ecological affinities of so-called dinocyst ecogroups. Index species were identified for sea-surface stratification, upwelling, freshwater input, salinity, SST, nutrients, and sea level dynamics (Sluijs et al., 2005; Frieling and Sluijs, 2018, and references therein). Although these paleoecological affinities were mostly identified for Cenozoic taxa, many of these taxa have either stratigraphic ranges extending into the Late Cretaceous (Bijl, 2022) or have closely affiliated taxa with likely similar affinities as their Cenozoic ancestors (Fensome et al., 1993).

Additional information about the depositional environment was derived from reworked palynomorphs (dinocysts and miospores) as in Bijl et al. (2018).

5. Paleomagnetism

Onboard paleomagnetic investigations during Expedition 392 focused mainly on determining the orientation of the natural remanent magnetization (NRM) vectors of core samples. This was done by performing quasicontinuous measurements on the archive-half sections, integrated with measurements on discrete samples from the working-half sections. Rock magnetic experiments were also performed to further characterize the magnetic properties of the core material.

5.1. Core orientation

Core orientation information was obtained during collection for APC cores only. APC and RCB cores were collected using a nonmagnetic core barrel. APC cores were oriented using the FlexIT or Icefield MI-5 core orientation tool. HLAPC, XCB, and RCB cores were not oriented. All results of oriented cores were reported in geographic coordinates derived using FlexIT/Icefield MI-5 measurements and local International Geomagnetic Reference Field (IGRF13) magnetic declination.

5.1.1. Continuous measurements

Remanence measurements of archive-half sections were performed using a 2G Enterprises superconducting rock magnetometer (SRM) equipped with direct-current superconducting quantum interference devices (DC-SQUIDs) and an in-line automated three-axes alternating field (AF) demagnetizer (maximum AF step = 80 mT). The coordinate systems used for archive halves, SRM, and AF demagnetizing coils are illustrated in Figure **F13A**. The background noise level (i.e., empty holder) of the shipboard SRM during Expedition 392 on average is x-axis = ~1.5×10^{-8} Am^2, y-axis = ~5.0×10^{-10} Am^2, and z-axis = ~5.0×10^{-9} Am^2. Occasionally, the background noise level of the SRM increases to x-axis = ~3.0×10^{-8} Am^2, y-axis = ~5.0×10^{-9} Am^2, and z-axis = ~1.0×10^{-8} Am^2. NRM was measured at 2.5 or 5 cm intervals, and measurements were repeated after AF demagnetization with a variation of three to four of the following steps: 5, 10, 15, and 20 mT. Intervals with clearly visible drilling-related disturbance were not measured. To avoid possible magnetic contamination, the sample track was cleaned a minimum of once per work shift (~12 h). The magnetization of the sample tray was also measured once per work shift, and the obtained value (holder) was subtracted from archive-half measurements.

Measurements of archive halves were conducted using the onboard Integrated Measurement System (IMS) (version 10.2) software. The measurement interval was 2.5 to 5 cm, and measurement speed was 1 Hz. The pick-up coil response functions of the DC-SQUID sensors have a full width of 7.2–9.1 cm at half height (Acton et al., 2017). Therefore, data collected within ~4.5 cm of piece boundaries (or voids) are significantly affected by edge effects. Consequently, all data points within 5 cm of piece boundaries (as documented in the curatorial record) were filtered out prior to further processing. Edge effects may also occur in a continuous core piece if substantial heterogeneity (in intensity or direction) is present in the piece. It is more difficult to filter out such artifacts, but calculating the average direction (using Fisher statistics; Fisher, 1953) for each core piece could provide a means of identifying these problems (Koppers et al., 2013).

5.1.2. Discrete measurements

Normally, one to two discrete samples per core were collected from undeformed, finer grained intervals, avoiding intervals clearly affected by drilling-induced disturbance. Discrete sample analysis helps to monitor the behavior of core samples during AF and thermal demagnetization experiments, determine the AF step necessary to remove the magnetic overprint in the archive-half section, and can additionally help characterize magnetic mineralogy. For soft-sediment intervals, discrete samples were collected from working halves using plastic Natsuhara-Giken sampling cubes (volume = 7 cm^3). Cubes were pushed into the working halves by hand with the up arrow (–*z*-axis) on the cube pointing toward the top of the core section (Figure **F13B**). For more indurated intervals, an extruder was pushed into the sediment and the cut material was then placed in a plastic box. For very hard lithified sediment and volcanic rock intervals, 8 cm^3 cubic samples (2 cm × 2 cm × 2 cm) were cut using a trim saw. The orientation of the cubes follows the right-hand rule (Figure **F13B**). For hard rock core samples, at least one oriented cube was analyzed per core.

All discrete samples were measured for volume-normalized bulk susceptibility (χ), and a select few were measured for anisotropy of magnetic susceptibility (AMS) with an AGICO Kappabridge (model KLY 4). The Kappabridge measures AMS by rotating the sample along three axes, stacking the data, and calculating the best-fit second-order tensor by using the AMSSpin freeware of Gee et al. (2008). Tensor elements were converted to eigenparameters (eigenvectors V_1, V_2, and V_3 with corresponding eigenvalues τ1, τ2, and τ3, where τ1 = maximum value and τ3 = minimum value) (Tauxe, 2010). The average AMS tensor of each set of samples was estimated by using the bootstrap approach of Constable and Tauxe (1990), and the anisotropy degree (*P′*) and shape parameter (T) have been calculated as follows (Jelinek, 1981):

$$P' = exp\sqrt{2\sum_{i=1}^{3}(\eta_i - \underline{\eta})^2}$$

and

$$T = \frac{2\eta_2 - \eta_1 - \eta_3}{\eta_1 - \eta_3},$$

where η_i is the natural logarithm of the normalized eigenvalue k_i axis and

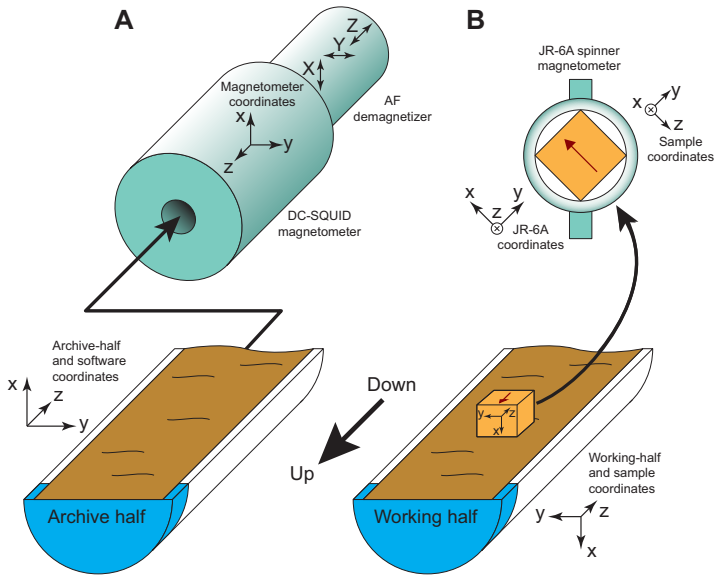

Figure F13. Coordinate systems used for (A) pass-through SRM measurements on archive halves, and (B) JR-6A spinner magnetometer measurements on discrete working-half samples.

$$\underline{\eta} = \frac{1}{3}\sum_{i=1}^{3}\eta_i .$$

A value of $P' = 1.0$ indicates the absence of magnetic fabric, and T > 0 (T < 0) indicates an oblate (prolate) ellipsoid. Normal sedimentary AMS fabrics are oblate with vertical axes corresponding to minimum susceptibility. Sediment deformation or other disturbances (e.g., bottom current) generally produce different AMS fabrics.

Following susceptibility measurements, AF demagnetization of discrete samples was performed using an ASC Scientific AF demagnetizer (model DTECH D-2000). After initial NRM measurement, discrete samples were progressively demagnetized along three axes in peak AF steps of 5, 10, 15, 20, 25, 30, 40, 50, and 70 mT. For some samples, additional lower steps (e.g., 2, 4, 6, or 8 mT) or higher AF steps of 90, 120, or 150 mT were used. A select few hard rock samples were also stepwise thermally demagnetized using an ASC Scientific Model TD-48 SC thermal specimen demagnetizer to temperatures up to 600°C. The remanence before and after demagnetization for discrete samples was measured on an AGICO JR-6A dual-speed spinner magnetometer (Figure **F13B**). The background noise level of the shipboard JR-6A was mostly ~1.0×10^{-5} A/m (volume = 8 cm^3) during Expedition 392. Data were transformed from the JR-6A instrument coordinate system to the core coordinate system. Principal component analysis (PCA) of characteristic remanent magnetization (ChRM) vectors (Kirschvink, 1980) was carried out using the PuffinPlot software package (Lurcock and Wilson, 2012). For best-fit lines with maximum angular deviation of >20° or for samples where the data clustered on vector endpoint plots and stopped trending, a Fisher (1953) mean was determined for at least three consecutive demagnetization steps that remained in the same direction.

After demagnetization experiments were completed on cube samples, isothermal remanent magnetization (IRM) acquisition experiments were performed at 100, 1200, and a backfield of 300 mT (denoted as -300) using an ASC IM10 impulse magnetizer. IRM acquisition remanence measurements are indicative of the magnetic mineralogy, which depends on the detrital magnetic mineral supply and/or diagenetic dissolution and neoformation of ferrimagnetic minerals.

Based on these remanence parameters, the saturation IRM (SIRM) was approximated by

$$\text{SIRM} = \text{IRM 1200 mT},$$

and the hard IRM (HIRM) was approximated by

$$\text{HIRM} = 0.5 \times (\text{SIRM} - \text{IRM\_-300 mT}),$$

where IRM_-300 is indicative of a backfield 300 mT step, and the *S*-ratio was calculated by

$$S = 0.5 \times (1 - \text{IRM\_-300 mT/SIRM}).$$

Note that the IRM_-300 measurement was assigned a negative value in instances when the application of the 300 mT backfield resulted in a polarity change from the SIRM step (e.g., inclination values flipped from 90° to –90°).

HIRM is a measure of the contribution of high-coercivity minerals (e.g., hematite) to the signal. The *S*-ratio is a measure of the relative amounts of low coercivity (soft) versus high coercivity (hard) and provides an estimate of the relative importance of ferrimagnetic minerals (e.g., magnetite) versus antiferromagnetic minerals (e.g., hematite). *S*-ratios close to 1 indicate a mineralogy dominated by low-coercivity minerals and values <1 indicate a mineralogy affected by high-coercivity minerals. For IRM experiments, magnetic intensities were measured using a JR-6A spinner magnetometer.

5.1.3. Magnetostratigraphy

Chron assignment was performed for each site by correlating observed polarity sequences to the current geomagnetic polarity timescale (GPTS) (Ogg, 2020) with the aid of biostratigraphic observations. For this expedition, we used the GPTS from the GTS2020 (Gradstein et al., 2020) (Table **T12**). At the latitude of the sites in this expedition (~40°S), polarity can be determined using the

sign of paleomagnetic inclination alone. In general, reversals were marked at the halfway point between the lower (upper) reversed polarity sample and upper (lower) normal polarity sample.

6. Stratigraphic correlation

Sedimentary successions cannot be continuously cored at a single borehole even when core recovery in a hole exceeds 100% (e.g., Ruddiman et al., 1987; Hagelberg et al., 1995; Acton et al., 2002). Core recovery exceeding 100% is common with APC and XCB drilling because of core expansion at the sea surface (red bands indicate added length in Figure **F14**). Gaps and disturbances occur between successive cores, caused by ship heave, drilling, and tides. To recover a complete sediment succession, adjacent holes offset by tens of meters laterally and several meters vertically must be cored and then correlated.

The main objective of stratigraphic correlation is to define a continuous lithologic record combining adjacent drilled holes at a given site. The composite record of multiple holes is called the "splice." It represents the most complete and undisturbed sedimentary sequence recovered at each

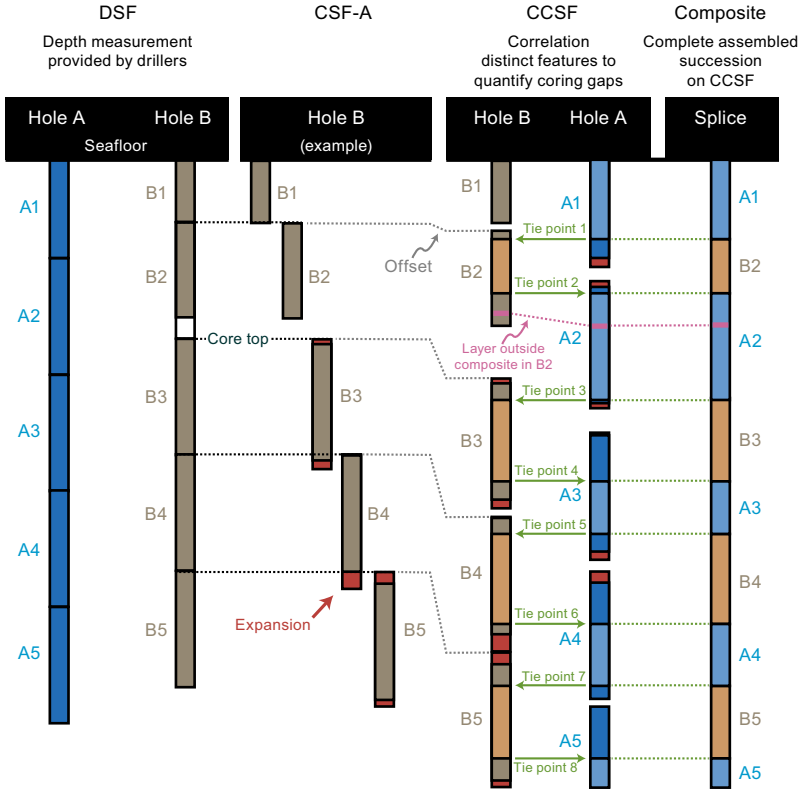

Figure F14. Interrelationship between cored material and the depth scales used during Expedition 392. In this example scenario, five cores were recovered from Hole A. The starting depth for coring Hole B was offset vertically by several meters to cover gaps in the record of Hole A. Five cores were recovered from Hole B, of which Core B2 had less than full recovery and Cores B3, B4, and B5 had more than 100% recovery because of expansion of core material, resulting in increased length (red segments). The CSF-A scale (example Hole B) is established by adding the curated core length (red and brown intervals) to the depth of each core top determined by the DSF measurement. If recovery is >100%, plotting recovery on the CSF-A scale will result in overlap between cores of the same hole. The CCSF scale corrects for this and other inadequacies of the CSF-A scale. It is based on locating features common to cores in multiple holes at a given site and is constructed by working from the top of the site downward to select tie points (green dashed lines) that correlate features in one hole to those in another. Because of core expansion, Holes A and B on the CCSF scale are longer than they are on the CSF-A scale. The splice on the CCSF scale at the far right is constructed by combining selected intervals between tie points so that coring gaps and disturbed sections are excluded. This process ideally results in a complete stratigraphic sequence. The procedure assumes identical sediment thickness between tie points joining two holes. However, because of differential squeezing and stretching of each core during the coring process and lateral variations in sedimentation, features cored in parallel will not align perfectly, as illustrated by the pink dashed lines joining the pink horizon in Cores A2 and B2.

site. Sampling for scientific analyses will primarily be done along the splice. Therefore, the quality of the composite record is critical for several key scientific objectives of Expedition 392. Intervals not included in the splice can be sampled; however, due to differential degrees of core expansion, compression, or local sedimentological differences among holes, small variations in the reported depth of correlative features in adjacent holes will occur.

To ensure complete recovery if two or more holes were drilled, near-real-time monitoring of the parallel hole was done by correlating features in newly recovered cores to features in previously drilled cores from the first hole. To allow for near-real-time correlation, thermally unequilibrated cores from the parallel holes were measured immediately after recovery and processing on the catwalk on the "fast-track" Special Task Multisensor Logger (STMSL) (see **Physical properties**). During Expedition 392, MS and NGR were generally the most useful information to guide drilling decisions, enabling identification of shared features among holes. If needed, the stratigraphic correlators advised the drillers when adjustments should be made in coring to ensure that core gaps in previously drilled holes were covered. After completing coring at a given site, stratigraphic correlation among holes was refined using all available physical property data, biostratigraphic data, and digital images of the split core halves to identify intervals in each hole with the best recovery that could be joined to assemble a complete composite record.

6.1. Composite record procedure

Using multiple data types, stratigraphic correlators identify tie points in each core of each hole that place it in a stratigraphic position most in agreement with cores in neighboring holes. The starting point is the longest first core that captures the mudline from among all holes at a site, which becomes the anchor in the composite record. In Figure **F14**, Core A1 captured the mudline and is selected as the anchor for the composite record. From this anchor, multiple data types are used to identify common features that can be correlated among holes downsection. For each core, a depth offset that best aligns the physical property variations to the equivalent cores in adjacent holes is added to the CSF-A depth scale, generally resulting in a cumulative depth offset in sequence down the holes (gray dashed lines indicate offsets in Figure **F14**). Depth offsets are often chosen to optimize correlation of specific features that later define splice levels in cores from adjacent holes. Not all features in a single core may line up with a parallel core (pink intervals and dashed line in Figure **F14**) because of differential disturbance or local variation in sedimentation.

When all cores are correlated, a composite record can be defined, ideally along the tie points already identified for the correlation (rightmost panel of Figure **F14**). The splice starts with the core that captures the mudline or the highest core in the interval of overlap between holes if it is some distance below the seafloor. Splicing continues downward by selection of the best recovered intervals across holes that together capture the most continuous and complete record of the drilled stratigraphy. The Hostile Environment Natural Gamma Ray Sonde (HNGS) downhole log measurements of total spectral gamma ray (HSGR) were consulted to establish the stratigraphic position of core data in case of incomplete core recovery.

Construction of a splice using parallel drilled cores from different holes was only possible for Site U1579. It was based on the stratigraphic correlation of data from the WRMSL, SHMSL, NGRL, and SHIL. NGRL data were collected at 10 cm intervals, WRMSL and SHMSL data were collected at 2.5 cm intervals (see **Physical properties**), and the SHIL line scan interval is 20 lines/mm (50 μm) (see **Lithostratigraphy**). Raw data were imported into Correlator software (v4.0) and culled as necessary to avoid incorporating anomalous data influenced by edge effects at section boundaries and by coring disturbance. Additionally, correlators employed the Code for Ocean Drilling Data (CODD), an Igor Pro–based system designed to integrate ocean drilling data of all types with depth-scaled core images (**https://www.codd-home.net**).

Constructing a splice entails a progression through a series of different depth scales from reported drilling depth to final composite depth (Figure **F14**). The naming conventions used for the depth scales follow IODP convention (**http://www.iodp.org/policies-and-guidelines**) and are described below.

6.2. Core depth below seafloor scale

The process of building a composite section begins by assigning a depth to the top of each core initially using the DSF depth scale. The DSF scale is a drill string measurement based on the length of drill string from the seafloor to the cored top of each core. It is calculated by subtracting the length of the drill string from the rig floor to the top of the cored interval from the length of the drill string between the rig floor and the mudline (the estimated level of the seafloor). Sources of error in the DSF depth scale are numerous and include pipe and BHA stretch and compression, tidal variations, wind-induced differences in the height of the sea surface, currents and wind affecting the bend of the drill string, and uncompensated heave. The influence of tides on DSF measurements can be significant (Hagelberg et al., 1995), and the prediction of tides is generally useful for guiding drilling to avoid initial gap alignment (Shipboard Scientific Party, 2003b). Because of the small tidal range of ±50 cm in the region of the sites, no adjustment was needed during Expedition 392.

The CSF-A depth scale is used to characterize the depth for a given position in any core. The CSF-A depth scale combines the DSF core-top depth with the curated length of the core after retrieval and allows overlap at core boundaries. The CSF-A scale is equivalent to the mbsf scale used during the DSDP, ODP, and Integrated Ocean Drilling Program. CSF-A values are specific to each hole, and the CSF-A scale is the depth scale used for most primary observations, including information summarized on the VCDs and presented in the site chapters. Minor inaccuracies in the CSF-A scale are related to both drilling effects and core expansion effects; thus, the CSF-A scale permits stratigraphically impossible overlaps between successive cores.

To compensate for expansion, the CSF-B depth scale is calculated for all cores as well. When recovery is ≤100%, the CSF-A and CSF-B scales have the same value. When recovery is >100%, linear interpolation is applied to compress the recovered interval into the length drilled, eliminating apparent overlaps. Factors that lead to >100% recovery include elastic, thermal, and/or gas-induced core expansion; flow-in and/or recovery of downhole contaminants; and gaps due to rotation and misalignment of breaks during sectioning. CSF-B values are available for all holes drilled during Expedition 392 but were not used in any of the reports.

6.3. Core composite depth below seafloor scale

The construction of a composite depth scale for a given site starts from the mudline or from the highest core in an interval of overlap. Compositing involves identification of coeval, laterally continuous features in parallel drilled holes, which may occur at different depths on the CSF-A scale for each hole. Once correlative features are identified, the depths of individual cores are offset relative to the CSF-A depth scale by a single value for each core in that hole such that the features are optimally aligned. Offsets for every core in every hole were tabulated in an affine table from each site with multiple stratigraphically overlapping holes. The resulting new depths for all the shifted cores are on the CCSF scale, which gives the distance from seafloor to target (e.g., core, sample) within recovered cores using a scale of adjusted depths constructed to resolve depth inconsistencies and gaps in the core recovery. The CCSF scale is equivalent to the meters composite depth (mcd) scale used during ODP and Integrated Ocean Drilling Program expeditions.

Compositing proceeds sequentially downcore through the establishment of specific tie points among the various holes. Because of coring-induced stretching and squeezing and stratigraphic differences between holes, the CCSF scale does not result in precise alignment of all coeval features among holes. Care should be taken when comparing results from samples collected from within the splice to those for the same CCSF interval in intervals not included in the splice.

Although all care is taken to avoid overlapping core gaps among holes, in practice at least some coring gaps exist at most sites. Downhole logging data can be used to estimate the length of the gap, maintaining an observational connection to the anchor core. When there is an aligned core gap across all holes at a site without suitable downhole data, cores below the gap are no longer tied to the anchor core. These cores can still be tied to one another, but the correlated sections are considered to be floating on the CCSF scale.

Choosing a CCSF depth for floating sections is subjective. During Expedition 392, one of two methods was used to tie floating sections into the splice as noted in the affine table. When a core was APPENDED, the core being appended used the inherited absolute offset of the core above the coring gap. When a core was SET, the stratigraphic correlator set a user-defined offset that resulted in the best qualitative alignment. In cases with large aligned core gaps within a splice, the CCSF scale for the uppermost core below the gap was assigned the same value as the CSF-A offset of that core. Alternative methods for defining a SET offset are available but were not used during Expedition 392.

During the process of constructing the composite section, a CCSF depth may become expanded compared to that of the CSF-A depth for equivalent horizons. This expansion of the depth scale may be an artifact of the selection of tie points or can be related to physical processes, including decompression of the sediment as it is brought to atmospheric pressure, pore space gases coming out of solution, warming, stretching that occurs as part of the coring process, and recovery of additional material, likely from borehole wall sediment that fell downhole and entered the core barrel (e.g., Hagelberg et al., 1995; Acton et al., 2002). Expansion of depth scales during Expedition 392 was limited, and offsets did not generally exceed the depth of the bottom of the interval drilled.

6.4. The splice

Once the CCSF scale is developed and the between-core gaps identified, a complete stratigraphic section (splice) is constructed by combining selected intervals between the previously established tie points. In case of core gaps aligned across all holes, any spliced sections below the gap are designated as floating splice sections and plotted against CCSF as described above.

6.5. Measurements and methods for correlation

Given that few long sections of overlap were cored at any site and the drilling technique used often differed between holes during Expedition 392, we adjusted our approach to correlation based on the specifics of the situation. Observations of features in the recovered core as seen through the core liner, comparison of DSF/CSF-A measurements between holes, and MS measurements acquired as soon as possible after core retrieval using the STMSL track were most useful for guiding drilling decisions in near real time. The success rate of these decisions in bridging coring gaps and areas of disturbed sediment was high. The initial correlation between holes used for guiding drilling was refined as additional information became available from subsequent analyses, including biostratigraphic and magnetostratigraphic information, higher resolution physical property records measured on the WRMSL, sedimentological observations, photos, and color data. In addition, comparison between core measurements and downhole logs were used to test and refine correlations. NGR arguably gave the most consistently useful means of correlation between holes beyond aligning drilling depths. In specific instances, however, other data (e.g., digitized color reflectance data [both RGB and L*, a*, b* measurements], MS, gamma ray attenuation [GRA] bulk density, lithologic observations, and paleomagnetic data) were all important. These data have different resolutions, and details on instrument calibrations, settings, and measurement intervals for Expedition 392 are given in **Physical properties**.

Compositing and splicing were accomplished using Correlator software (v4.0). The software generated standard affine tables (listings of the vertical offset, in meters, added to each core to generate the CCSF scale) and splice interval tables (listings of the specific core intervals used to construct the splice). These tables were uploaded into the LIMS database, which then linked the appropriate depth scale to any associated data set.

7. Chronostratigraphy

Age models for the sedimentary sequences recovered during Expedition 392 were constructed using biostratigraphic age constraints, including tops, bases, assemblages, evolutionary turnovers (see **Micropaleontology**) and, where possible, magnetostratigraphy (see **Paleomagnetism**). We use the GTS2020 of Gradstein et al. (2020) for all ages of biostratigraphic datums (Tables **T8**, **T9**,

T10, **T11**) and paleomagnetic chrons (Table **T12**). Age-depth tie points from bio- and magnetostratigraphy are combined into one age-depth model for each of the four sites drilled during Expedition 392. We place biohorizons by convention at the midpoint between constraining samples and magnetic polarity reversals between measurement points with clear opposite polarity. As a result, bio- and magnetostratigraphic tie points have depth uncertainty dictated by the spacing of samples. Age uncertainty is plotted when given in the GTS2020 or when ages are derived from the overlapping stratigraphic ranges of several age diagnostic species in one sample.

The age-depth models were plotted using R, a free software environment for statistical computing (R Core Team, 2018), with tidyverse (Wickham et al., 2019) packages. Average sedimentation rates were interpreted by running a locally weighted smooth fit (locally estimated scatterplot smoothing [LOESS]) through the tie points, with greater weighting of the magnetostratigraphic age constraints. This smoothing was modified where hiatuses are inferred. Where signs of rhythmicity in sedimentary banding patterns or physical property data were observed, sedimentation rates were estimated based on a preliminary interpretation of the potential orbital driver and compared to the biostratigraphic and magnetostratigraphic framework.

Table T12. The GPTS used during Expedition 392 (Ogg, 2020). **Download table in CSV format.**

Chron	Polarity chron	Base age (Ma)
C1	C1n	0.773
	C1r.1r	0.990
	C1r.1n	1.070
	C1r.2r	1.180
	C1r.2n	1.215
	C1r.3r	1.775
C2	C2n	1.934
	C2r.1r	2.116
	C2r.1n	2.140
	C2r.2r	2.595
C2A	C2An.1n	3.032
	C2An.1r	3.116
	C2An.2n	3.207
	C2An.2r	3.330
	C2An.3n	3.596
	C2Ar	4.187
C3	C3n.1n	4.300
	C3n.1r	4.493
	C3n.2n	4.631
	C3n.2r	4.799
	C3n.3n	4.896
	C3n.3r	4.997
	C3n.4n	5.235
	C3r	6.023
C3A	C3An.1n	6.272
	C3An.1r	6.386
	C3An.2n	6.727
	C3Ar	7.104
C3B	C3Bn	7.214
	C3Br.1r	7.262
	C3Br.1n	7.305
	C3Br.2r	7.456
	C3Br.2n	7.499
	C3Br.3r	7.537
C4	C4n.1n	7.650
	C4n.1r	7.701
	C4n.2n	8.125
	C4r.1r	8.257
	C4r.1n	8.300
	C4r.2r	8.771
C4A	C4An	9.105
	C4Ar.1r	9.311
	C4Ar.1n	9.426
	C4Ar.2r	9.647
	C4Ar.2n	9.721
	C4Ar.3r	9.786
C5	C5n.1n	9.937
	C5n.1r	9.984
	C5n.2n	11.056
	C5r.1r	11.146
	C5r.1n	11.188
	C5r.2r	11.592
	C5r.2n	11.657
	C5r.3r	12.049
C5A	C5An.1n	12.174
	C5An.1r	12.272
	C5An.2n	12.474
	C5Ar.1r	12.735
	C5Ar.1n	12.770
	C5Ar.2r	12.829
	C5Ar.2n	12.887
	C5Ar.3r	13.032
C5AA	C5AAn	13.183
	C5AAr	13.363
C5AB	C5ABn	13.608
	C5ABr	13.739
C5AC	C5ACn	14.070
	C5ACr	14.163
C5AD	C5ADn	14.609
	C5ADr	14.775
C5B	C5Bn.1n	14.870
	C5Bn.1r	15.032
	C5Bn.2n	15.160
	C5Br	15.974
C5C	C5Cn.1n	16.268
	C5Cn.1r	16.303
	C5Cn.2n	16.472
	C5Cn.2r	16.543
	C5Cn.3n	16.721
	C5Cr	17.235
C5D	C5Dn	17.533
	C5Dr.1r	17.717
	C5Dr.1n	17.740
	C5Dr.2r	18.007
C5E	C5En	18.497
	C5Er	18.636
C6	C6n	19.535
	C6r	19.979
C6A	C6An.1n	20.182
	C6An.1r	20.448
	C6An.2n	20.765
	C6Ar	21.204
C6AA	C6AAn	21.441
	C6AAr.1r	21.519
	C6AAr.1n	21.691
	C6AAr.2r	21.13
	C6AAr.2n	21.722
	C6AAr.3r	21.806
C6B	C6Bn.1n	21.985
	C6Bn.1r	22.042
	C6Bn.2n	22.342
	C6Br	22.621
C6C	C6Cn.1n	22.792
	C6Cn.1r	22.973
	C6Cn.2n	23.040
	C6Cn.2r	23.212
	C6Cn.3n	23.318
	C6Cr	24.025
C7	C7n.1n	24.061
	C7n.1r	24.124
	C7n.2n	24.459
	C7r	24.654
C7A	C7An	24.766
	C7Ar	25.099
C8	C8n.1n	25.264
	C8n.1r	25.304
	C8n.2n	25.987
	C8r	26.420
C9	C9n	27.439
	C9r	27.859
C10	C10n.1n	28.087
	C10n.1r	28.141
	C10n.2n	28.278
	C10r	29.183
C11	C11n.1n	29.477
	C11n.1r	29.527
	C11n.2n	29.970
	C11r	30.591
C12	C12n	30.977
	C12r	33.214
C13	C13n	33.726
	C13r	35.102
C15	C15n	35.336
	C15r	35.580
C16	C16n.1n	35.718
	C16n.1r	35.774
	C16n.2n	36.351
	C16r	36.573
C17	C17n.1n	37.385
	C17n.1r	37.530
	C17n.2n	37.781
	C17n.2r	37.858
	C17n.3n	38.081
	C17r	38.398
C18	C18n.1n	39.582
	C18n.1r	39.666
	C18n.2n	40.073
	C18r	41.030
C19	C19n	41.180
	C19r	42.196
C20	C20n	43.450
	C20r	46.235
C21	C21n	47.760
	C21r	48.878
C22	C22n	49.666
	C22r	50.767
C23	C23n.1n	50.996
	C23n.1r	51.047
	C23n.2n	51.724
	C23r	52.540
C24	C24n.1n	52.930
	C24n.1r	53.020
	C24n.2n	53.120
	C24n.2r	53.250
	C24n.3n	53.900
	C24r	57.101
C25	C25n	57.656
	C25r	58.959
C26	C26n	59.237
	C26r	62.278
C27	C27n	62.530
	C27r	63.537
C28	C28n	64.645
	C28r	64.862
C29	C29n	65.700
	C29r	66.380
C30	C30n	68.178
	C30r	68.351
C31	C31n	69.271
	C31r	71.451
C32	C32n.1n	71.691
	C32n.1r	71.851
	C32n.2n	73.651
	C32r.1r	73.951
	C32r.1n	74.051
	C32r.2r	74.201
C33	C33n	79.900
	C33r	83.650
C34	C34n	120.964

8. Geochemistry

The geochemistry program for Expedition 392 combined headspace hydrocarbon analyses, IW analyses, inorganic bulk geochemistry of sediments and hard rocks, and organic sediment geochemistry of sediments. Sediment geochemistry included total inorganic carbon (TIC), total carbon (TC), calculated total organic carbon (TOC), total nitrogen (TN), and on selected samples, total sulfur (TS) and bulk organic matter source and maturity analyses.

These analyses closely followed shipboard safety and pollution prevention requirements. The primary goal of these analyses was to determine the diagenetic regime by IW analysis and provide bulk sediment/hard rock geochemistry indicators for shipboard interpretation, providing a basis for shore-based sampling.

8.1. Whole-round samples for interstitial water sampling

Routine IW was extracted from 5–10 cm long whole-round sediment sections that were cut and capped immediately after core was curated into sections on the catwalk. In the upper 30 m of the sedimentary sequence, samples were taken at a resolution of approximately three samples per 10 m. Below the upper 30 m, one sample per core was typically taken from the bottom of Section 1 or from a section that was most optimal for pore fluid extraction upon visual inspection. However, the sampling resolution varied at each site due to core length and recovery. Samples from more than one hole were treated as constituting a single depth profile using the CSF-A depth scale as the depth reference, if possible. No acetone was used to seal the end caps of the cut cores until after all whole-round samples were removed from the catwalk.

In the laboratory, whole-round sediment samples were removed from the core liner under a nitrogen atmosphere, and the outer outside surfaces (~0.5 cm) of the sediment samples were carefully scraped off with spatulas to minimize potential contamination by drilling fluids. Each scraped whole-round sediment sample was placed into a Manheim titanium squeezer and compressed at ambient temperature with a Carver hydraulic press (Manheim, 1966). IW samples discharged from the squeezer were passed through 0.45 µm polyethersulfone membrane filters, collected in acid-cleaned plastic syringes, and stored in plastic or glass sample bottles for shipboard or shore-based analyses.

Samples saved for shore-based analyses were split into four separate aliquots for oxygen isotopes, carbon isotopes, Li and K isotopes, and rare earth elements (REE), trace metals, and Sr isotopes.

Sample allocation was determined based on the obtained pore fluid volume and analytical priorities. Data produced using the Agilent 5110 inductively coupled plasma–optical emission spectrometer (ICP-OES) was collected in atomic emission spectroscopy mode and is referred to as ICP-AES in the LIMS database. In this volume, ICP-AES is used to refer to these data. Aliquots for shipboard analysis using ICP-AES were acidified by adding ~10 µL of trace metal–grade concentrated HNO_3 and placed in 2 mL cryovials. Aliquots for titration and ion chromatography analyses were put in 10 mL glass vials.

After IW extraction was complete, a sample was taken from the sediment squeeze cake for onboard bulk parameter analyses and the remainder was divided and kept for various shore-based analyses by the shipboard science party. The remainder was returned to the repository.

8.2. Shipboard analysis

IW samples were analyzed on board the ship following protocols as described in Gieskes et al. (1991), Murray et al. (2000), and the IODP user manuals for shipboard instrumentation.

8.2.1. Salinity, alkalinity, and pH

Salinity, alkalinity, and pH were measured immediately after squeezing, following the procedures in Gieskes et al. (1991). Salinity was measured using a Fisher temperature-compensated handheld refractometer, pH was measured with a combination glass electrode, and alkalinity was determined by Gran titration with an autotitrator (Metrohm 794 basic Titrino) using 0.1 M HCl at 25°C.

International Association for the Physical Sciences of the Oceans (IAPSO) standard seawater was used for calibration and was analyzed at the beginning and end of a batch of samples for each site and after every 10 samples. Alkalinity titrations are estimated to have a precision better than 5% based on repeated analysis of IAPSO standard seawater.

8.2.2. Ion chromatography

Sulfate, chloride, bromide, calcium, magnesium, potassium, and sodium concentrations were analyzed using ion chromatography (Metrohm 850 Professional IC) using aliquots of 100 µL that were diluted 1:100 with deionized water (18 MΩ·cm). At the beginning and end of each run, different dilutions of IAPSO standard seawater were analyzed for quality control and to determine accuracy and precision. Analytical precision was generally better than 2% for chloride, bromide, sulfate, calcium, magnesium, potassium, and sodium concentrations; however, refer to data tables in individual site chapters for reproducibility information.

8.2.3. Ammonium

Ammonium concentrations were determined using an Agilent Technologies Cary Series 100 UV-Vis spectrophotometer with a sipper sample introduction system, following the protocol in Gieskes et al. (1991). Concentrations of ammonium were estimated based on alkalinity measurements to determine the appropriate dilutions for analysis. For ammonium measurements in samples with an alkalinity of <20 mM, a 0.2 mL sample aliquot was diluted with 2 mL nanopure water. To each diluted sample, 1 mL phenol ethanol, 1 mL sodium nitroprusside, and 2 mL oxidizing solution (trisodium citrate and sodium hydroxide) were added to a sample tube (Gieskes et al., 1991). The solution was kept at room temperature in the dark for ~6.5 h to develop color. Ammonium concentrations were determined at a spectral absorbance of 640 nm. Because of the low levels of ammonium measured during this expedition, precision and accuracy of the ammonium analyses are estimated to be <50% for Sites U1579 and U1580; however, for each site, the individual site chapter data tables should be consulted for a more accurate assessment of the analytical uncertainties.

8.2.4. Major and minor elements in dissolved interstitial water samples using inductively coupled plasma–atomic emission spectroscopy

Dissolved major (sodium [Na^+]; potassium [K^+]; calcium [Ca^{2+}]; sulfur, which is assumed to be sulfate [SO_4^{2-}]; and magnesium [Mg^{2+}]) and minor (lithium [Li], strontium [Sr], boron [B], silicon [Si], manganese [Mn], iron [Fe], phosphorus [P], and barium [Ba]) element concentrations were determined by ICP-AES with an SPS4 autosampler. Emission wavelengths for sample analysis are presented in Table **T13**. The shipboard ICP-AES analyses of IW samples followed an analytical

Table T13. Emission wavelengths for ICP-AES analysis. **Download table in CSV format.**

Element	Wavelength (nm) for IW samples	Wavelength (nm) for sediments and rocks
Al		396.152
Ba	455.403	230.424
B	249.772	
Ca	317.933	317.933
Fe	238.204	238.204
K	766.491	766.491
Li	670.783	
Mg	202.582	279.078
Mn	257.61	257.610
Na	330.298	589.592
P		177.434
S	180.669	180.669
Si		288.158
Sr	421.552	421.552
Ti		368.520
V		292.401
Zn		213.857
Zr		327.307

protocol originally developed at the Institute for Chemistry and Biology of the Marine Environment (ICBM; Germany). Each acidified IW sample was diluted 1:10 by adding 500 µL IW and 100 µL spike solution containing 100 ppm each of beryllium (Be), indium (In), and scandium (Sc) internal standards and 200 ppm antimony (Sb) to 4.4 mL 2% HNO_3 in 18 MΩ·cm deionized water. The multielement spike was used to cover both atomic and ionic interferences (B. Schnetger, pers. comm., 2017). For calibration, serial dilutions of IAPSO standard seawater (10%, 30%, 50%, 70%, 90%, and 100%) were prepared to cover IW concentrations smaller than or equal to normal seawater. Additional calibration solutions for major and minor element concentrations exceeding seawater (Ca, B, Ba, Fe, Li, Mn, P, Si, and Sr) were prepared in 3.5% NaCl as a matrix. Calibration solutions were spiked in the same way as the IW samples. Calibration solutions were made from certified stock solutions for minor elements (B, Ba, Fe, Li, Mn, P, Si, and Sr).

During each ICP-AES run, a complete set of all in-house and IAPSO dilutions were analyzed at the beginning and end of each batch. Furthermore, 100% concentration solutions of in-house and IAPSO standards were run every 8–10 samples to monitor instrumental drift. Elemental concentrations reported for each sample were average values from three replicate integrations of each sample measured consecutively by continuous flow, as set by instrumental parameters; the standard error in the average was also calculated by the instrument software.

Following each ICP-AES run, measured concentrations were recalculated after setting background correction parameters and adjusting peak centers using the software that accompanies the ICP-AES instrument. Replicate analyses of IAPSO standard seawater between every 10 IW samples were used to estimate the accuracy and precision of the measurements for all elements, which typically was lower than 5%. Precision was determined by the instrument from threefold runs of each sample; however, data tables for individual site chapters should be consulted for a more accurate assessment of the analytical uncertainties.

8.2.5. Headspace hydrocarbon analyses

The shipboard organic geochemistry monitoring program included determination of the composition and concentrations of volatile hydrocarbons (C_1–C_6) in sediment to ensure that gas content did not exceed amounts safe for drilling operations.

One headspace gas sample was routinely taken at the top of the lowermost 150 cm section of each core. The headspace gas sampling procedure involved placing ~5 cm^3 of sediment into a glass serum vial immediately following core retrieval. The glass vial was then quickly sealed with a polytetrafluoroethylene/silicone septum and aluminum crimp cap and heated at 70°C for 30 min to allow for gas liberation from the sediment. Following the heating period, a 5 mL volume of headspace gas from the headspace in the vial was removed with a gas-tight glass syringe for analysis using gas chromatography.

The headspace gas samples were analyzed using an Agilent 7890A gas chromatograph (GC) equipped with a flame ionization detector (FID). The GC was equipped with an electronic pressure control module to control the overall flow into the instrument. A stainless steel GC column (2.4 m × 3.2 mm inner diameter) packed with 80/100 mesh HayeSep R was used for separation. The oven program started at a temperature of 35°C for 4 min before ramping at 25°C/min to 200°C, with a final hold time of 15.6 min. The total run time per gas sample was 15 min. Data were collected and evaluated with an Agilent Chemstation data handling program. Concentrations of methane (C_1), ethane (C_2), ethene ($C_{2=}$), propane (C_3), propene ($C_{3=}$), butanes (C_4), pentanes (C_5), and hexanes (C_6) were recorded. The chromatographic response was calibrated against known standards to determine concentrations in sediment. Gas standards were measured routinely once per day, or more frequently as required, to monitor instrument stability.

8.3. Carbonate and organic sediment geochemistry

8.3.1. Sediment nitrogen and inorganic and organic carbon content

Sediment samples for carbonate, organic carbon, and nitrogen analysis were routinely collected from 1–2 horizons per core, and additional samples were taken from intervals of distinct lithologies. Prior to analysis for TC, TIC, and TN, samples were frozen, freeze-dried for ~12 h, and then

homogenized using an isopropyl cleaned agate mortar and pestle or a ball mill for hard and consolidated sediments. TS was measured on samples of special lithology (e.g., organic carbon–rich black shale).

TC, TN, and TS of the sediment samples were determined with a ThermoElectron FlashEA 1112 CHNS elemental analyzer equipped with a ThermoElectron packed column CHNS/NCS GC and a thermal conductivity detector (TCD). Approximately 10–15 mg of sediment was weighed into a tin cup and combusted at 950°C under an oxygen stream. The reaction gases passed through a reduction chamber to reduce nitrogen oxides to nitrogen and then were separated using gas chromatography before detection by TCD. All measurements were calibrated to a standard (Soil Reference Material [NIST2704]; sulfanilamide for sulfur), which was run every 10 samples. The peak areas from the TCD were calculated to determine the TC, TN, and TS of the samples. Typical precision was 5% for replicate analyses of a carbonate sample; however, data tables in individual site chapters should be consulted for further reproducibility information.

TIC was determined using a UIC 5015 CO_2 coulometer. Around 10 mg of sediment was weighed into a glass vial and acidified with 2 M HCl. The liberated CO_2 was titrated, and the corresponding change in transmittance in the coulometric cell was monitored using a photodetection cell. The weight percent of calcium carbonate ($CaCO_3$) was calculated from the inorganic carbon content:

$$CaCO_3\ (wt\%) = TIC\ (wt\%) \times 100/12.$$

Standard $CaCO_3$ (>99.9%; Fisher Scientific) was used to confirm accuracy. TOC content was calculated by subtraction of inorganic carbon from the TC:

$$wt\%\ TOC = (wt\%\ TC) - (wt\%\ TIC).$$

8.3.2. Bulk organic matter source and thermal maturity

The type and quantity of organic matter in sediments with ≥2 wt% TOC were evaluated by pyrolysis assay using a source rock analyzer (SRA) from Weatherford Laboratories. Between 60 and 180 mg of freeze-dried, ground sediment was weighed into SRA crucibles. The sample was heated at 340°C for 3 min, releasing volatile hydrocarbon (HC) as the S1 peak (mg HC/g rock). The temperature was increased from 340° to 640°C at 25°C/min, resulting in hydrocarbon release from the pyrolysis of kerogen (S2 peak; mg HC/g rock). The temperature of the maximum rate of hydrocarbon yield during the S2 analysis is T_{max}. The S3 peak constitutes CO_2 (as mg C/g rock) released during pyrolysis between 340° and 390°C. CO_2 (as mg C/g rock) produced by oxidizing the pyrolysis residue at 580°C is the S4 peak, which is not reported. To validate the calculated TOC derived from the elemental analyzer we calculated TOC_{SRA} from S1, S2, and S4, assuming that S1 and S2 are 83% carbon:

$$wt\%\ TOC_{SRA} = [0.83 \times (S1 + S2) + S4]/10.$$

The carbon-normalized hydrogen index (HI) (mg HC/g TOC) and the oxygen index (OI) (mg CO_2/g TOC) were calculated from pyrolysis values:

$$HI = (100 \times S2)/TOC_{SRA}, \text{ and}$$

$$OI = (100 \times S3)/TOC_{SRA}.$$

The production index (PI) as thermal maturity indicator was calculated as follows:

$$PI = S1/(S1 + S2).$$

All SRA measurements were preceded by a blank and calibrated to a rock standard from Weatherford Laboratories (533; PN:810-141-B). The same standard was used for quality control every 10 samples.

8.4. Inorganic sediment and hard rock geochemistry

Sediment samples were analyzed for whole rock major and minor elements using ICP-AES at a minimum resolution of 50 m and a higher resolution through intervals of interest. Besides petro-

graphic core and thin section descriptions (see **Igneous petrology**), a representative set of igneous rocks were also geochemically characterized using ICP-AES and XRF analysis. In general, ICP-AES samples were taken from the same (or adjacent) intervals from which thin sections were produced. To receive rapid preliminary information on the selected samples, all sample powders produced for ICP-AES analytics were measured with the pXRF instrument prior to digestion. To help distinguish macroscopically similar but geochemically distinct igneous units (e.g., different lava flows for which contact boundaries are not preserved) during core description and as an additional guide for shipboard ICP-AES sampling, pXRF measurements were also conducted on the split core surfaces on the archive halves.

8.4.1. Sample preparation

Sample preparation for sediment samples was carried out on 2–5 cm^3 splits of squeeze cakes. Splits were frozen in a –80°C freezer and then freeze-dried for at least 12 h or until dry. Freeze-dried samples were powdered in a ball mill prior to weighing for digestion.

Sample preparation for hard rock samples was carried out on 2–8 cm^3 of igneous rock, which was cut from the cores using a diamond-blade rock saw. To remove altered rinds as well as saw marks and any drilling-related contamination on the exterior, the outer surfaces of the samples were ground off using a diamond-impregnated grinding wheel. Afterward, each rock sample was cleaned in a beaker with isopropanol in an ultrasonic bath for 15 min to remove dust. After decanting the isopropanol, the samples were agitated twice in an ultrasonic bath in 18 MΩ·cm nanopure deionized water for 10 min. After drying the cleaned samples for 10–12 h at 110°C to remove water, the rock samples were crushed to <1 cm between two Delrin plastic disks in a hydraulic press.

The crushed rock chips were ground to a fine powder using a tungsten carbide SPEX 8515 Shatterbox powdering system. Potential contamination from powdering in tungsten carbide mills was checked during ODP Leg 206 (Shipboard Scientific Party, 2003a) and appeared to be negligible for major elements and most of the trace elements measured on board the ship (Sc, V, Cr, Ni, Sr, Y, Zr, and Ba). A systematic analysis of the shipboard powders from Integrated Ocean Drilling Program Expedition 304/305, however, indicated possible Co contamination during powder preparation (Godard et al., 2009). Before further processing the powder for ICP-AES and volatile analytics, pXRF measurements were conducted.

8.4.2. Volatile measurements

Volatile content of igneous rock samples was measured using the loss on ignition (LOI) method. On a Mettler Toledo balance, about 5000 mg of the sample powder was weighed into quartz crucibles, ignited for 4 h at 950°C, and weighed after cooling in a desiccator to determine LOI. Estimated relative uncertainties on LOI values for 5000 mg samples are ~0.2% on the basis of duplicate measurements.

8.4.3. Rock and sediment inductively coupled plasma–atomic emission spectroscopy

The standard shipboard procedure for digestion of rocks and sediments and the subsequent ICP-AES analysis is described in detail in Murray et al. (2000) and the shipboard user guide for ICP-AES, with modifications as indicated in the Expedition 369 methods chapter (Huber et al., 2019a). The following protocol is a synopsis of this procedure with minor changes and additions.

On a Cahn C-31 microbalance, each sample and standard was weighed to 100.0 ± 0.5 mg. The weighing errors are estimated to be ±0.2 mg under relatively smooth sea-surface conditions but can be larger in case of high swell and bad weather conditions. Aliquots of ignited whole-rock powders or nonignited sediment powders were mixed with 800.0 ± 0.5 mg of $LiBO_2$ flux (preweighed on shore). To prevent the fused bead from sticking to the crucible during cooling, aqueous LiBr solution (10 µL of 0.172 mM) was added to the flux and rock powder mixture as a nonwetting agent prior to sample fusion. Samples were fused individually in Pt-Au (95:5) crucibles for ~12 min at a maximum temperature of 1220°C in an internally rotating induction furnace (Bead Sampler NT-2100).

The beads were then transferred into 50 mL high-density polyethylene (HDPE) bottles and dissolved in a 50 mL solution of 10 wt% HNO_3 (prepared from Optima-grade concentrated HNO_3). The solution bottle was placed in a Burrell wrist-action shaker for 3–6 h at 7°C to aid dissolution, and then 0.5 mL of the sample solution was pipetted into a polyethylene centrifuge tube and diluted with 4.4 mL of 10 wt% HNO_3 and 0.1 mL of internal standard solution containing Be (100 µg/g), In (100 µg/g), and Sb (200 µg/g). This solution was analyzed for both major and trace elements.

8.4.4. Analysis

For the sediment analysis, major and trace element concentrations of standards and samples were determined using ICP-AES. The analyzed major elements include Si, Ti, Al, Fe, Mg, Mn, Ca, Na, K, and P, and minor or trace elements include V, Zn, Sr, Zr, and Ba. Matrix-matched multielement solutions were made for instrument calibration by mixing 0.5 mL of flux blank, 0.1 mL of internal standard (detailed above), the appropriate volume of multielement solution, and 10% trace metal grade nitric acid to bring the solution to 5 mL. The calibration was checked with certified international reference standards (HISS-1 and MESS-4), and drift was monitored with three check standards run every 10 samples.

For igneous rock analysis, major and trace element concentrations of standards and samples were also determined using ICP-AES. The analyzed major elements include Si, Ti, Al, Fe, Mg, Mn, Ca, Na, K, and P, and trace elements include Sc, V, Co, Ni, Cu, Zn, Sr, Y, Zr, and Ba. Emission wavelengths for the analysis of samples are presented in Table **T13**. In a first run, matrix-matched multielement solutions were used for instrument calibration (see above). For a second run, certified international rock reference materials (BCR-2, BHVO-2, BIR-1, JA-1, JA-2, JA-3, JB-3, JGb-1, and MRG-1) were used for calibration and drift monitoring. Chemical procedural blanks were included with the unknown samples for each sample run. Detection limits were calculated as three times the standard deviation of the mean for blank solution measurements.

The ICP-AES plasma was ignited at least 20 min before each sample run to allow the instrument to warm up and stabilize. ICP-AES data were acquired using Agilent's ICP Expert software. The intensity curve for each element is defined by 20 measurements within the designated wavelength window. The Expert software integrates the area delineated by the baseline and the intensity curve. Each sample was analyzed three times from the same dilute solution in a given sample run. For several elements, measurements were made at two or more wavelengths in axial/radial mode. For each run, the wavelength yielding the best calibration line was identified and used to determine concentrations.

A drift-correction sample (in-house standard of Be, In, and Sb mixed with equal amounts of all samples to be 400 mg in total) was analyzed in every fifth sample position and at the beginning and end of each run. Procedural blank solutions were run near the beginning and end of each run and at every ~25 sample positions. A 10% HNO_3 wash solution was run for 90 s between each sample analysis.

8.4.5. Data reduction

A drift correction was applied to each element based on linear interpolation between drift-monitoring solutions run every fourth or fifth analysis. After drift correction and subtraction of the average procedural blank, a calibration line for each element was calculated using the results for the certified rock standards. Concentrations used for the calibrations were compiled values from the literature as detailed in Table **T14**; they were recalculated on a volatile-free basis for those samples with LOI > 2%. Total Fe oxide concentrations were reported as $Fe_2O_3^t$. The compiled values were from Govindaraju (1994) and the GeoRem website (**http://georem.mpch-mainz.gwdg.de**) (Jochum et al., 2005). Element concentrations in the samples were then calculated from the relevant calibration lines. Blank measurements were used to determine detection limits. Estimates of accuracy and precision of major and trace element analyses were based on replicate analyses of international standards run as unknowns and were not used in the calibration. Results are presented in Table **T15**.

8.4.6. Portable X-ray fluorescence spectrometry measurements

pXRF spectrometry measurements, made using an Olympus DeltaX handheld instrument, provided rapid characterization of split core surfaces and powder samples for assessment of chemical variations and how they may (or may not) tie to petrographic observables. For practical reasons, only qualitative measurements (ratios) were used during Expedition 392; thus, no external data calibrations against international rock standards were performed. However, internal calibration

Table T14. Accepted values for the rock standards used for calibration of major and trace element ICP-AES analyses, Expedition 392. **Download table in CSV format.**

Standard	Al (wt%)	B (ppm)	Ba (ppm)	Ca (wt%)	Ce (ppm)	Co (ppm)	Cr (ppm)	Cu (ppm)	Eu (ppm)	Fe (wt%)	K (wt%)	La (ppm)	Li (ppm)	Mg (wt%)	Mn (wt%)	Mo (ppm)
MRG-1	8.47		61	14.7		87	430	134		17.94	0.18			13.55	0.17	0.87
BCR-2	13.48	4.4	683.9	7.114	53.12	37.33	15.85	19.66	1.989	13.77	1.774	25.08	9.13	3.599	0.1966	250.6
BHVO-2	13.44	2.95	130.9	11.4	37.53	44.89	287.2	129.3	2.043	12.39	0.513	15.2	4.5	7.257	0.169	4.07
BIR-1	15.35	0.25	7	13.24	1.92	51.4	382	126	0.5201	11.26	0.027	0.627	3.203	9.68	0.171	0.5
JA-1	8.06	21	311	4.07	13.3	12.3	7.83	43	1.2	4.95	0.64	5.24	10.8	0.95	0.122	1.59
JA-2	8.16	20.7	321	4.5	32.7	29.5	436	29.7	0.93	4.34	1.5	15.8	27.3	4.58	0.084	0.6
JA-3	8.23	24.8	323	4.46	22.8	21.1	66.2	43.4	0.82	4.62	1.17	9.33	14.5	2.24	0.081	1.89
JB-3	9.1	18	245	7	21.5	34.3	58.1	194	1.32	8.27	0.65	8.81	7.21	3.13	0.137	1.09
JGb-1	9.26	4.03	64.3	8.5	8.17	60.1	57.8	85.7	0.62	10.53	0.2	3.6	4.59	4.73	0.146	0.59
JP-1	0.35	1.4	19.5	0.39	0.19	116	2807	6.72	0.004	5.85	0.002	0.084	1.79	26.9	0.094	0.087
JR-1	6.79	117	50.3	0.48	47.2	0.83	2.83	2.68	0.3	0.62	3.66	19.7	61.4	0.07	0.077	3.25
JR-2	6.73	145	39.5	0.36	38.8	0.46	3.1	1.36	0.14	0.54	3.69	16.3	79.2	0.02	0.087	3.35

Standard	Na (wt%)	Nb (ppm)	Ni (ppm)	P (wt%)	Rb (ppm)	S (ppm)	Sc (ppm)	Si (wt%)	Sr (ppm)	Ta (ppm)	Ti (wt%)	U (ppm)	V (ppm)	Y (ppm)	Zn (ppm)	Zr (ppm)
MRG-1	0.74	20	193	0.08	8.5	610	55	39.12	266		3.77	0.24	526	14	191	108
BCR-2	3.12	12.44	12.57	0.3593	46.02		33.53	54	337.4	0.786	2.265	1.683	417.6	36.07	129.5	186.5
BHVO-2	2.219	18.1	119.8	0.2685	9.261		31.83	49.6	394.1	1.174	2.731	0.412	318.2	25.91	103.9	171.2
BIR-1	1.75	0.6	166	0.046	0.25		44	47.77	108	0.0414	0.96	0.01	313	16	71	15.5
JA-1	2.85	1.85	3.49	0.072	12.3	21.6	28.5	29.9	263	0.13	0.51	0.34	105	30.6	90.9	88.3
JA-2	2.31	9.47	130	0.064	72.9	8	19.6	26.37	248	0.8	0.4	2.21	126	18.3	64.7	116
JA-3	2.37	3.41	32.2	0.051	36.7	214	22	29.11	287	0.27	0.42	1.18	169	21.2	67.7	118
JB-3	2.03	2.47	36.2	0.128	15.1	9.86	33.8	23.82	403	0.15	0.86	0.48	372	26.9	100	97.8
JGb-1	0.89	3.34	25.4	0.024	6.87	1910	35.8	20.41	327	0.18	0.96	0.13	635	10.4	109	32.8
JP-1	0.02	1.48	2460		0.8	26.9	7.24	19.81	3.32	0.02		0.036	27.6	1.54	41.8	5.92
JR-1	2.98	15.2	1.67	0.009	257	13.3	5.07	35.27	29.1	1.86	0.066	8.88	7	45.1	30.6	99.9
JR-2	2.96	18.7	1.99	0.005	303	9.6	5.59	35.38	8.11	2.29	0.04	10.9	3	51.1	27.8	96.3

Table T15. Results of analyses of international rock reference materials used during analysis as check standards, Expedition 392. BDL = below detection limit. **Download table in CSV format.**

Standard	Al (wt%)	Ba (ppm)	Ca (wt%)	Co (ppm)	Cu (ppm)	Fe (wt%)	K (wt%)	Mg (wt%)	Mn (wt%)	Na (wt%)	Ni (ppm)	Sc (ppm)	Sr (ppm)	Ti (wt%)	V (ppm)	Y (ppm)	Zn (ppm)	Zr (ppm)
BHVO-2	10.00	135.69	11.00	37.54	124.99	11.79	0.42	6.85	0.15	1.77	112.61	32.89	398.11	2.58	329.79	27.30	96.93	174.97
BHVO-2	10.33	141.16	12.07	46.01	136.13	12.51	0.46	7.44	0.15	1.81	129.91	34.48	405.80	2.57	353.81	28.28	98.98	184.11
BHVO-2	11.24	147.72	13.38	50.75	151.72	13.28	0.45	8.17	0.16	1.84	133.50	36.86	428.86	2.58	380.65	30.68	96.97	198.18
BHVO-2	10.88	147.57	13.64	59.09	139.08	13.28	0.43	8.34	0.16	1.76	138.24	37.68	427.96	2.59	377.40	32.20	96.36	197.04
BHVO-2	11.32	149.42	14.10	50.16	145.93	13.52	0.47	8.59	0.16	1.83	129.47	37.69	441.06	2.62	393.18	31.20	95.92	203.16
BHVO-2	9.89	138.01	10.14	42.99	144.21	10.97	0.42	6.42	0.15	1.78	94.48	32.54	411.00	2.63	313.83	26.96	100.06	173.20
BHVO-2	10.25	140.87	10.27	46.03	150.40	11.42	0.41	6.45	0.15	1.82	108.65	33.07	416.18	2.67	324.00	27.20	103.80	179.07
BHVO-2	9.91	136.87	9.86	40.45	143.77	11.23	0.42	6.34	0.15	1.76	100.05	32.59	402.82	2.62	312.54	26.54	95.07	175.04
Average:	10.48	142.16	11.81	46.63	142.03	12.25	0.44	7.33	0.15	1.79	118.36	34.73	416.47	2.61	348.15	28.80	98.01	185.60
±:	0.59	5.38	1.72	6.76	8.63	1.03	0.02	0.94	0.00	0.03	16.54	2.32	14.92	0.03	32.38	2.22	2.84	12.07
BIR-1	11.81	8.91	13.18	51.48	129.58	10.85	0.02	9.14	0.16	1.45	168.34	46.54	110.64	0.92	345.00	16.72	67.50	16.33
BIR-1	12.06	9.22	14.04	54.61	133.37	11.30	0.03	9.70	0.16	1.48	182.66	48.17	112.39	0.93	344.29	17.00	67.39	15.85
BIR-1	12.43	9.52	15.51	64.63	129.38	11.92	0.02	10.57	0.16	1.47	191.41	50.89	116.59	0.93	376.46	18.88	66.75	15.26
BIR-1	13.02	10.30	16.48	67.50	134.29	12.69	0.03	11.22	0.16	1.51	215.51	53.19	119.40	0.93	387.93	18.41	70.12	17.99
BIR-1	12.84	9.94	16.64	67.42	127.99	12.96	BDL	11.29	0.16	1.47	219.71	53.22	119.17	0.90	396.06	18.60	67.46	17.45
BIR-1	11.38	8.94	11.77	48.41	135.16	10.62	0.01	8.34	0.15	1.44	162.43	45.32	111.19	0.91	311.30	16.61	69.17	14.95
BIR-1	11.36	9.20	11.71	46.76	135.21	10.00	0.02	8.33	0.15	1.42	148.38	45.25	111.58	0.93	311.05	16.73	67.61	15.28
BIR-1	11.48	8.97	11.74	48.25	138.20	10.24	0.02	8.32	0.15	1.43	156.77	45.49	110.89	0.91	314.43	16.41	70.90	16.52
Average:	12.05	9.37	13.89	56.13	132.90	11.32	0.02	9.61	0.16	1.46	180.65	48.51	113.98	0.92	348.32	17.42	68.36	16.20
±:	0.66	0.51	2.11	8.96	3.55	1.10	0.00	1.28	0.00	0.03	26.61	3.46	3.78	0.01	35.00	1.02	1.50	1.09

and data corrections of the instrument were tailored for geological applications and are based on the Fundamental Parameters methodology. Accordingly, a series of nonlinear equations is solved for each element analyzed. Parameters used in the equations comprise metrics for X-ray source, fluorescence intensities, absorption coefficients, and absorption edge effects for each wavelength analyzed, along with parameters for sample geometry and a Compton normalization scheme (e.g., Reynolds, 1963; van Sprang, 2000). All measurements during Expedition 392 were performed using the Geochemistry program of the instrument with 30 s counting time for each of the two beams, respectively. Measurements on split core surfaces were conducted using a shield sleeve analyzer mount. For these analyses, 3525 Ultralene 0.16 mil (4 µm) film was placed over the core interval to prevent contamination and/or damage to the X-ray analyzer (e.g., Johnston et al., 2018). In addition, powders prepared for ICP-AES analysis were measured using XRF powder mount assemblies based on methods outlined in Reagan et al. (2015). Reference standard BHVO-2 was analyzed with each set of unknowns to track instrument performance over time.

9. Physical properties

High-resolution petrophysical measurements were made during Expedition 392 on cores in the shipboard physical properties laboratory and using downhole (in situ) logging tools (see **Downhole measurements**). These data play a major role in hole-to-hole and site-to-site stratigraphic correlation, detection of stratal discontinuities and inhomogeneities, obtaining information about differences in the composition and texture of sediments and underlying basement rocks, identification of major seismic reflectors, and construction of synthetic seismograms. A variety of techniques and methods were used to characterize the physical properties of Expedition 392 cores on whole-round, section-half, and discrete samples. Core sections are typically 1.5 m in length, such that a typical coring length (stroke) of 9.5 m with full recovery yields six sections plus a shorter seventh and core catcher section. Procedures for measuring sediment, lithified sediment, and hard rock (e.g., igneous rock) cores differ slightly.

9.1. General physical properties sampling and measurement sequence

9.1.1. Measurements of sediment core sections

After recovery and curation of core sections, whole-round sections were initially run through the NGRL (Figure **F15**). Selected core sections were then run through the X-Ray Imager (XRI) (Figure **F16**). Following thermal equilibration at ambient room temperature (~20°C) and atmospheric pressure for ~4 h, the core sections were run through the WRMSL to measure bulk density using the GRA method, MS, and compressional wave velocity on the *P*-wave logger (PWL) (Figure **F17**).

When an interval of stratigraphy was cored in multiple holes, core sections were run through the STMSL immediately upon recovery, measuring just GRA bulk density and MS at a lower sampling resolution (5 cm) prior to equilibration to help with rapid stratigraphic correlation to inform drilling decisions. Because some of the physical properties measurements are particularly sensitive to temperature, all fast-tracked sections were remeasured using the WRMSL at a 2.5 cm sampling resolution following the standard 4 h thermal equilibration period.

Thermal conductivity was measured on one whole-round section per every one or two sediment cores (typically Section 3) (Figure **F18**). For soft sediments these data were collected with a needle probe inserted into a hole drilled through the plastic core liner near the middle of the whole-round section. The cores were then split longitudinally, with one half to be archived and the other half for sampling and analysis (working half). For more consolidated sediments, the puck probe was used to measure the working-half section for thermal conductivity.

Following splitting of the section, the archive half of the core was passed through the SHMSL for measurement of MSP and color reflectance at a nominal sample interval of 2.5 cm (Figure **F19**). Two-dimensional X-ray images were taken from the archive half of the core through select intervals of interest at each site (Figure **F16**).

Discrete samples were collected from one to two sections of the working halves of the split sections of the core (typically Sections 2 and 4 or 5) to measure wet bulk density, dry bulk density, water content, porosity, and grain density using moisture and density (MAD) procedures (Figure **F20**). Where possible, samples were taken as close to the middle of the core sections as core conditions permitted. However, in some cases, there was poor core recovery or the cores consisted of numerous small fragments (biscuits); in such cases, the most suitable and representative discrete

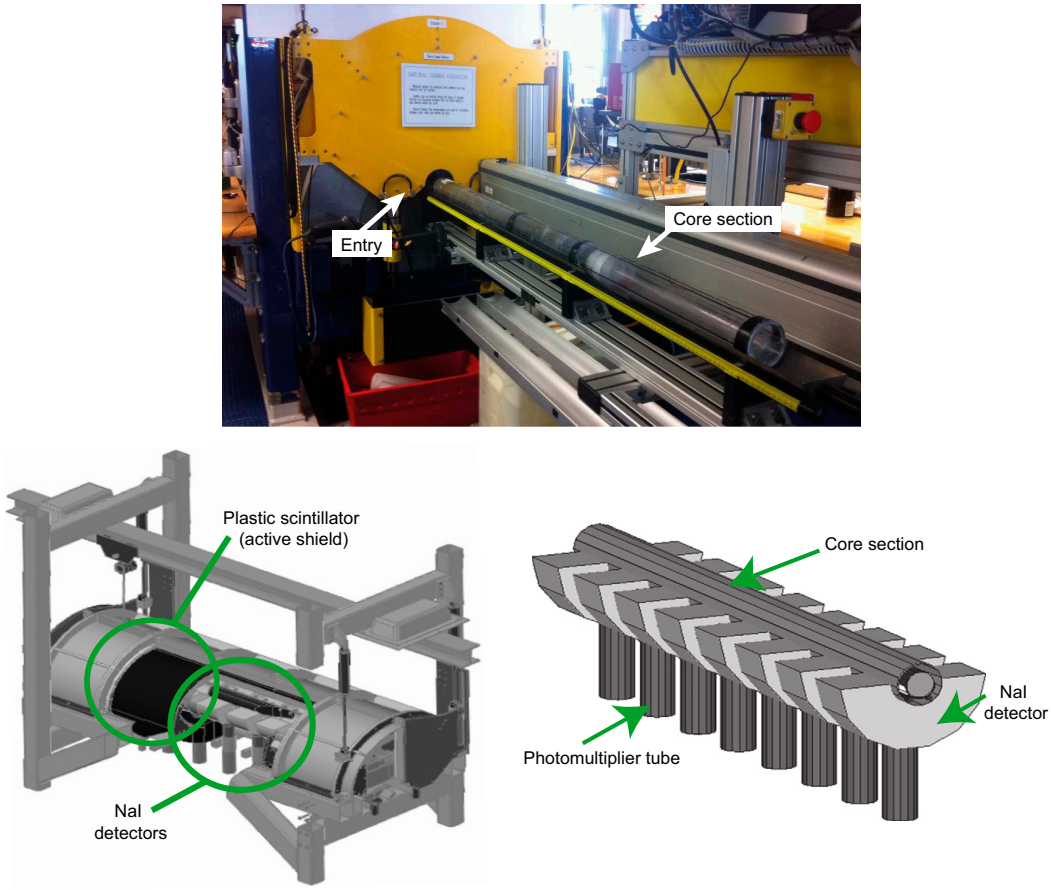

Figure F15. NGRL system (Vasiliev et al., 2011).

Figure F16. XRI system.

rock samples of these cores were selected. Such biscuiting is normally only an issue in XCB and RCB cores across variable lithologies. At sites where multiple holes provided overlapping intervals, the cores from additional parallel holes were not sampled; only nondestructive analyses (e.g., WRMSL and SHMSL) were collected (see above). *P*-wave velocity was also measured on working halves and cubic samples (in *x*-, *y*-, and *z*-directions) using the SHMG, a contact acoustic velocity logger using an acoustic transducer and first arrival traveltimes to estimate the *P*-wave velocity (Figure **F21**).

9.1.2. Measurements of hard rock core sections

Hard rock cores, consisting of basalt, were recovered with the RCB coring method. These cores were run through the NGRL and the WRMSL, as described for the sedimentary cores (Figures **F15**, **F17**). Hard rock core sections containing fragments were shaken onto liners in the core splitting room for examination by a petrologist, who decided where the pieces should be split between working and archive halves (see **Introduction** for curatorial procedures). The archive half of the core was passed through the SHMSL (Figure **F19**) for measurement of MSP and color reflectance at a nominal sample interval of 2.5 cm. The hard rock samples were saturated with seawater before measurements of thermal conductivity, *P*-wave velocity, and MAD analysis. Thermal conductivity was measured once per core using a contact puck probe on a piece of a section half (Figure **F18**). *P*-wave velocity was measured on one to two sections per core using the SHMG for discrete hard

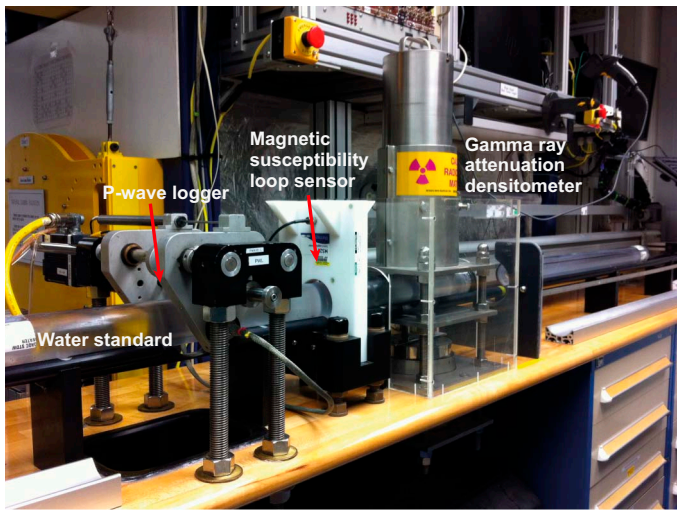

Figure F17. WRMSL.

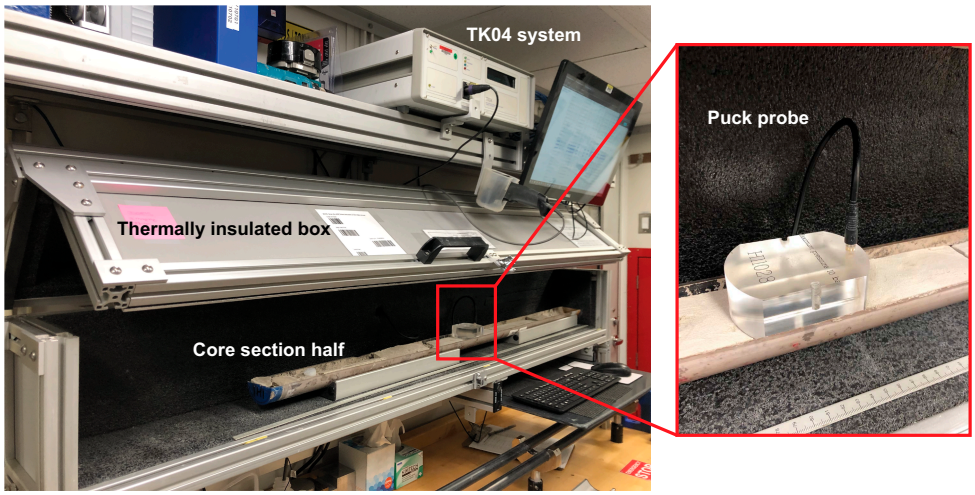

Figure F18. Thermal conductivity (TK04) system.

rock samples (Figure **F21**). MAD measurements (Figure **F20**) were also taken on these samples or from discrete samples or core fragments obtained from the same lithology from a position near where *P*-wave caliper velocity was measured.

A full discussion of all methodologies and calculations used aboard *JOIDES Resolution* in the physical properties laboratory is available in Blum (1997). Details and procedures for each physical properties measurement are described below.

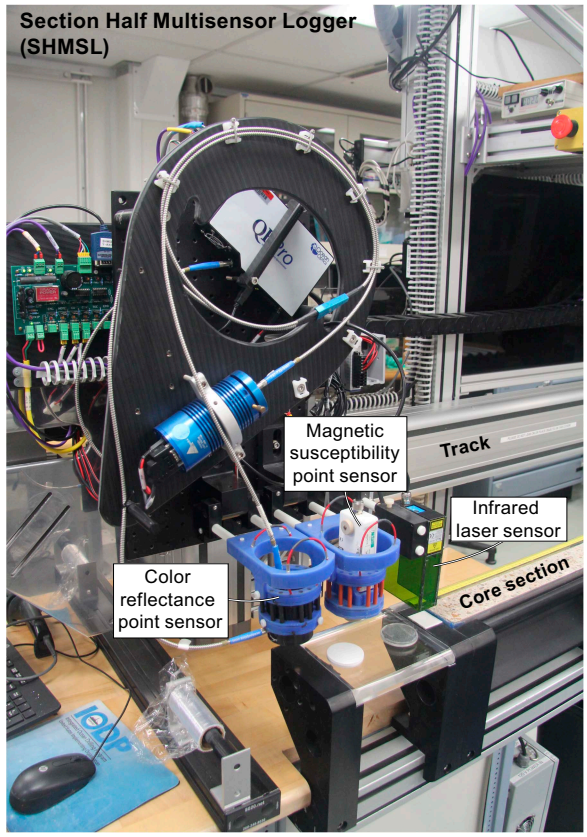

Figure F19. SHMSL used on archive section halves.

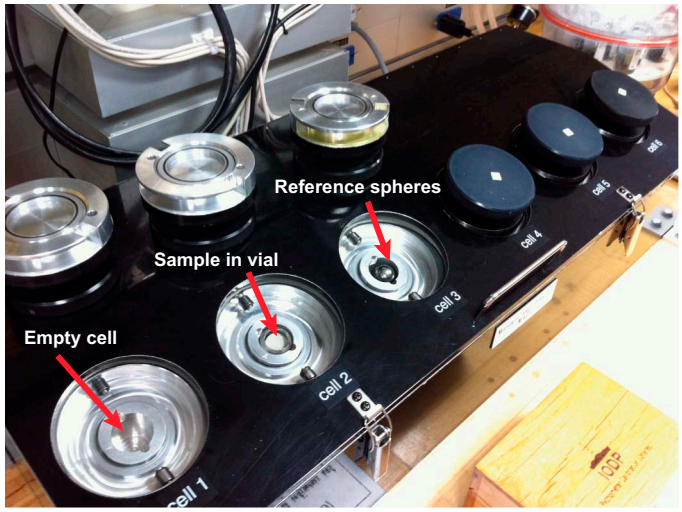

Figure F20. Pycnometer cells for MAD measurements.

9.2. Whole-Round Multisensor Logger core measurements

GRA bulk density, *P*-wave velocity, and MS of cores were measured nondestructively on the WRMSL (Figure F17). To optimize the process, sampling intervals and measurement integration times were the same for all sensors. Sampling intervals were set at 2.5 cm with an integration time of 5 s for each measurement. These sampling intervals are common denominators of the distances between the sensors installed on the WRMSL (30–50 cm), which allows for efficient sequential and simultaneous measurements. After every core was analyzed, the fidelity of the measurements was monitored by passing a single core liner filled with deionized water through the WRMSL.

9.2.1. Gamma ray attenuation bulk density

The GRA densitometer (Figure F17) provides an estimate of bulk density of core based on the attenuation of a gamma ray beam. The beam is produced by a ^{137}Cs gamma ray source at a radiation level of 370 MBq within a lead shield with a 5 mm collimator, which is directed through the whole-round section. The gamma ray detector on the opposite side from the source includes a scintillator and an integral photomultiplier tube to record the gamma radiation that passes through the core. The attenuation of the gamma rays occurs primarily by Compton scattering, in which the gamma rays are scattered by electrons in the formation. The degree of scattering is related to the material bulk density. The density (ρ) is proportional to the intensity of the attenuated gamma rays and can be expressed as

$$\rho = -\ln(I/I_0)/(\mu d),$$

where

I = the measured intensity of gamma rays passing through the sample,
I_0 = gamma ray source intensity,
μ = Compton attenuation coefficient, and
d = sample diameter.

The μ, I_0, and d are treated as constants, such that ρ can be calculated from I.

In general, WRMSL GRA bulk density measurements are most accurate when taken on a completely filled core liner with minimal drilling disturbance; otherwise, measurements tend to underestimate true values. By default, the instrument reports measurements using the internal diameter of the core liner (66 mm) as the assumed sample diameter. This assumption is suitable for most sediment cores obtained using the APC system. For sediment and/or hard rock cored using the XCB or RCB systems, core diameter is usually ~58 mm or less, resulting in an underestimated density for these cores.

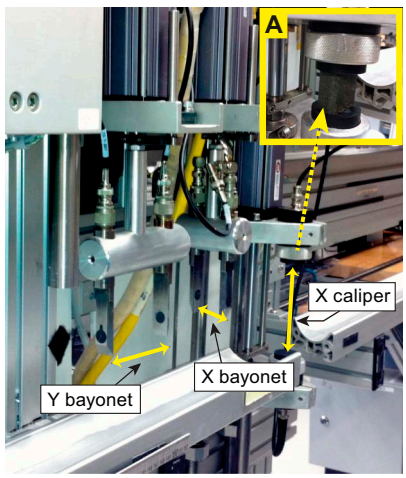

Figure F21. SHMG *x*-axis caliper and *y*- and *z*-axis bayonets used to measure *P*-wave velocity on split-core sections of soft sediment and discrete samples of indurated sediment or igneous rock. A. *P*-wave velocity measurement on an igneous rock discrete sample using the *x*-axis caliper.

Beginning with GRA bulk density data from Hole U1581B, a density correction was applied to account for the actual volume of the core sample. The laser sensor of the color reflectance spectrophotometer measures the sample's height above core track with a resolution of 0.01 cm. The following equation was used to calculate the area of a circular segment (a):

$$a = R^2\left(\frac{d}{R}\right) - d\sqrt{R^2 - d^2},$$

using the difference (d) between the reference and measured elevation of the top surface of split half core section and the radius of the core liner (R = ~3.59 cm). The density correction ($\Delta\rho$) can be calculated comparing the true measured segment area (a) and the archive half area of the core liner's cross section (a_0):

$$\Delta\rho = \rho_{GRA}\frac{a_0 - a}{a_0},$$

where ρ_{GRA} is the measured GRA bulk density. The corrected density values (ρ'_{GRA}) are obtained as follows:

$$\rho'_{GRA} - \rho_{GRA} + \Delta\rho .$$

The reflectance spectroscopy expanded profile data were downloaded from LIMS database, smoothed using a median filter, and interpolated in the location of the GRA bulk density measurements.

The spatial resolution of the GRA densitometer is less than ±1 cm. The gamma ray detector is calibrated with sealed calibration cores (one standard core liner filled with distilled water and aluminum cylinders of various diameters). To establish the calibration curves, gamma ray counts were taken through each aluminum cylinder for 60 s. Each aluminum cylinder has a density of 2.7 g/cm^3, and d is from 1 cm to 6 cm. The relationship between I and μd is as follows:

$$\ln(I) = A(\mu d)^2 + B(\mu d) + C,$$

where the coefficients A, B, and C are instrument constants determined from the calibration. Recalibration was performed as needed when the estimated deionized water density standard deviated significantly (more than a few percent) from 1 g/cm^3.

9.2.2. Magnetic susceptibility

MS (χ) is a dimensionless measure of the degree to which a material can be magnetized by an external magnetic field:

$$\chi = M/H,$$

where M is the magnetization induced in the material by an external field of strength H. The bulk MS of a rock depends on its mineralogical composition and sometimes the size of the mineral grains. Ferrimagnetic minerals (e.g., magnetite and maghemite) have relatively high positive MS and produce a large bulk MS even when present at low concentrations in rocks. Antiferromagnetic (hematite and goethite) and paramagnetic (smectite, illite, and chlorite) minerals have lower positive MS and can produce weak bulk rock MS in the absence or near-absence of ferromagnetic minerals. Diamagnetic minerals (calcite, quartz, and kaolinite) have very low and negative MS and produce null or slightly negative bulk rock MS in the absence of other magnetic minerals (e.g., in chalk or a pure limestone). Igneous materials typically have MS two orders of magnitude greater than their alteration products, such as clay minerals.

WRMSL MS measurements were made on whole-round core sections using a Bartington MS2C loop sensor (Figure **F17**). An oscillator circuit in the sensor operates at a frequency of 0.565 kHz and produces a low-intensity, nonsaturating alternating magnetic field of ~140 A/m. Sediment or hard rock core sections within the influence of this field cause a change in oscillator frequency. Frequency information returned in a pulse form to the susceptometer is converted into MS. The loop sensor is about 25 mm wide, and measurements had a spatial resolution of ~10 cm and precision to within 2%. Note that higher spatial resolution MS data are also collected on section halves by the SHMSL (see below), and bulk MS data are collected for discrete cubes during AMS analyses (see **Paleomagnetism**).

9.2.3. *P*-wave velocity

P-wave velocity data can be used to evaluate small-strain (linear elastic) moduli, to correlate between downhole logging and core data, and to evaluate porosity and compaction in sedimentary rocks. *P*-wave (compressional) velocity (V_P) is determined by measuring the time required for a compressional wave to travel a specific distance through the core:

$$V_P = d/t_{core},$$

where d is the path length of the wave across the core and t_{core} is the traveltime.

The PWL on the WRMSL (Figure **F17**) measures the first arrival traveltime of 500 kHz ultrasonic waves traveling horizontally across the core while it remains in the core liner. Waves are transmitted to the core by plastic transducer contacts connected to linear actuators. Pressure is applied to the actuators to ensure coupling between the transducers and the core liner. The seismic waves radiate from the source across the whole core and core liner. The total traveltime t_0 is the sum of the following:

- t_{delay} = time delay related to transducer faces and electronic circuitry,
- t_{pulse} = delay related to the peak detection procedure,
- t_{liner} = transit time through the core liner, and
- t_{core} = traveltime through the core.

The system is calibrated using a core liner filled with distilled water, which provides control for t_{delay}, t_{pulse}, and t_{liner}. From these calibrations, V_P can be calculated for the whole-round sections in core liners as follows:

$$V_P = (d_{cl} - 2d_{liner})/(t_o - t_{pulse} - t_{delay} - 2t_{liner}),$$

where

d_{cl} = measured diameter of core and liner, and
d_{liner} = liner wall thickness.

The above equation assumes that the core completely fills the core liner.

9.3. Natural Gamma Radiation Logger core measurements

Gamma radiation is emitted because of the spontaneous decay of radioactive elements 238-uranium (^{238}U), 232-thorium (^{232}Th), and 40-potassium (^{40}K) contained in all rocks. The NGRL measures this natural emission on whole-round sections using a system designed and built at the Integrated Ocean Drilling Program–US Implementing Organization (USIO) (Texas A&M University, USA) (Figure **F15**) (Vasiliev et al., 2011; Dunlea et al., 2013). When ^{238}U, ^{232}Th, and ^{40}K radioisotopes decay, they and their daughter products emit gamma radiation at specific energy levels unique to each isotope. NGR spectroscopy measures a wide energy spectrum that can be used to estimate the abundance of each isotope based on the strength of the signal at characteristic energies (Blum, 1997; Gilmore, 2008). In sedimentary rocks, Th and K are usually associated with particular clay minerals, and U is often encountered in either clay minerals or organic-rich material. Because minor changes in the abundance of clay minerals produce a relatively large variation in gamma radiation, the NGR data are useful as a lithologic indicator, aiding in core-to-core correlation. The NGR spectral data were processed to estimate U, Th, and K contents with depth using the method and Matlab routines by de Vleeschouwer et al. (2017).

The NGRL system was installed on the renovated research vessel *JOIDES Resolution* in 2009 and has been used on every *JOIDES Resolution* expedition starting with Expedition 320. The NGRL system consists of 8 sodium iodide (NaI) detectors arranged at 20 cm intervals under the lower half of the core section (Figure **F15**). The data were collected in two measurement cycles, each of which produced NGRL measurements at 8 positions in the core section. During the first measurement cycle, the first detector was located 10 cm from the top of the core section, thus producing 8 measurements at positions that are odd multiples of 10 cm from the top of the core. The core was then advanced 10 cm, producing another 8 measurements at positions that are even multiples of

10 cm from the top of the core. The detector array has both passive (layers of lead) and active (plastic scintillators) shielding to reduce the background environmental and cosmic radiation. The plastic scintillators are positioned above the core section and detect incoming high-energy gamma and muon cosmic radiation that is removed from the total counts of the NaI detectors. The passive (lead) layers separate the NaI detectors, isolating the portion of the core being measured. The quality of the energy spectrum measured in a core depends on the concentration of radionuclides in the sample and on the measurement time, with longer duration measurements yielding better spectra. Measurement times were chosen to be 5 min per measurement cycle, or ~10 min per core section. This yields statistically significant energy spectra for most lithologies (Vasiliev et al., 2011).

9.4. Thermal conductivity core measurements

Thermal conductivity was typically measured on one section per core (usually Section 3) with the TK04 (Teka Bolin) system (Figure **F18**) using a needle probe method in full-space configuration for whole-round sediment cores for poorly consolidated sediments (Von Herzen and Maxwell, 1959) and contact probe method in half-space configuration on split cores using a puck sensor applied to most of sedimentary and hard rock samples. The probes contain a heater wire and calibrated thermistor.

For hard rock cores, samples were selected from the working half and returned unaltered to the core liner upon completion of the tests. Measurements were taken with a contact probe embedded in the surface of an epoxy block with low thermal conductivity (Vacquier, 1985). The epoxy block and the probe were placed in contact with the sample, and both were placed in a plastic container filled with seawater.

To measure thermal conductivity, the probe heat source was turned on and the increase in temperature was recorded over 80 s. A heating power of about twice the tabulated average rock conductivity was typically used. The solution to the heat conduction equation with a line source of heat was then fit to the temperature measurements to obtain the thermal conductivity. Because the probe is much more conductive than sediments or basalts, the probe is assumed to be a perfect conductor. Under this assumption, the temperature of the probe has a linear relationship with the natural logarithm of the time after heating is initiated:

$$T(t) = (q/4\pi k) \times \ln(t) + C,$$

where

T = temperature (K),
q = heat input per unit length per unit time (W/m),
k = thermal conductivity of the sample (W/[m·K]),
t = time after the initiation of the heat source (s), and
C = instrument constant.

Three measuring cycles were automatically performed, with the probe and sample allowed to reequilibrate for 10 min between each cycle. A test for instrument drift was conducted at the beginning of each measurement cycle. Once the probe temperature stabilized, the heater circuit was closed and the temperature rise in the probe was recorded. Thermal conductivity was calculated from the rate of temperature rise while the heater current was flowing. Temperatures measured during the first 80 s of the heating cycle were fitted to an approximate solution of a constantly heated line source (for details, see Kristiansen, 1982; Blum, 1997). The conductivity was taken to be the average of the values from the three determined at each cycle. Measurement errors were 5%–10%.

9.5. Section Half Multisensor Logger core measurements

Color reflectance and MS were measured by the core description team on the archive section halves using the SHMSL (Figure **F19**). The archive half of the split core was placed on the core track, above which an electronic platform moves along a track, recording the height of the split-core surface with a laser sensor. The laser establishes the surface topography of the section, and

then the platform reverses the direction of movement, moving from the core section top (higher in the borehole) to end (lower in the borehole) making measurements of MSP and color reflectance. Also, because the SHMSL requires a firm contact between the MS point sensor and the split core surface, measurements were made on the archive halves of split cores. MSP and color reflectance data were collected at a nominal interval of 2.5 cm for each core.

9.5.1. Color reflectance spectrophotometry

The color reflectance spectrometer uses an Ocean Optics USB4000 spectrophotometer mounted on the automated SHMSL. This uses both halogen and LED light sources, which cover wavelengths from ultraviolet through visible to near infrared. The measurements were taken from 380 to 900 nm wavelengths at 2 nm intervals on the core sections. A 3 s data acquisition time was applied for the entire scan of the archive section half. The data are reported using the L*a*b* color system, in which L* is lightness, a* is redness (positive) versus greenness (negative), and b* is yellowness (positive) versus blueness (negative) of the rock. The color reflectance spectrometer calibrates on two spectra, pure white (reference) and pure black (dark). Color calibration was conducted approximately once every 6 h (twice per shift), and plastic film was used to cover soft-sediment sections to prevent material from collecting on the detectors.

9.5.2. Point magnetic susceptibility

MSP measurements were taken with a Bartington Instruments MS2E point sensor and an MS2K contact probe with a flat 15 mm diameter round sensor with a field of influence of 25 mm and an operation frequency of 930 Hz. The instrument averages three measurements from the sensor at each position on the core, providing an accuracy of ~5%. The spatial resolution of the MSP instrument is ~3.8 mm, higher than the ~10 cm resolution of the MS loop on the WRMSL. The probe is zeroed in air slightly above the core before each measurement to compensate for the influence of the metal track. The MSP sensor was calibrated by the manufacturer before installation on the ship and is quality checked every 6 h at the same time as the color reflectance sensor calibration.

9.6. X-ray imaging

JOIDES Resolution is equipped with an XRI consisting of a Teledyne ICM CP120B X-ray generator and detector unit (Figure **F16**). The instrument measures density contrasts in core sections. During Expedition 392, the XRI was applied to selected whole-round sections and section halves. Given time and core workflow constraints, not all sections were imaged. Core sections were X-ray imaged for the following reasons: (1) to document important lithologic or geological boundaries, (2) to assess the disturbance of poorly lithified sediments in APC core sections, (3) to detect possible occurrence of macrofossils or lithoclasts, or (4) to investigate sedimentary structures.

The X-ray generator works with a maximum voltage of ~120 kV and a tube current of ~1 A and has a 0.8 mm × 0.5 mm focal spot. The generator produces a directional cone at a beam angle of 50° × 50°. The detector unit is located 65 cm from the source and consists of a Go-Scan 1510 H system composed of an array of complementary metal oxide semiconductor (CMOS) sensors arranged to offer an active area of 102 mm × 153 mm and a resolution of 99 µm. Core sections were run through the imaging area at 12 cm intervals, providing images of 15 cm onto the detector and allowing an overlap of 3 cm.

The XRI settings were adjusted to compensate for the varying lithologies of the cores. The number of images stacked was 20, taken at exposure times of 300 s, and the current was kept at 0.7 mA. The voltage ranged between 70 and 90 kV; higher voltages were used for denser lithologies.

The raw XRI images were collected as 16-bit images and were processed using an IODP in-house processing utility in the IMS software (version 1.3). The software applies corrections for the detector (gain and offset corrections), compensates for core shape and thickness, and adjusts the image contrast. The Savitzky-Golay FIR filter was chosen to smooth images. The resulting processed images include a masked background, the depth scale of the section, and the acquisition parameters. The software applies different processing to APC (or HLAPC) and RCB cores.

9.7. Velocity, moisture, and density discrete core measurements

Discrete samples were collected from the working halves of the core to determine wet and dry bulk density, grain density, water content, and porosity. Samples were typically taken from two sections per core, with additional samples taken as warranted by lithology changes. At sites where multiple holes provided overlapping intervals, the duplicate cores were not sampled. In soft sediment, ~10 cm^3 samples were collected with a plastic syringe and placed in glass vials for measurements. The cores composed of strongly lithified sediments and hard rocks were analyzed by cutting a sample with a saw from the working halves. These samples often corresponded to the same intervals as collected for discrete paleomagnetic analyses. Discrete *P*-wave velocity measurements (in *x*-direction) were taken on intact core sections with the positions coinciding as much as possible with the MAD sample locations. For cores that did not present intact sections, *P*-wave velocity measurements were taken on either the MAD samples, or on larger pieces obtained from the same core section and with the same lithology, and as close as possible to the MAD sample location.

9.7.1. Sample preparation

Soft-sediment samples were placed in numbered, preweighed ~16 mL Wheaton glass vials for wet and dry sediment weighing, drying, and dry volume measurements. To determine the wet mass of well-lithified samples (typically basalt), we placed the samples in individual plastic vials filled with seawater and used a vacuum chamber to force saturation of the pore space. The vacuum pump removed the air from the chamber to a pressure of ~40–50 kPa below the atmospheric pressure. This, in theory, would force seawater into the pore space of the samples. These samples were kept under saturation for at least 6 h, with low pressure maintained in the chamber by turning the pump on for 15 min every 2 h. After removal from the saturator, the cubes were patted dry with a paper towel, and the wet mass was immediately determined using the dual balance system.

9.7.2. *P*-wave velocity

The *P*-wave velocity acquisition system installed on the SHMG uses Panametrics-NDT Microscan delay line transducers (Figure **F21**), which transmit seismic waves at 0.5 MHz. The signal received through a discrete sample was digitally recorded, and the first arrival time was picked automatically or manually. The distance between the transducers was measured with a built-in linear voltage displacement transformer. Calibration was performed with a series of acrylic cylinders with various thicknesses and a known *P*-wave velocity of 2750 ± 20 m/s. The system time delay, determined from the calibration, was subtracted from the picked arrival time to estimate the *P*-wave traveltime through the sample. The thickness of the sample (calculated by the linear voltage displacement transformer) was divided by the traveltime to calculate the *P*-wave velocity in meters per second.

9.7.3. Dual balance mass measurement

The weights of wet and dry samples were determined to a precision of 0.005 g using two Mettler Toledo electronic balances, with one acting as a reference. A standard weight of similar value to the sample (within ±5 g) was placed upon the reference balance to increase accuracy. A computer averaging system was used to compensate for the ship's motion. The default setting of the balances is 300 measurements (taking ~1.5 min).

9.7.4. Pycnometer volume measurement

Dry sample volume was determined using a six-celled, custom-configured Micrometrics AccuPyc 1330TC helium-displacement pycnometer (Figure **F20**). The precision of each cell is 1% of the full-scale volume. Volume measurement was preceded by three purges of the sample chamber with helium warmed to ~28°C. Three measurement cycles were run for each sample. A reference volume (two calibration spheres) was placed in one of the chambers during each set of measurements to check for instrument drift and systematic error (Figure **F20**). The reference volume was moved sequentially between chambers, such that each chamber was calibrated in turn every 5 sets of measurements. The volumes occupied by the Wheaton vials used for soft-sediment samples were calculated before the cruise by dividing each vial's weight by the average density of the vial glass. Dry mass and volume were measured after samples were heated in an oven at 105° ± 5°C for 24 h and allowed to cool in a desiccator for 3 h. The procedures for the determination of these

physical properties comply with the American Society for Testing and Materials (ASTM) designation (D) 2216 (ASTM International, 1990). The fundamental relation and assumptions for the calculations of all physical properties parameters are discussed by Blum (1997) and summarized below.

9.7.5. Mass and volume calculation

We measured wet mass (M_{wet}), dry mass (M_{dry}), and dry volume (V_{dry}). Salt precipitated in sediment pores during the drying process is included in the M_{dry} and V_{dry} values. The mass of the evaporated water (M_{water}) and salt (M_{salt}) in the sample are given by the following:

$$M_{water} = M_{wet} - M_{dry}, \text{ and}$$

$$M_{salt} = M_{water}[s/(1 - s)],$$

where s is the assumed seawater salinity (3.5%) corresponding to a pore water density (ρ_{pw}) of 1.024 g/cm^3 and a salt density (ρ_{salt}) of 2.22 g/cm^3. The corrected mass of pore water (M_{pw}), volume of pore water (V_{pw}), mass of solids excluding salt (M_{solid}), volume of salt (V_{salt}), volume of solids excluding salt (V_{solid}), and wet volume (V_{wet}) are as follows:

$$M_{pw} = (M_{wet} - M_{dry})/rm,$$

$$V_{pw} = M_{pw}/\rho_{pw},$$

$$M_{solid} = M_{wet} - M_{pw},$$

$$M_{salt} = M_{pw} - (M_{wet} - M_{dry}),$$

$$V_{salt} = M_{salt}/\rho_{salt},$$

$$V_{wet} = V_{dry} - V_{salt} + V_{pw}, \text{ and}$$

$$V_{solid} = V_{wet} - V_{pw},$$

where rm = 0.965 is the ratio of mass between equal volumes of the fresh and seawater.

9.7.6. Calculation of bulk properties

For all sediment samples, water content (w) is expressed as the ratio of mass of pore water to wet sediment (total) mass:

$$w = M_{pw}/M_{wet}.$$

Wet bulk density (ρ_{wet}), dry bulk density (ρ_{dry}), sediment grain density (ρ_{solid}), porosity (ϕ), and void ratio (VR) are calculated as follows:

$$\rho_{wet} = M_{wet}/V_{wet},$$

$$\rho_{dry} = M_{solid}/V_{wet},$$

$$\rho_{solid} = M_{solid}/V_{solid},$$

$$\phi = V_{pw}/V_{wet}, \text{ and}$$

$$VR = V_{pw}/V_{solid}.$$

MAD properties reported in the Physical properties sections of all site chapters were calculated with the MADMax shipboard program using the program's predefined Method C. In Method C, the wet and dry bulk mass and dry bulk volume are measured, and the other physical properties are derived using the above equations.

10. Downhole measurements

Downhole measurements during Expedition 392 consisted of wireline logging runs and in situ formation temperature measurements at select holes.

10.1. Wireline logging

Downhole logs generate in situ measurements of physical, chemical, and structural properties of the geologic formations penetrated by the borehole. Data are rapidly collected, continuously with depth, and measured in situ; data can be interpreted in terms of the stratigraphy, lithology, mineralogy, magnetic characteristics, and geochemical composition of the penetrated formations. Logging provides important data that characterize the borehole sections where core recovery is incomplete or disturbed. Where core recovery is good, log and core data complement each other and may be interpreted jointly.

Downhole logs provide measurements of physical properties of the formations on a scale that is intermediate between those obtained from laboratory measurements on core samples and those from geophysical surveys. Downhole logs are useful in calibrating the interpretation of geophysical survey data (e.g., through the use of synthetic seismograms) and provide a necessary link for the integrated understanding of physical and chemical properties on different scales.

Wireline logging during Expedition 392 was successfully performed at two of the four sites to aid in core-log-seismic integration, fill in lithologic information across poorly recovered intervals, and obtain oriented structural measurements. During wireline logging operations, the logs were recorded with Schlumberger logging tools combined into tool strings, which were lowered into the hole after completion of coring operations. Several downhole logging methods and corresponding configurations of tool strings were used during Expedition 392 (Figure **F22**), including (1) the triple combination (triple combo) tool string, which measured NGR, density, and resistivity along with porosity and MS; (2) the quadruple combination (quad combo) tool string, which measured seismic velocity along with the standard triple combo measurements minus porosity; (3) the FMS-sonic tool string, which provided electrical resistivity images of the borehole wall and seismic velocities of the rock formation; and (4) the UBI and NGR combination tool string. Each tool string also contained an Enhanced Digital Telemetry Cartridge (EDTC) for communicating through the wireline to the Schlumberger multi-tasking acquisition and imaging system (MAXIS) on the vessel. To help stabilize the borehole walls for logging, the boreholes were cleaned and cleared using the drill bit (reamed), flushed of debris using drilling fluid, and unless a UBI run was scheduled, filled with seawater-based logging gel (sepiolite mud mixed with seawater and weighted with barite; approximate density = 10.5 lb/gal or 1258 kg/m^3). The BHA was pulled up to ~70–150 m wireline log matched depth below seafloor (WMSF) to expose the deeper borehole wall for wireline measurement and to stabilize the upper portion of the hole. The tool string was then lowered downhole on a seven-conductor wireline cable before being pulled up at constant speed to provide continuous log measurements of several properties simultaneously.

Each tool string deployment is termed a "logging run," and data collection during each lowering or hauling-up of the tool string constitutes a "pass". The measurements during each run were performed using the following sequence of operations: (1) recording while the tool string was lowered to the bottom of the hole (downpass), (2) high-resolution recording over selected depth intervals (where applicable), and (3) recording on the way up (main pass). Repeatable measurements help to increase the accuracy and obtain better images using the FMS and UBI borehole images. The caliper log data can be acquired only on ascending (main) passes. Therefore, measurements that require information on the borehole diameter are less accurate for downpasses. Incoming data were recorded and monitored in real time on the Schlumberger Minimum Configuration MAXIS (MCM) logging computer. A wireline heave compensator (WHC) was used to minimize the effect of the heave of the ship on the tool position in the borehole (see **Wireline heave compensator**).

10.1.1. Wireline logged rock properties and tool measurement principles

The logged properties and the principles used in the tools that measure them are briefly described below. More detailed information on individual tools and their geological applications may be

found in Serra (1984, 1986, 1989), Schlumberger (1989, 1994), Rider (1996), Goldberg (1997), Lovell et al. (1998), and Ellis and Singer (2007). A complete online list of acronyms for the Schlumberger tools and measurement curves can be found at **https://www.apps.slb.com/cmd**.

10.1.2. Downhole natural gamma radiation

The HNGS measured borehole NGR during each logging run (Figure **F22**). The HNGS uses two bismuth germanate scintillation detectors and five-window spectroscopy to determine concentrations of potassium (in weight percent), thorium (in parts per million), and uranium (in parts per million) from the characteristic gamma ray energies of isotopes in the ^{40}K, ^{232}Th, and ^{238}U radioactive decay series, which dominate the natural radiation spectrum. The computation of the elemental abundances uses a least-squares method of extracting U, Th, and K elemental concentrations from the spectral measurements. The HNGS filters out gamma ray energies below 500 keV, eliminating sensitivity to bentonite or KCl in the drilling mud and improving measurement accuracy. The HNGS also provides a measure of the HSGR and uranium-free (or computed gamma ray [HCGR]) that are measured in American Petroleum Institute gamma radiation units (gAPI). The HNGS response is influenced by the borehole diameter; therefore, the HNGS data are corrected for borehole diameter variations during acquisition using caliper data.

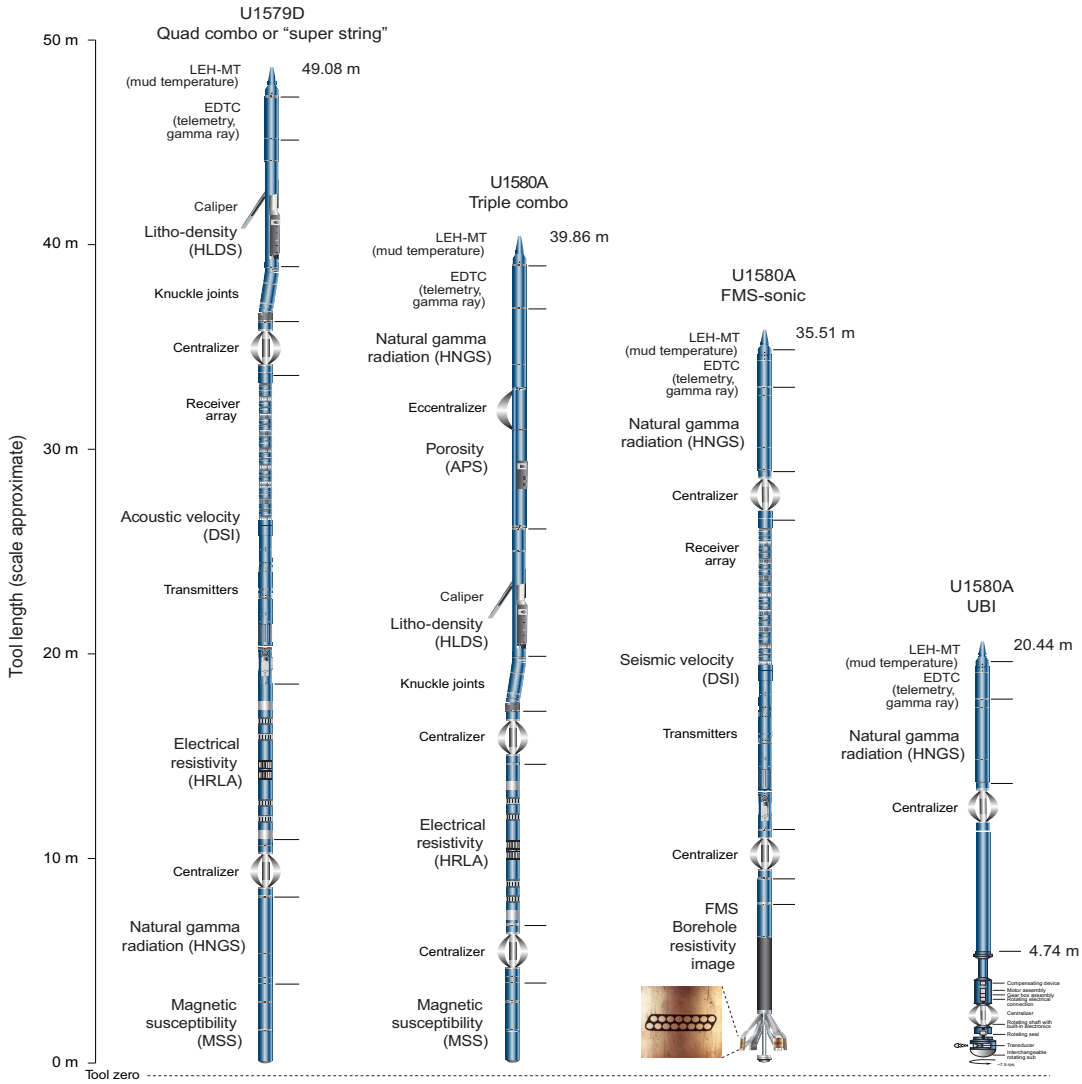

Figure F22. Downhole logging assemblies used during Expedition 392. LEH-MT = logging equipment head-mud temperature, EDTC = Enhanced Digital Telemetry Cartridge, HLDS = Hostile Environment Litho-Density Sonde, DSI = Dipole Shear Sonic Imager, HRLA = High-Resolution Laterolog Array, HNGS = Hostile Environment Natural Gamma Ray Sonde, MSS = Magnetic Susceptibility Sonde, APS = Accelerator Porosity Sonde, FMS = Formation MicroScanner.

An additional NGR sensor was housed in the EDTC at the top of each tool string (Figure **F22**). The EDTC is primarily used to communicate data to the vessel. The sensor includes a sodium iodide scintillation detector that also measures the total NGR emission of the formation. It is not a spectral tool (it does not provide U, Th, or K concentrations), but it provides total intensity of gamma radiation for each pass. The HNGS is normally included in the triple combo, quad combo, and FMS-sonic tool strings to help precisely match depths between logging strings and passes and can additionally be used for core-log integration.

10.1.3. Density and photoelectric effect

Formation density was measured downhole using the Hostile Environment Litho-Density Sonde (HLDS). The HLDS contains a radioactive cesium (^{137}Cs) gamma ray source (622 keV) and far-offset and near-offset gamma ray detectors mounted on a shielded skid that is pressed against the borehole wall by a hydraulically activated decentralizing arm. Gamma rays emitted by the source undergo Compton scattering, in which gamma rays are scattered by electrons in the formation. The intensity of scattered gamma radiation is proportional to the electron density of the material, which is related to bulk density. Porosity may also be derived from this bulk density if the matrix (grain) density is known.

The HLDS also measures the photoelectric effect (PEF), a measure of the photoelectric absorption of low-energy gamma radiation. PEF absorption is dependent on elemental composition/mineralogy and can be used as a lithology indicator. Photoelectric absorption occurs when the energy of photons falls below 150 keV as a result of being repeatedly scattered by electrons in the formation. PEF is determined by comparing the counts from the far detector in the high-energy region, where only Compton scattering occurs, with those in the low-energy region, where count rates depend on both reactions. Because PEF depends on the atomic number of the elements in the formation (heavier elements have higher PEF), the photoelectric absorption varies according to the chemical composition of the minerals present and can be used for the identification of the mineral species in the formation. For example, the PEF of calcite is 5.08 barn/e$^-$, illite is 3.03 barn/e$^-$, quartz is 1.81 barn/e$^-$, potassium feldspar is 2.86 barn/e$^-$, and pure pyrite is 16.97 barn/e$^-$ (where barn = 10^{-24} cm^2). A firm contact between the tool and borehole wall is essential for good quality HLDS logs because drilling mud entrained at the contact with borehole wall may result in underestimation of density values. The density correction and the borehole size corrections should be applied for correct interpretation. In the deeper parts of the hole, the PEF log should be used with caution, especially in washouts, because barium (element with high atomic mass) contained in the logging mud can bias the signal, even when the mud correction is applied. These data were recorded during wireline logging and are available at the Lamont Doherty Earth Observatory (LDEO) logging database (**https://mlp.ldeo.columbia.edu/logdb/scientific_ocean_drilling**) but are not discussed in expedition site chapters.

10.1.4. Porosity

Formation porosity was measured downhole using the Accelerator Porosity Sonde (APS). The APS includes a minitron neutron generator, which produces fast (14.4 MeV) neutrons, and five neutron detectors (four for epithermal neutrons and one for slow thermal neutrons) positioned at different distances from the minitron. The tool's detectors count neutrons that arrive at the detectors after being scattered and slowed by collisions with atomic nuclei in the formation.

The highest energy loss occurs when neutrons collide with hydrogen nuclei, which have practically the same mass as the neutron (the neutrons bounce off heavier elements without losing much energy). If the hydrogen (or, equivalently, water molecule) concentration is low, as in low-porosity formations, neutrons can travel farther before being captured and the count rates increase at the detector. The opposite effect occurs in high-porosity formations where the water content is high. However, because hydrogen-containing minerals such as clays and hydrocarbons also contribute to the measurement, the raw porosity value is often an overestimate.

10.1.5. Electrical resistivity

The High-Resolution Laterolog Array (HRLA) tool provides six resistivity measurements with different depths of investigation (including the borehole or mud resistivity and five measurements of

formation resistivity with increasing penetration into the formation). The tool sends a focused electrical current into the formation and measures the intensity necessary to maintain a constant drop in voltage across a fixed interval, providing direct resistivity measurements. The array has one central (source) electrode and six electrodes above and below it, which serve alternatively as focusing and returning current electrodes. By rapidly changing the role of these electrodes, a simultaneous resistivity measurement at six penetration depths is achieved. The tool is designed so that all signals are measured simultaneously and the sensitivity to "shoulder bed" effects is reduced when crossing sharp beds thinner than the electrode spacing. The design of the HRLA, which eliminates the need for a surface reference electrode, improves formation resistivity evaluation compared to traditional dual induction and allows the full range of resistivity to be measured, from low (e.g., in high-porosity sediments) to high (e.g., in basalt). The HRLA needs to be run centralized in the borehole for optimal results, so knuckle joints were used to centralize the HRLA and allow the density and porosity tools to maintain good contact with the borehole wall.

Calcite, silica, and hydrocarbons are electrical insulators, whereas ionic solutions like IW are conductors. Electrical resistivity, therefore, can be used to evaluate porosity for a given salinity and resistivity of the IW. Clay-surface conduction also contributes to the resistivity values, but at high porosities this is a relatively minor effect.

10.1.6. Seismic logging

The Dipole Shear Sonic Imager (DSI) measures the transit times between sonic transmitters and an array of eight receivers (Figure **F22**). It combines replicate measurements, thereby providing a direct measurement of seismic velocity through formations that is relatively free from the effects of formation damage and an enlarged borehole (Schlumberger, 1989). The DSI can also measure seismic anisotropy when operating in anisotropic mode, which was used to obtain complementary structural information at Site U1580.

The DSI combines high-speed telemetry with simultaneous, 12-bit dynamic range digitization of an eight-receiver array. The DSI incorporates both monopole and crossed-dipole transmitters with an eight-station array of electronically configurable hydrophones for monopole and dipole reception. Combining new dipole-based technology with the latest monopole developments into one system provides the best method available today for obtaining borehole compressional and shear wave slowness. The dipole source excites flexural, compressional, and shear head waves. The flexural waves are helpful to characterize shear velocity anisotropy and velocities in slow formations (with shear velocity less than in the borehole fluid) often encountered in deep-ocean drilling.

The elastic anisotropy of formations can be characterized by shear wave splitting observations. In a vertical borehole inside a transversely isotropic medium with a horizontal symmetry axis (e.g., because of vertical fractures), the shear wave splits into two waves propagating with different speeds. The polarization of the fast and slow shear wave components depends only on the fast and slow direction of the formation and does not depend on the orientation of the source dipole. For instance, the fast component aligns parallel to the plane of the fractures, whereas the slow wave polarization is perpendicular to the plane of the fractures. The flexural wave also splits into fast and slow components aligned with the formation anisotropy.

Processing with the MAXIS wellsite unit displays full seismic waveforms and the component characteristics. The MAXIS high-speed array processor uses the slowness-time-coherence method to determine compressional and shear wave slowness values.

10.1.7. Formation MicroScanner

The FMS provides high-resolution electrical resistivity–based images of borehole walls. The tool has four orthogonal arms and pads, each containing 16 button electrodes that are pressed against the borehole wall during logging. The electrodes are arranged in two diagonally offset rows of eight electrodes each. A focused current is emitted from the button electrodes into the formation, and a return electrode is arranged near the top of the tool. Resistivity of the formation at the button electrodes is derived from the intensity of the current passing through the button electrodes.

The processed FMS resistivity data are presented in the form of high-resolution images that reveal geologic structures of the borehole wall. Features such as bedding, stratification, fracturing, slump folding, and bioturbation can be resolved (Luthi, 1990; Salimullah and Stow, 1992; Lovell et al., 1998). Because the images are oriented to magnetic north, further analysis can provide measurement of the dip and direction (azimuth) of planar features in the formation (e.g., Morris et al., 2009). In addition, when the corresponding dipping planar features can be identified in the recovered core samples, individual core pieces can be reoriented with respect to true north.

The maximum extension of the caliper arms is 40.6 cm (16 inches). In holes or sections of holes with a diameter greater than this value, the pad contact at the end of the caliper arms will be inconsistent and the FMS images may appear out of focus and too conductive. For example, irregular (rough) borehole walls adversely affect the images if contact with the wall is poor. Therefore, the standard procedure is to make two full main passes with the FMS to maximize the chance of getting full borehole coverage using the pad sensor. This also helps to ensure that adequate data coverage is obtained because only ~30% of a borehole with a diameter of 25 cm is imaged during a single pass.

10.1.8. Magnetic Susceptibility Sonde

The Magnetic Susceptibility Sonde (MSS) is a nonstandard wireline tool designed by LDEO. It measures the degree to which formations are magnetized when subjected to a magnetic field. The ease of magnetization is ultimately related to the concentration and composition (size, shape, and mineralogy) of magnetic minerals in the formation, principally (titano)magnetite. These measurements provide one of the best methods for investigating stratigraphic changes in mineralogy and lithology because the measurement is quick, repeatable, and nondestructive and because different lithologies often have strongly contrasting susceptibilities. Additionally, the MSS can potentially be used to correlate logging data to cores because MS data are measured shipboard using the WRMSL and SHMSL (see **Physical properties**) and in the paleomagnetism laboratory (see **Paleomagnetism**).

The MSS dual-coil sensor provides ~1 inch resolution downhole susceptibility measurements. The MSS was run as the lowermost tool in the triple combo tool string, using a specially developed data translation cartridge to enable the MSS to be run in combination with the Schlumberger tools (Figure **F22**).

MS data from both the high-resolution and deep-reading sensors are plotted as uncalibrated instrument units (IU). The MSS reading responses are affected by temperature and borehole size (higher temperatures lead to higher susceptibility measurements). Preliminary processing was performed offshore to remove the temperature drift by calculating a least-squares polynomial fit to the data and subtracting the calculated trend from the data set. When the MS signal in sediment is very low, the detection limits of the tool may be reached. For quality control and environmental correction, the MSS also measures internal tool temperature, *z*-axis acceleration, and low-resolution borehole conductivity.

10.1.9. Ultrasonic Borehole Imager

The UBI features a high-resolution transducer that provides acoustic images of the borehole wall. The transducer emits ultrasonic pulses at a frequency of 250 or 500 kHz (low and high resolution, respectively) that are reflected at the borehole wall and then received by the same transducer. The amplitude and traveltime of the reflected signal are determined. Continuous rotation of the transducer and the upward motion of the tool produce a complete map of the borehole wall. The amplitude depends on the reflection coefficient of the borehole fluid/rock interface, the position of the UBI tool in the borehole, the shape of the borehole, and the roughness of the borehole wall. Changes in the borehole wall roughness (e.g., at fractures intersecting the borehole) are responsible for the modulation of the reflected signal. Therefore, fractures or other variations in the character of the drilled rocks can be recognized in the amplitude image. The recorded traveltime image gives detailed information about the shape of the borehole, which allows calculation of one caliper value of the borehole from each recorded traveltime. The amplitude and traveltime are recorded together with a reference to magnetic north by means of a three-component magnetometer included in the General Purpose Inclinometry Tool (GPIT), permitting the orientation of images.

The orientation of the core with respect to the true north is possible by matching characteristic lithologic and structural features observed both in the core and in the UBI images. The UBI oriented images can also be used to measure stress in the borehole through identification of borehole breakouts and slip along fault surfaces penetrated by the borehole (Paillet and Kim, 1987). In an isotropic, linearly elastic rock formation that is subjected to an anisotropic stress field, drilling a subvertical borehole causes breakouts in the direction of the minimum principal horizontal stress (Bell and Gough, 1983). Similarly, borehole breakouts may occur in elastically anisotropic (horizontal transverse isotropic [HTI]) rocks subjected to isotropic loading in the horizontal plane.

10.1.10. Acceleration and inclinometry

Three-component acceleration and magnetic field measurements were made with the GPIT during logging. The primary purpose of this tool, which incorporates a three-component accelerometer and a three-component magnetometer, is to determine the acceleration and orientation of the UBI and FMS-sonic strings. This information allows the UBI and FMS images to be corrected for irregular tool motion and to determine the dip and direction (azimuth) of features in the images.

10.2. Log data quality

The main influences on log data quality are the condition of the borehole wall and the uncertainty in the position of the logging tool along the borehole. The quality of wireline logging data, which require good contact with the borehole wall (i.e., FMS, density, and porosity), may be degraded if the borehole diameter varies over short intervals with depth because of washouts, softer material, or ledges of harder material. The measurements with deep penetration into the rock formation (such as gamma radiation, resistivity, and sonic logging) do not require a tight contact with the borehole wall and are generally less sensitive to the borehole conditions. "Bridged" sections, where the borehole diameter is much smaller than the bit size, may also bias the interpretation of downhole logging data. The data quality can be improved by minimizing the circulation of drilling fluid while drilling, flushing the borehole to remove debris, and logging as soon as possible after the borehole is completed. During this expedition, the necessity of flushing dense basement rocks up and out of the borehole required heavy fluid circulation.

The borehole diameter, measured using the caliper tool, provides an indication of formation strength and its response to the artificial erosion associated with drilling operations. Additionally, caliper measurements can provide information on the present-day stress field inferred from the borehole failure pattern induced by drilling. The method for estimating stress-field orientation uses the orthogonal borehole diameter measured with the calipers of the FMS-sonic tool string (called C1 and C2, respectively) and the caliper orientation provided by the GPIT (see **Acceleration and inclinometry**). Displaying this information along depth can provide evidence of breakouts or borehole ellipticity that can be interpreted in terms of maximum and minimum plane stresses. A breakout signal typically shows an increase in diameter in one of the orthogonal calipers, whereas the other caliper remains close to the bit size. Theoretically, the greater diameter highlights the minimum plane stress.

The quality of the wireline depth determination depends on several factors. The depth of the logging measurements is determined from the length of the cable deployed from the winch on the ship. The seafloor is identified on the NGR log by the abrupt reduction in gamma ray count at the water/sediment interface (mudline). Discrepancies between the drilling depth and the wireline log depth may occur. Drilling depth discrepancies may be due to core expansion, incomplete core recovery, or incomplete heave compensation. Log depth discrepancies between successive runs occur because of incomplete heave compensation, incomplete correction for cable stretch, and cable slip. Tidal changes in sea level affect both drilling and logging depths. These tidal ranges were predicted to be less than 0.5 m on the Agulhas Plateau while logging Sites U1579 and U1580.

10.2.1. Wireline heave compensator

During wireline logging operations, the up-and-down motion of the ship (heave) causes a similar motion of the downhole logging tools. If the amplitude of this motion is large, depth discrepancies can be introduced into the logging data. The risk of damaging downhole instruments is also

increased. A WHC system was thus designed to compensate for the vertical motion of the ship and maintain a steady motion of the logging tools to ensure high-quality logging data acquisition (Liu et al., 2013; Iturrino et al., 2013). The WHC uses a vertical accelerometer (motion reference unit [MRU]) positioned under the rig floor near the ship's center of gravity to calculate the vertical motion of the ship with respect to the seafloor. It then adjusts the length of the wireline by varying the distance between two sets of pulleys through which the cable passes to minimize downhole tool motion. Real-time measurements of uphole (surface) and downhole acceleration are made simultaneously by the MRU and the EDTC, respectively. An LDEO-developed software package allows these data to be analyzed and compared in real time, displaying the actual motion of the logging tool string and enabling monitoring of the efficiency of the compensator and using this information for the interpretation of logging data.

10.2.2. Logging data flow and log depth scales

Data for each wireline logging run were monitored in real time and recorded using the Schlumberger MAXIS 500. Initial logging data were referenced to the wireline log depth below rig floor (WRF) depth scale. After logging was completed, the data were transferred onshore to the LDEO Borehole Research Group (LDEO-BRG), where standard data processing took place. The main part of the processing workflow was to identify the depth of the seafloor based on steps in NGR and to match the depths of each individual run and pass to obtain a consistent WMSF depth scale. Additional minor corrections were applied to individual tools and logs (e.g., FMS and UBI imagery was corrected for tool acceleration, including stick and slip). The documentation for the logs with an assessment of log quality was prepared, and the data were exported to ASCII format for the conventional logs and GIF format for the FMS and UBI images. The Schlumberger Petrel/Techlog software package is used for most of the processing of the collected wireline logging data. The data were transferred back to the ship within a few days of logging, and this processed data set was made available to the science party (in ASCII and DLIS formats) through the shipboard logging database and shipboard servers. Downhole data from three sites are available through the LDEO logging database.

10.3. In situ temperature measurements

In situ formation temperature measurements were collected during Expedition 392 using the APCT-3 tool at Site U1579 on the Agulhas Plateau and Site U1581 in the Transkei Basin, where the APC system was deployed. The APCT-3 fits directly into the coring shoe of the APC system and consists of a battery pack, data logger, and a platinum resistance-temperature device calibrated over a temperature range of 0°–30°C. The nominal accuracy of the APCT-3 temperature measurements is ±0.05°C.

Before entering the borehole, the APCT-3 tool is first stopped at the mudline for 5 min to thermally equilibrate with bottom water temperatures. Occasionally during Expedition 392, the lowest temperature recorded during the run was used instead of the average temperature at the mudline as an estimate of the bottom water temperature because it was more repeatable and the bottom water is expected to have the lowest temperature in the profile. When the APC system advances into the formation, there is an instantaneous temperature rise from frictional heating. This heat gradually dissipates into the surrounding sediment as the temperature at the APCT-3 equilibrates toward the temperature of the sediment. After the APC system penetrated the sediment, it was held in place for 10 min while the APCT-3 tool recorded the temperature of the cutting shoe every second.

The equilibrium temperature of the sediment was estimated by applying a mathematical heat-conduction model to the temperature decay record (Horai and Von Herzen, 1985). The synthetic thermal decay curve for the APCT-3 tool is a function of the geometry and thermal properties of the probe and the sediment (Bullard, 1954; Horai and Von Herzen, 1985). The equilibrium temperature was estimated by fitting a parameterized theoretical temperature decay curve to the observed temperature time series (Pribnow et al., 2000). The data quality depends on the assumption that the temperature equilibration curve was not disturbed by other factors, such as ship heave pulling the APC up from full penetration.

The APCT-3 temperature data were combined with thermal conductivity measurements obtained from the whole-round and split-core sections to obtain heat flow values using the Bullard method (Bullard, 1954). Slopes and intercepts of temperature versus depth, thermal conductivity versus depth, and temperature versus thermal resistance are computed with linear regression. Uncertainties are quantified as standard deviations.

References

Abramovich, S., and Keller, G., 2003. Planktonic foraminiferal response to the latest Maastrichtian abrupt warm event: a case study from South Atlantic DSDP Site 525A. Marine Micropaleontology, 48(3):225–249. **https://doi.org/10.1016/S0377-8398(03)00021-5**

Acton, G., Morris, A., Musgrave, R., Zhao, X., and IODP SRM Personnel, 2017. Assessment of the New Superconducting Rock Magnetometer (SRM) on the *JOIDES Resolution*. **http://iodp.tamu.edu/publications/JRSO/SRM_Workshop_2017.pdf**

Acton, G.D., Borton, C.J., and the Leg 178 Shipboard Scientific Party, 2002. Palmer Deep composite depth scales for Leg 178 sites 1098 and 1099. In Barker, P.F., Camerlenghi, A., Acton, G.D., and Ramsay, A.T.S. (Eds.), Proceedings of the Ocean Drilling Program, Scientific Results. 178: College Station, TX (Ocean Drilling Program), 1–35. **https://doi.org/10.2973/odp.proc.sr.178.202.2001**

Agnini, C., Fornaciari, E., Raffi, I., Catanzariti, R., Pälike, H., Backman, J., and Rio, D., 2014. Biozonation and biochronology of Paleogene calcareous nannofossils from low and middle latitudes. Newsletters on Stratigraphy, 47(2):131–181. **https://doi.org/10.1127/0078-0421/2014/0042**

Agnini, C., Fornaciari, E., Raffi, I., Rio, D., Röhl, U., and Westerhold, T., 2007. High-resolution nannofossil biochronology of middle Paleocene to Early Eocene at ODP Site 1262; implications for calcareous nannoplankton evolution. Marine Micropaleontology, 64(3–4):215–248. **https://doi.org/10.1016/j.marmicro.2007.05.003**

Agnini, C., Muttoni, G., Kent, D.V., and Rio, D., 2006. Eocene biostratigraphy and magnetic stratigraphy from Possagno, Italy: the calcareous nannofossil response to climate variability. Earth and Planetary Science Letters, 241(3–4):815–830. **https://doi.org/10.1016/j.epsl.2005.11.005**

ASTM International, 1990. Standard method for laboratory determination of water (moisture) content of soil and rock (Standard D2216–90). In Annual Book of ASTM Standards for Soil and Rock Philadelphia (American Society for Testing Materials).

Atta-Peters, D., and Salami, M.B., 2004. Late Cretaceous to early Tertiary pollen grains from offshore Tano Basin, southwestern Ghana. Revista Espanola de Micropaleontologia, 36(3):451–465.

Aubry, M.-P., Ouda, K., Dupuis, C., Berggren, W.A., Van Couvering, J.A., and the Members of the Working Group on the Paleocene/Eocene Boundary, 2007. The Global Standard Stratotype-section and Point (GSSP) for the base of the Eocene Series in the Dababiya section (Egypt) Episodes, 30(4):271–286.

Awad, W.K., and Oboh-Ikuenobe, F.E., 2016. Early Paleogene dinoflagellate cysts from ODP Hole 959D, Côte d'Ivoire-Ghana Transform Margin, West Africa: new species, biostratigraphy and paleoenvironmental implications. Journal of African Earth Sciences, 123:123–144. **https://doi.org/10.1016/j.jafrearsci.2016.07.014**

Backman, J., 1980. Miocene-Pliocene nannofossils and sedimentation rates in the Hatton-Rockall Basin, NE Atlantic Ocean. Stockholm Contributions in Geology, 36:1–91.

Backman, J., 1986. Late Paleocene to middle Eocene calcareous nannofossil biochronology from the Shatsky Rise, Walvis Ridge and Italy. Palaeogeography, Palaeoclimatology, Palaeoecology, 57(1):43–59. **https://doi.org/10.1016/0031-0182(86)90005-2**

Backman, J., 1987. Quantitative calcareous nannofossil biochronology of middle Eocene through early Oligocene sediment from DSDP Sites 522 and 523. Abh. Geology, 39:21–31. **https://web.archive.org/web/20190430234835id_/https://www.zobodat.at/pdf/AbhGeolBA_39_0021-0032.pdf**

Backman, J., and Raffi, I., 1997. Calibration of Miocene nannofossil events to orbitally tuned cyclostratigraphies from Ceara Rise. In Shackleton, N.J., Curry, W.B., Richter, C., and Bralower, T.J. (Eds.), Proceedings of the Ocean Drilling Program, Scientific Results. 154: College Station, TX (Ocean Drilling Program), 83–99. **https://doi.org/10.2973/odp.proc.sr.154.101.1997**

Backman, J., Raffi, I., Rio, D., Fornaciari, E., and Pälike, H., 2012. Biozonation and biochronology of Miocene through Pleistocene calcareous nannofossils from low and middle latitudes. Newsletters on Stratigraphy, 45(3):221–244. **https://doi.org/10.1127/0078-0421/2012/0022**

Barron, J.A., Stickley, C.E., and Bukry, D., 2015. Paleoceanographic, and paleoclimatic constraints on the global Eocene diatom and silicoflagellate record. Palaeogeography, Palaeoclimatology, Palaeoecology, 422:85–100. **https://doi.org/10.1016/j.palaeo.2015.01.015**

Batiza, R., and White, J.D.L., 2000. Submarine lavas and hyaloclastite. In Sigurdsson, H., Encyclopedia of Volcanoes. San Diego, CA (Academic Press), 361–381.

Beddow, H.M., Liebrand, D., Wilson, D.S., Hilgen, F.J., Sluijs, A., Wade, B.S., and Lourens, L.J., 2018. Astronomical tunings of the Oligocene–Miocene transition from Pacific Ocean Site U1334 and implications for the carbon cycle. Climate of the Past, 14(3):255–270. **https://doi.org/10.5194/cp-14-255-2018**

Bell, J.S., and Gough, D.I., 1983. The use of borehole breakouts in the study of crustal stress. In Zoback, M.D. and Haimson, B.C., Hydraulic Fracturing Stress and Measurements. Washington, DC (National Academic Press), 201–209.

Berggren, W.A., Aubry, M.P., van Fossen, M., Kent, D.V., Norris, R.D., and Quillévéré, F., 2000. Integrated Paleocene calcareous plankton magnetobiochronology and stable isotope stratigraphy: DSDP Site 384 (NW Atlantic Ocean). Palaeogeography, Palaeoclimatology, Palaeoecology, 159(1):1–51. **https://doi.org/10.1016/S0031-0182(00)00031-6**

Berggren, W.A., Hilgen, F.J., Langereis, C.G., Kent, D.V., Obradovich, J.D., Raffi, I., Raymo, M.E., and Shackleton, N.J., 1995a. Late Neogene chronology: new perspectives in high-resolution stratigraphy. Geological Society of America Bulletin, 107(11):1272–1287. **https://doi.org/10.1130/0016-7606(1995)107<1272:LNCNPI>2.3.CO;2**

Berggren, W.A., Kent, D.V., Swisher, C.C., III, Aubry, M.-P., Berggren, W.A., Kent, D.V., Aubry, M.-P., and Hardenbol, J., 1995b. A revised Cenozoic geochronology and chronostratigraphy. In Berggren, W.A., Kent, D.V., Aubry, M.-P., and Hardenbol, J. (Eds.), Geochronology, Time Scales and Global Stratigraphic Correlation. SEPM Special Publication, 54. **https://doi.org/10.2110/pec.95.04.0129**

Berggren, W.A., and Pearson, P.N., 2005. A revised tropical to subtropical Paleogene planktonic foraminiferal zonation. Journal of Foraminiferal Research, 35(4):279–298. **https://doi.org/10.2113/35.4.279**

Bijl, P.K., 2022. DINOSTRAT: a global database of the stratigraphic and paleolatitudinal distribution of Mesozoic–Cenozoic organic-walled dinoflagellate cysts. Earth System Science Data, 14(2):579–617. **https://doi.org/10.5194/essd-14-579-2022**

Bijl, P.K., Brinkhuis, H., Egger, L.M., Eldrett, J.S., Frieling, J., Grothe, A., Houben, A.J.P., Pross, J., Śliwińska, K.K., and Sluijs, A., 2017. Comment on 'Wetzeliella and its allies – the 'hole' story: a taxonomic revision of the Paleogene dinoflagellate subfamily Wetzelielloideae' by Williams et al. (2015). Palynology, 41(3):423–429. **https://doi.org/10.1080/01916122.2016.1235056**

Bijl, P.K., Frieling, J., Cramwinckel, M.J., Boschman, C., Sluijs, A., and Peterse, F., 2021. Maastrichtian–Rupelian paleoclimates in the southwest Pacific – a critical re-evaluation of biomarker paleothermometry and dinoflagellate cyst paleoecology at Ocean Drilling Program Site 1172. Climate of the Past, 17(6):2393–2425. **https://doi.org/10.5194/cp-17-2393-2021**

Bijl, P.K., Houben, A.J.P., Bruls, A., Pross, J., and Sangiorgi, F., 2018. Stratigraphic calibration of Oligocene-Miocene organic-walled dinoflagellate cysts from offshore Wilkes Land, East Antarctica, and a zonation proposal. Journal of Micropalaeontology, 37(1):105–138. **https://doi.org/10.5194/jm-37-105-2018**

Bijl, P.K., Sluijs, A., and Brinkhuis, H., 2013. A magneto- and chemostratigraphically calibrated dinoflagellate cyst zonation of the early Palaeogene South Pacific Ocean. Earth-Science Reviews, 124:1–31. **https://doi.org/10.1016/j.earscirev.2013.04.010**

Blaj, T., Backman, J., and Raffi, I., 2009. Late Eocene to Oligocene preservation history and biochronology of calcareous nannofossils from paleoequatorial Pacific Ocean sediments. Rivista Italiana Di Paleontologia E Stratigrafia, 115(1):67–85. **https://doi.org/10.13130/2039-4942/5920**

Blum, P., 1997. Physical properties handbook: a guide to the shipboard measurement of physical properties of deep-sea cores. Ocean Drilling Program Technical Note, 26. **https://doi.org/10.2973/odp.tn.26.1997**

Bohaty, S.M., Uenzelmann-Neben, G., Childress, L.B., Archontikis, O.A., Batenburg, S.J., Bijl, P.K., Burkett, A.M., Cawthra, H.C., Chanda, P., Coenen, J.J., Dallanave, E., Davidson, P.C., Doiron, K.E., Geldmacher, J., Gürer, D., Haynes, S.J., Herrle, J.O., Ichiyama, Y., Jana, D., Jones, M.M., Kato, C., Kulhanek, D.K., Li, J., Liu, J., McManus, J., Minakov, A.N., Penman, D.E., Sprain, C.J., Tessin, A.C., Wagner, T., and Westerhold, T., 2023a. Site U1579. In Uenzelmann-Neben, G., Bohaty, S.M., Childress, L.B., and the Expedition 392 Scientists, Agulhas Plateau Cretaceous Climate. Proceedings of the International Ocean Discovery Program, 392: College Station, TX (International Ocean Discovery Program). **https://doi.org/10.14379/iodp.proc.392.103.2023**

Bohaty, S.M., Uenzelmann-Neben, G., Childress, L.B., Archontikis, O.A., Batenburg, S.J., Bijl, P.K., Burkett, A.M., Cawthra, H.C., Chanda, P., Coenen, J.J., Dallanave, E., Davidson, P.C., Doiron, K.E., Geldmacher, J., Gürer, D., Haynes, S.J., Herrle, J.O., Ichiyama, Y., Jana, D., Jones, M.M., Kato, C., Kulhanek, D.K., Li, J., Liu, J., McManus, J., Minakov, A.N., Penman, D.E., Sprain, C.J., Tessin, A.C., Wagner, T., and Westerhold, T., 2023b. Site U1580. In Uenzelmann-Neben, G., Bohaty, S.M., Childress, L.B., and the Expedition 392 Scientists, Agulhas Plateau Cretaceous Climate. Proceedings of the International Ocean Discovery Program, 392: College Station, TX (International Ocean Discovery Program). **https://doi.org/10.14379/iodp.proc.392.104.2023**

Bollmann, J., 1997. Morphology and biogeography of Gephyrocapsa coccoliths in Holocene sediments. Marine Micropaleontology, 29(3):319–350. **https://doi.org/10.1016/S0377-8398(96)00028-X**

Bown, P.R., 1998. Calcareous Nannofossil Biostratigraphy: Dordrect, Netherlands (Kluwer Academic Publishing).

Bown, P.R., 2005. Palaeogene calcareous microfossils from the Kilwa and Lindi areas of coastal Tanzania (Tanzania Drilling Project 2003–4). Journal of Nannoplankton Research, 27:21–95.

Bown, P.R., and Young, J.R., 1998. Techniques. In Bown, P.R., Calcareous Nannofossil Biostratigraphy. Dordrect, Netherlands (Kluwer Academic Publishing), 16–28.

Bralower, T.J., Fullagar, P.D., Paull, C.K., Dwyer, G.S., and Leckie, R.M., 1997. Mid-Cretaceous strontium-isotope stratigraphy of deep-sea sections. Geological Society of America Bulletin, 109(11):1421–1442. **https://doi.org/10.1130/0016-7606(1997)109<1421:MCSISO>2.3.CO;2**

Brinkhuis, H., Bujak, J.P., Smit, J., Versteegh, G.J.M., and Visscher, H., 1998. Dinoflagellate-based sea surface temperature reconstructions across the Cretaceous–Tertiary boundary. Palaeogeography, Palaeoclimatology, Palaeoecology, 141(1):67–83. **https://doi.org/10.1016/S0031-0182(98)00004-2**

Brinkhuis, H., Munsterman, D.K., Sengers, S., Sluijs, A., Warnaar, J., and Williams, G.L., 2004a. Late Eocene-Quaternary dinoflagellate cysts from ODP Site 1168, off western Tasmania. In Exon, N.F., Kennett, J.P., and Malone, M.J. (Eds.), Proceedings of the Ocean Drilling Program, Scientific Results. 189: College Station, TX (Ocean Drilling Program). **https://doi.org/10.2973/odp.proc.sr.189.105.2003**

Brinkhuis, H., Sengers, S., Sluijs, A., Warnaar, J., and Williams, G.L., 2004b. Latest Cretaceous-earliest Oligocene and Quaternary dinoflagellate cysts, ODP Site 1172, east Tasman Plateau. In Exon, N.F., Kennett, J.P., and Malone, M.J.

(Eds.), Proceedings of the Ocean Drilling Program, Scientific Results. 189: College Station, TX (Ocean Drilling Program). **https://doi.org/10.2973/odp.proc.sr.189.106.2003**

Bullard, E.C., 1954. The flow of heat through the floor of the Atlantic Ocean. Proceedings of the Royal Society of London, A: Mathematical and Physical Sciences, 222(1150):408–429. **https://doi.org/10.1098/rspa.1954.0085**

Burnett, J.A., 1998. Upper Cretaceous. In Bown, P.R., Calcareous Nannofossil Biostratigraphy. Dordrecht, The Netherlands (Kluwer Academic Publishing), 132–199.

Chaisson, W.P., and Pearson, P.N., 1997. Planktonic foraminifer biostratigraphy at Site 925: middle Miocene-Pleistocene. In Shackleton, N.J., Curry, W.B., Richter, C., and Bralower, T.J. (Eds.), Proceedings of the Ocean Drilling Program, Scientific Results. 154: College Station, TX (Ocean Drilling Program), 3–31. **https://doi.org/10.2973/odp.proc.sr.154.104.1997**

Chaproniere, G.C.H., Styzen, M.J., Sager, W.W., Nishi, H., Quinterno, P.J., and Abrahamsen, N., 1994. Late Neogene biostratigraphic and magnetostratigraphic synthesis, Leg 135. In Hawkins, J., Parson, L., Allan, J., et al., Proceedings of the Ocean Drilling Program, Scientific Results. 135: College Station, TX (Ocean Drilling Program), 857–877. **https://doi.org/10.2973/odp.proc.sr.135.116.1994**

Clague, D.A., Paduan, J.B., and Davis, A.S., 2009. Widespread strombolian eruptions of mid-ocean ridge basalt. Journal of Volcanology and Geothermal Research, 180(2–4):171–188. **https://doi.org/10.1016/j.jvolgeores.2008.08.007**

Cody, R.D., Levy, R.H., Harwood, D.M., and Sadler, P.M., 2008. Thinking outside the zone: high-resolution quantitative diatom biochronology for the Antarctic Neogene. Palaeogeography, Palaeoclimatology, Palaeoecology, 260(1–2):92–121. **https://doi.org/10.1016/j.palaeo.2007.08.020**

Constable, C., and Tauxe, L., 1990. The bootstrap for magnetic susceptibility tensors. Journal of Geophysical Research: Solid Earth, 95(B6):8383–8395. **https://doi.org/10.1029/JB095iB06p08383**

Contreras, L., Pross, J., Bijl, P.K., O'Hara, R.B., Raine, J.I., Sluijs, A., and Brinkhuis, H., 2014. Southern high-latitude terrestrial climate change during the Palaeocene–Eocene derived from a marine pollen record (ODP Site 1172, East Tasman Plateau). Climate of the Past, 10(4):1401–1420. **https://doi.org/10.5194/cp-10-1401-2014**

Costa, L.I., and Davey, R.J., 1992. Dinoflagellate cysts of the Cretaceous system. In Powell, A.J., A Stratigraphic Index of Dinoflagellate Cysts. Dordrecht, Netherlands (Springer), 99–154.

Crouch, E.M., Willumsen, P.S., Kulhanek, D.K., and Gibbs, S.J., 2014. A revised Paleocene (Teurian) dinoflagellate cyst zonation from eastern New Zealand. Review of Palaeobotany and Palynology, 202:47–79. **https://doi.org/10.1016/j.revpalbo.2013.12.004**

Crux, J.A., 1991. Calcareous nannofossils recovered by Leg 114 in the subantarctic South Atlantic Ocean. In Ciesielski, P.F., Kristoffersen, Y., et al., Proceedings of the Ocean Drilling Program, Scientific Results. 114: College Station, TX (Ocean Drilling Program), 155–177. **https://doi.org/10.2973/odp.proc.sr.114.123.1991**

de Vleeschouwer, D., Dunlea, A.G., Auer, G., Anderson, C.H., Brumsack, H., de Loach, A., Gurnis, M.C., Huh, Y., Ishiwa, T., Jang, K., Kominz, M.A., März, C., Schnetger, B., Murray, R.W., Pälike, H., and Expedition 356 Shipboard Scientists, 2017. Quantifying K, U, and Th contents of marine sediments using shipboard natural gamma radiation spectra measured on DV JOIDES Resolution. Geochemistry, Geophysics, Geosystems, 18(3):1053–1064. **https://doi.org/10.1002/2016GC006715**

Dixon, J.E., Stopler, E.M., and Holloway, J.R., 1995. An experimental study of water and carbon dioxide solubilities in mid-ocean ridge basaltic liquids, Part I: Calibration and solubility models. Journal of Petrology, 36(6):1607–1631. **https://doi.org/10.1093/oxfordjournals.petrology.a037267**

do Monte Guerra, R., Concheyro, A., Wise, S.W., Kender, S., and Fauth, G., 2016. New latitude-based nannofossil zonations for the Campanian–Maastrichtian of the South Atlantic Ocean and their paleoceanographic implications. Palaeogeography, Palaeoclimatology, Palaeoecology, 452:55–67. **https://doi.org/10.1016/j.palaeo.2016.04.010**

Dunham, R.J., 1962. Classification of carbonate rocks according to depositional texture. In Ham, W.E., Classification of Carbonate Rocks. AAPG Memoir, 1.

Dunlea, A.G., Murray, R.W., Harris, R.N., Vasiliev, M.A., Evans, H., Spivack, A.J., and D'Hondt, S., 2013. Assessment and use of NGR instrumentation on the JOIDES Resolution to quantify U, Th, and K concentrations in marine sediment. Scientific Drilling, 15:57–63. **https://doi.org/10.2204/iodp.sd.15.05.2013**

Egger, L.M., Sliwinska, K.K., van Peer, T.E., Liebrand, D., Lippert, P.C., Friedrich, O., Wilson, P.A., Norris, R.D., and Pross, J., 2016. Magnetostratigraphically-calibrated dinoflagellate cyst bioevents for the uppermost Eocene to lowermost Miocene of the western North Atlantic (IODP Expedition 342, Paleogene Newfoundland sediment drifts). Review of Palaeobotany and Palynology, 234:159–185. **https://doi.org/10.1016/j.revpalbo.2016.08.002**

Ellis, D.V., and Singer, J.M., 2007. Well Logging for Earth Scientists (2nd edition): New York (Elsevier). **https://doi.org/10.1007/978-1-4020-4602-5**

Embry, A.F., and Klovan, J.E., 1971. A late Devonian reef tract on northeastern Banks Island, N.W.T. Bulletin of Canadian Petroleum Geology, 19(4):730–781. **https://doi.org/10.35767/gscpgbull.19.4.730**

Esper, O., and Zonneveld, K.A.F., 2007. The potential of organic-walled dinoflagellate cysts for the reconstruction of past sea-surface conditions in the Southern Ocean. Marine Micropaleontology, 65(3–4):185–212. **https://doi.org/10.1016/j.marmicro.2007.07.002**

Expedition 320/321 Scientists, 2010. Methods. In Pälike, H., Lyle, M., Nishi, H., Raffi, I., Gamage, K., Klaus, A., and the Expedition 320/321 Scientists, Proceedings of the Integrated Ocean Drilling Program. 320/321: Tokyo (Integrated Ocean Drilling Program Management International, Inc.). **https://doi.org/10.2204/iodp.proc.320321.101.2010**

Expedition 324 Scientists, 2010. Methods. In Sager, W.W., Sano, T., Geldmacher, J., and the Expedition 324 Scientists, Proceedings of the Integrated Ocean Drilling Program. 324: Tokyo (Integrated Ocean Drilling Program Management International, Inc). **https://doi.org/10.2204/iodp.proc.324.102.2010**

Expedition 330 Scientists, 2012. Methods. In Koppers, A.A.P., Yamazaki, T., Geldmacher, J., and the Expedition 330 Scientists, Proceedings of the Integrated Ocean Drilling Program. 330: Tokyo (Integrated Ocean Drilling Program Management International, Inc.). **https://doi.org/10.2204/iodp.proc.330.102.2012**

Fensome, R.A., Taylor, F.J.R., Norris, G., Sarjeant, W.A.S., Wharton, D.I., and Williams, G.L., 1993. A classification of living and fossil dinoflagellates. Micropaleontology Special Paper.

Fisher, R.A., 1953. Dispersion on a sphere. Proceedings of the Royal Society A: Mathematical, Physical and Engineering Sciences, 217(1130):295–305. **https://doi.org/10.1098/rspa.1953.0064**

Florindo, F., Farmer, R.K., Harwood, D.M., Cody, R.D., Levy, R., Bohaty, S.M., Carter, L., and Winkler, A., 2013. Paleomagnetism and biostratigraphy of sediments from Southern Ocean ODP Site 744 (southern Kerguelen Plateau): implications for early-to-middle Miocene climate in Antarctica. Global and Planetary Change, 110(C):434–454. **https://doi.org/10.1016/j.gloplacha.2013.05.004**

Folk, R.L., 1962. Spectral subdivision of limestone types. In Ham, W.E., Classification of Carbonate Rocks. AAPG Memoir, 1: 62–84.

Fornaciari, E., 1996. Biocronologia a nannofossili calcarei e stratigrafia ad eventi nel Miocene italiano [PhD dissertation]. University of Padua, Padua, Italy.

Fornaciari, E., Di Stefano, A., Rio, D., and Negri, A., 1996. Middle Miocene quantitative calcareous nannofossil biostratigraphy in the Mediterranean region. Micropaleontology, 42(1):37–63. **https://doi.org/10.2307/1485982**

Forniaciari, E., Agnini, C., Catanzariti, R., Rio, D., Bolla, E.M., and Valvasoni, E., 2010. Mid-latitude calcareous nannofossil biostratigraphy and biochronology across the middle to late Eocene transition. Stratigraphy, 7(4):229–264. **https://www.micropress.org/microaccess/check/1717**

Frieling, J., and Sluijs, A., 2018. Towards quantitative environmental reconstructions from ancient non-analogue microfossil assemblages: ecological preferences of Paleocene–Eocene dinoflagellates. Earth-Science Reviews, 185:956–973. **https://doi.org/10.1016/j.earscirev.2018.08.014**

Gale, A.S., Bown, P., Caron, M., Crampton, J., Crowhurst, S.J., Kennedy, W.J., Petrizzo, M.R., and Wray, D.S., 2011. The uppermost middle and upper Albian succession at the Col de Palluel, Hautes-Alpes, France: an integrated study (ammonites, inoceramid bivalves, planktonic Foraminifera, nannofossils, geochemistry, stable oxygen and carbon isotopes, cyclostratigraphy). Cretaceous Research, 32(2):59–130. **https://doi.org/10.1016/j.cretres.2010.10.004**

Gale, A.S., Kennedy, W.J., Lees, J.A., Petrizzo, M.R., and Walaszczyk, I., 2007. An integrated study (inoceramid bivalves, ammonites, calcareous nannofossils, planktonic foraminifera, stable carbon isotopes) of the Ten Mile Creek section, Lancaster, Dallas County, north Texas, a candidate global boundary stratotype section and point for the base of the Santonian stage. Acta Geologica Polonica, 57(2):113–160.

Gartner, S., 1977. Calcareous nannofossil biostratigraphy and revised zonation of the Pleistocene. Marine Micropaleontology, 2:1–25. **https://doi.org/10.1016/0377-8398(77)90002-0**

Gartner, S., 1992. Miocene nannofossil chronology in the North Atlantic, DSDP Site 608. Marine Micropaleontology, 18(4):307–331. **https://doi.org/10.1016/0377-8398(92)90045-L**

Gee, J.S., Tauxe, L., and Constable, C., 2008. AMSSpin: a LabVIEW program for measuring the anisotropy of magnetic susceptibility with the Kappabridge KLY-4S. Geochemistry, Geophysics, Geosystems, 9(8):Q08Y02. **https://doi.org/10.1029/2008GC001976**

Gieskes, J.M., Gamo, T., and Brumsack, H.J., 1991. Chemical methods for interstitial water analysis aboard *JOIDES Resolution*. Ocean Drilling Program Technical Note, 15. **https://doi.org/10.2973/odp.tn.15.1991**

Gilmore, G.R., 2008. Practical Gamma-Ray Spectrometry, 2nd Edition: New York (Wiley). **https://doi.org/10.1002/9780470861981**

Godard, M., Awaji, S., Hansen, H., Hellebrand, E., Brunelli, D., Johnson, K., Yamasaki, T., Maeda, J., Abratis, M., Christie, D., Kato, Y., Mariet, C., and Rosner, M., 2009. Geochemistry of a long in-situ section of intrusive slow-spread oceanic lithosphere: results from IODP Site U1309 (Atlantis Massif, 30°N Mid-Atlantic-Ridge). Earth and Planetary Science Letters, 279(1–2):110–122. **https://doi.org/10.1016/j.epsl.2008.12.034**

Goldberg, D., 1997. The role of downhole measurements in marine geology and geophysics. Reviews of Geophysics, 35(3):315–342. **https://doi.org/10.1029/97RG00221**

Govindaraju, K., 1994. 1994 compilation of working values and sample description for 383 geostandards. Geostandards Newsletter, 18(S1):1–158. **https://doi.org/10.1046/j.1365-2494.1998.53202081.x-i1**

Gradstein, F.M., Ogg, J.G., Schmitz, M.D., and Ogg, G.M. (Eds.), 2012. The Geologic Time Scale 2012: Amsterdam (Elsevier). **https://doi.org/10.1016/C2011-1-08249-8**

Gradstein, F.M., Ogg, J.G., Schmitz, M.D., and Ogg, G.M. (Eds.), 2020. The Geologic Time Scale 2020: Amsterdam (Elsevier BV). **https://doi.org/10.1016/C2020-1-02369-3**

Greene, A.R., Scoates, J.S., Weis, D., Katvala, E.C., Israel, S., and Nixon, G.T., 2010. The architecture of oceanic plateaus revealed by the volcanic stratigraphy of the accreted Wrangellia oceanic plateau. Geosphere, 6(1):47–73. **https://doi.org/10.1130/GES00212.1**

Gregg, T.K.P., and Fink, J.H., 1995. Quantification of submarine lava-flow morphology through analog experiments. Geology, 23(1):73–76. **https://doi.org/10.1130/0091-7613(1995)023<0073:QOSLFM>2.3.CO;2**

Grippo, A., Fischer, A.G., Hinnov, L.A., Herbert, T.D., Premoli Silva, I., D'Argenio, B., Fischer, A.G., Premoli Silva, I., Weissert, H., and Ferreri, V., 2004. Cyclostratigraphy and Chronology of the Albian Stage (Piobbico Core, Italy). In D'Argenio, B., Fischer, A.G., Premoli Silva, I., Weissert, H., and Ferrerri, V. (Eds.), Cyclostratigraphy: Approaches and Case Histories. Special Publication - SEPM (Society for Sedimentary Geology), 81: 57–81. **https://doi.org/10.2110/pec.04.81.0057**

Hagelberg, T.K., Pisias, N.G., Shackleton, N.J., Mix, A.C., and Harris, S., 1995. Refinement of a high-resolution, continuous sedimentary section for studying equatorial Pacific Ocean paleoceanography, Leg 138. In Pisias, N.G., Mayer, L.A., Janecek, T.R., Palmer-Julson, A., and van Andel, T.H. (Eds.), Proceedings of the Ocean Drilling Program, Scientific Results. 138: College Station, TX (Ocean Drilling Program). **https://doi.org/10.2973/odp.proc.sr.138.103.1995**

Hajós, M., and Stradner, H., 1975. Late Cretaceous Archaeomonadaceae, Diatomaceae, and Silicoflagellatae from the South Pacific Ocean, Deep Sea Drilling Project, Leg 29, Site 275. In Kennett, J.P., Houtz, R. E., et al., Initial Reports

of the Deep Sea Drilling Project. 29: Washington, DC (US Government Printing Office), 913–1009. **https://doi.org/10.2973/dsdp.proc.29.126.1975**

Haldorsen, J.B.U., Johnson, D.L., Plona, T., Sinha, B., Valero, H., and Winkler, K., 2006. Borehole acoustic waves. Oilfield Review, 18(1):3443.

Hancock, H.J.L., Chaproniere, G.C., Dickens, G.R., and Henderson, R.A., 2002. Early Palaeogene planktic foraminiferal and carbon isotope stratigraphy, Hole 762C, Exmouth Plateau, northwest Australian margin. Journal of Micropalaeontology, 21(1):29–42. **https://doi.org/10.1144/jm.21.1.29**

Harwood, D.M., Feldmann, R.M., and Woodburne, M.O., 1988. Upper Cretaceous and lower Paleocene diatom and silicoflagellate biostratigraphy of Seymour Island, eastern Antarctic Peninsula. In Feldman, R.M., and Woodburne, M.O. (Eds.), Geology and Paleontology of Seymour Island Antarctic Peninsula. Geological Society of America Memoirs, 169. **https://doi.org/10.1130/MEM169-p55**

Harwood, D.M., and Maruyama, T., 1992. Middle Eocene to Pleistocene diatom biostratigraphy of Southern Ocean sediments from the Kerguelen Plateau, Leg 120. In Wise, S.W., Jr., Schlich, R., et al., Proceedings of the Ocean Drilling Program, Scientific Results. 120: College Station, TX (Ocean Drilling Program), 683–733. **https://doi.org/10.2973/odp.proc.sr.120.160.1992**

Helby, R.J., Morgan, R., and Partridge, A.D., 1987. A Palynological Zonation of the Australian Mesozoic. Memoir of the Association of Australasian Palaeontologists, 4. **http://pascal-francis.inist.fr/vibad/index.php?action=getRecordDetail&idt=7516487**

Hilgen, F.J., Krijgsman, W., Raffi, I., Turco, E., and Zachariasse, W.J., 2000. Integrated stratigraphy and astronomical calibration of the Serravallian/Tortonian boundary section at Monte Gibliscemi (Sicily, Italy). Marine Micropaleontology, 38(3–4):181–211. **https://doi.org/10.1016/S0377-8398(00)00008-6**

Horai, K., and Von Herzen, R.P., 1985. Measurement of heat flow on Leg 86 of the Deep Sea Drilling Project. In Heath, G.R., Burckle, L. H., et al., Initial Reports of the Deep Sea Drilling Project. 86: Washington, DC (US Government Printing Office), 759–777. **https://doi.org/10.2973/dsdp.proc.86.135.1985**

Hornibrook, N.B., Brazier, R.C., and Strong, C.P., 1989. Manual of New Zealand Permian to Pleistocene foraminiferal biostratigraphy. New Zealand Geological Survey Paleontological Bulletin, 56.

Huang, C., Hinnov, L., Fischer, A.G., Grippo, A., and Herbert, T., 2010. Astronomical tuning of the Aptian Stage from Italian reference sections. Geology, 38(10):899–902. **https://doi.org/10.1130/G31177.1**

Huber, B.T., 1991. Paleogene and early Neogene planktonic foraminifer biostratigraphy of Sites 738 and 744, Kerguelen Plateau (southern Indian Ocean). In Barron, J., Larsen, B., et al., Proceedings of the Ocean Drilling Program, Scientific Results. 119: College Station, TX (Ocean Drilling Program), 427–451. **https://doi.org/10.2973/odp.proc.sr.119.142.1991**

Huber, B.T., Hobbs, R.W., Bogus, K.A., Batenburg, S.J., Brumsack, H.-J., do Monte Guerra, R., Edgar, K.M., Edvardsen, T., Garcia Tejada, M.L., Harry, D.L., Hasegawa, T., Haynes, S.J., Jiang, T., Jones, M.M., Kuroda, J., Lee, E.Y., Li, Y.-X., MacLeod, K.G., Maritati, A., Martinez, M., O'Connor, L.K., Petrizzo, M.R., Quan, T.M., Richter, C., Riquier, L., Tagliaro, G.T., Wainman, C.C., Watkins, D.K., White, L.T., Wolfgring, E., and Xu, Z., 2019a. Expedition 369 methods. In Hobbs, R.W., Huber, B.T., Bogus, K.A., and the Expedition 369 Scientists, Australia Cretaceous climate and tectonics. Proceedings of the International Ocean Discovery Program, 369: College Station, TX (International Ocean Discovery Program). **https://doi.org/10.14379/iodp.proc.369.102.2019**

Huber, B.T., Hobbs, R.W., Bogus, K.A., Batenburg, S.J., Brumsack, H.-J., do Monte Guerra, R., Edgar, K.M., Edvardsen, T., Garcia Tejada, M.L., Harry, D.L., Hasegawa, T., Haynes, S.J., Jiang, T., Jones, M.M., Kuroda, J., Lee, E.Y., Li, Y.-X., MacLeod, K.G., Maritati, A., Martinez, M., O'Connor, L.K., Petrizzo, M.R., Quan, T.M., Richter, C., Riquier, L., Tagliaro, G.T., Wainman, C.C., Watkins, D.K., White, L.T., Wolfgring, E., and Xu, Z., 2019b. Expedition 369 summary. In Hobbs, R.W., Huber, B.T., Bogus, K.A., and the Expedition 369 Scientists, Australia Cretaceous climate and tectonics. Proceedings of the International Ocean Discovery Program, 369: College Station, TX (International Ocean Discovery Program). **https://doi.org/10.14379/iodp.proc.369.101.2019**

Huber, B.T., and Leckie, R.M., 2011. Planktic foraminiferal species turnover across deep-sea Aptian/Albian boundary sections. Journal of Foraminiferal Research, 41(1):53–95. **https://doi.org/10.2113/gsjfr.41.1.53**

Huber, B.T., MacLeod, K.G., and Tur, N.A., 2008. Chronostratigraphic framework for upper Campanian-Maastrichtian sediments on the Blake Nose (subtropical North Atlantic). Journal of Foraminiferal Research, 38(2):162–182. **https://doi.org/10.2113/gsjfr.38.2.162**

Huber, B.T., MacLeod, K.G., Watkins, D.K., and Coffin, M.F., 2018. The rise and fall of the Cretaceous hot greenhouse climate. Global and Planetary Change, 167:1–23. **https://doi.org/10.1016/j.gloplacha.2018.04.004**

Huber, B.T., Petrizzo, M.R., and Falzoni, F., 2022. Taxonomy and phylogeny of Albian–Maastrichtian planispiral planktonic foraminifera traditionally assigned to Globigerinelloides. Micropaleontology, 68(2):117–183.

Ingle, J.C., Jr., 1980. Cenozoic paleobathymetry and depositional history of selected sequences within the southern California continental borderland. In Sliter, W.V., Studies in Marine Micropaleontology and Paleoecology: A Memorial Volume to Orville L. Bandy. Cushman Special Publications, 19.

Iturrino, G., Liu, T., Goldberg, D., Anderson, L., Evans, H., Fehr, A., Guerin, G., Inwood, J., Lofi, J., Malinverno, A., Morgan, S., Mrozewski, S., Slagle, A., and Williams, T., 2013. Performance of the wireline heave compensation system onboard D/V JOIDES Resolution. Scientific Drilling, 15:46–50. **https://doi.org/10.2204/iodp.sd.15.08.2013**

Jelinek, V., 1981. Characterization of the magnetic fabric of rocks. Tectonophysics, 79(3–4):T63–T67. **https://doi.org/10.1016/0040-1951(81)90110-4**

Jerram, D.A., and Widdowson, M., 2005. The anatomy of continental flood basalt provinces: geological constraints on the processes and products of flood volcanism. Lithos, 79(3–4):385–405. **https://doi.org/10.1016/j.lithos.2004.09.009**

Jochum, K.P., Nohl, U., Herwig, K., Lammel, E., Stoll, B., and Hofmann, A.W., 2005. GeoReM: a new geochemical database for reference materials and isotopic standards. Geostandards and Geoanalytical Research, 29(3):333–338. **https://doi.org/10.1111/j.1751-908X.2005.tb00904.x**

Johnston, R.M., Ryan, J.G., Fryer, P., Wheat, C.G., Williams, T., Albers, E., Bekins, B.A., Debret, B.P.R., Jianghong, D., Yanhui, D., Eickenbusch, P., Frery, E.A., Ichiyama, Y., Johnson, K., Kevorkian, R.T., Kurz, W., Magalhaes, V., Mantovanelli, S.S., Menapace, W., Menzies, C.D., Michibayashi, K., Moyer, C.L., Mullane, K.K., Park, J.-W., Price, R.E., Shervais, J.W., Suzuki, S., Sissmann, O.J., Takai, K., Walter, B., and Rui, Z., 2018. pXRF and ICP-AES characterization of shipboard rocks and sediments; protocols and strategies. In Mariana Convergent Margin and South Chamorro Seamount. Proceedings of the International Ocean Discovery Program, 366: (Proceedings of the International Ocean Discovery Program). **https://doi.org/10.14379/iodp.proc.366.110.2018**

Jones, R.W., and Brady, H.B., 1994. The Challenger Foraminifera: Oxford, UK (Oxford University Press).

Kaminski, M., and Gradstein, F., 2005. Atlas of Paleogene Cosmopolitan Deep-Water Agglutinated Foraminifera: New York (Grzybowski Foundation). **https://foraminifera.eu/atlas.html**

Kanungo, S., 2005. Biostratigraphy and palaeoceanography of mid-Cretacous calcareous nannofossils: studies from the Cauvery Basin, SE India; the Anglo-Paris Basin, SE England; North Atlantic and Pacific Ocean [PhD dissertation]. University College, London, UK.

Keil, R.G., Hu, F.S., Tsamakis, E.C., and Hedges, J.I., 1994. Pollen in marine sediments as an indicator of oxidation of organic matter. Nature, 369(6482):639–641. **https://doi.org/10.1038/369639a0**

Kirschvink, J.L., 1980. The least-squares line and plane and the analysis of palaeomagnetic data. Geophysical Journal International, 62(3):699–718. **https://doi.org/10.1111/j.1365-246X.1980.tb02601.x**

Kokelaar, B.P., 1982. Fluidization of wet sediments during the emplacement and cooling of various igneous bodies. Journal of the Geological Society, 139(1):21–33. **https://doi.org/10.1144/gsjgs.139.1.0021**

Koppers, A.A.P., Yamazaki, T., Geldmacher, J., and the Expedition 330 Scientific Party, 2013. IODP Expedition 330: drilling the Louisville Seamount Trail in the SW Pacific. Scientific Drilling, 15:11–22. **https://doi.org/10.2204/iodp.sd.15.02.2013**

Köthe, A., 2012. A revised Cenozoic dinoflagellate cyst and calcareous nannoplankton zonation for the German sector of the southeastern North Sea Basin. Newsletters on Stratigraphy, 45(3):189–220. **https://doi.org/10.1127/0078-0421/2012/0021**

Kristiansen, J.I., 1982. The transient cylindrical probe method for determination of thermal parameters of earth materials [PhD dissertation]. Åarhus University, Åarhus, Denmark. **http://digitallib.oit.edu/digital/collection/geoheat/id/2103/**

Kuhlmann, G., Langereis, C.G., Munsterman, D., van Leeuwen, R.J., Verreussel, R., Meulenkamp, J.E., and Wong, T.E., 2006. Integrated chronostratigraphy of the Pliocene-Pleistocene interval and its relation to the regional stratigraphical stages in the southern North Sea region. Geologie en Mijnbouw, 85(1):19–35. **https://doi.org/10.1017/S0016774600021405**

Li, C.-F., Lin, J., Kulhanek, D.K., Williams, T., Bao, R., Briais, A., Brown, E.A., Chen, Y., Clift, P.D., Colwell, F.S., Dadd, K.A., Ding, W., Almeida, I.H., Huang, X.-L., Hyun, S., Jiang, T., Koppers, A.A.P., Li, Q., Liu, C., Liu, Q., Liu, Z., Nagai, R.H., Peleo-Alampay, A., Su, X., Sun, Z., Tejada, M.L.G., Trinh, H.S., Yeh, Y.-C., Zhang, C., Zhang, F., Zhang, G.-L., and Zhao, X, 2015. Methods. In Li, C.-F., Lin, J., Kulhanek, D.K., and the Expedition 349 Scientists, South China Sea Tectonics. Proceedings of the International Ocean Discovery Program, 349: College Station, TX (International Ocean Discovery Program). **https://doi.org/10.14379/iodp.proc.349.102.2015**

Liebrand, D., Beddow, H.M., Lourens, L.J., Pälike, H., Raffi, I., Bohaty, S.M., Hilgen, F.J., Saes, M.J.M., Wilson, P.A., van Dijk, A.E., Hodell, D.A., Kroon, D., Huck, C.E., and Batenburg, S.J., 2016. Cyclostratigraphy and eccentricity tuning of the early Oligocene through early Miocene (30.1–17.1 Ma): Cibicides mundulus stable oxygen and carbon isotope records from Walvis Ridge Site 1264. Earth and Planetary Science Letters, 450:392–405. **https://doi.org/10.1016/j.epsl.2016.06.007**

Liu, T., Iturrino, G., Goldberg, D., Meissner, E., Swain, K., Furman, C., Fitzgerald, P., Frisbee, N., Chlimoun, J., Van Hyfte, J., and Beyer, R., 2013. Performance evaluation of active wireline heave compensation systems in marine well logging environments. Geo-Marine Letters, 33(1):83–93. **https://doi.org/10.1007/s00367-012-0309-8**

Loeblich, A.R., and Tappan, H.N., 1988. Foraminiferal Genera and Their Classification: Plates: (Van Nostrand Reinhold Company).

Lonsdale, P., and Spiess, F.N., 1980. Deep-tow observations at the East Pacific Rise, 8°45′N, and some interpretations. In Rosendahl, B.R., Hekinian, R., et al., Initial Reports of the Deep Sea Drilling Project. 54: Washington, DC (US Government Printing Office), 43–62. **https://doi.org/10.2973/dsdp.proc.54.104.1980**

Lourens, L., Hilgen, F., Shackleton, N.J., Laskar, J., and Wilson, D., 2005. The Neogene period. In Smith, A.G., Gradstein, F.M. and Ogg, J.G., A Geologic Time Scale 2004. Cambridge, UK (Cambridge University Press), 409–440. **https://doi.org/10.1017/CBO9780511536045.022**

Lovell, M.A., Harvey, P.K., Brewer, T.S., Williams, C., Jackson, P.D., and Williamson, G., 1998. Application of FMS images in the Ocean Drilling Program: an overview. Geological Society Special Publication, 131:287–303. **https://doi.org/10.1144/GSL.SP.1998.131.01.18**

Lurcock, P.C., and Wilson, G.S., 2012. PuffinPlot: a versatile, user-friendly program for paleomagnetic analysis. Geochemistry, Geophysics, Geosystems, 13(6):Q06Z45. **https://doi.org/10.1029/2012GC004098**

Luthi, S.M., 1990. Sedimentary structures of clastic rocks identified from electrical borehole images. In Hurst, A., Lovell, M.A., and Morton, A.C., Geological Applications of Wireline Logs. Geological Society Special Publication, 48: 3–10. **https://doi.org/10.1144/GSL.SP.1990.048.01.02**

Luyendyk, B.P., and Davies, T.A., 1974. Introduction and principal results; Leg 26 Deep Sea Drilling Project. In Davies, T.A., Luyendyk, B.P., et al., Initial Reports of the Deep Sea Drilling Project. 26: Washington, DC (US Government Printing Office), 5–9. **https://doi.org/10.2973/dsdp.proc.26.101.1974**

MacKenzie, W.S., Donaldson, C.H., and Guilford, C., 1982. Atlas of Igneous Rocks and Their Textures: Essex, UK (Longman Group UK Limited).

Maiorano, P., and Marino, M., 2004. Calcareous nannofossil bioevents and environmental control on temporal and spatial patterns at the early-middle Pleistocene. Marine Micropaleontology, 53(3):405–422. **https://doi.org/10.1016/j.marmicro.2004.08.003**

Maltman, A., 1994. Deformation structures preserved in rocks. In Maltman, A., The Geological Deformation of Sediments. Dordrecht (Springer Netherlands), 261–307. **https://doi.org/10.1007/978-94-011-0731-0_9**

Manheim, F.T., 1966. A hydraulic squeezer for obtaining interstitial waters from consolidated and unconsolidated sediments. US Geological Survey Professional Paper, 550-C:256–261.

Mao, S., and Mohr, B.A.R., 1992. Late Cretaceous dinoflagellate cysts (?Santonian-Maestrichtian) from the southern Indian Ocean (Hole 748C). In Wise, S.W., Jr., Schlich, R., et al., Proceedings of the Ocean Drilling Program, Scientific Results. 120: College Station, TX (Ocean Drilling Program), 307–341. **https://doi.org/10.2973/odp.proc.sr.120.190.1992**

Martini, E., 1971. Standard Tertiary and Quaternary calcareous nannoplankton zonation. Proceedings of the Second Planktonic Conference, Roma, 1970:739–785.

Masure, E., Rauscher, R., Dejax, J., Schuler, M., and Ferré, B., 1998. Cretaceous-Paleocene palynology from the Côte d'Ivoire-Ghana transform margin, Sites 959, 960, 961, and 962. In Mascle, J., Lohmann, G.P., and Moullade, M. (Eds.), Proceedings of the Ocean Drilling Program, Scientific Results. 159: College Station, TX (Ocean Drilling Program), 253–276. **https://doi.org/10.2973/odp.proc.sr.159.040.1998**

Matsuoka, H., and Okada, H., 1990. Time-progressive morphometric changes of the genus Gephyrocapsa in the Quaternary sequence of the tropical Indian Ocean, Site 709. Proceedings of the Ocean Drilling Program, Scientific Results, 115:255–270. **https://doi.org/10.2973/odp.proc.sr.115.155.1990**

Mazzullo, J., Meyer, A., and Kidd, R., 1988. Appendix I: New sediment classification scheme for the Ocean Drilling Program. In Mazzullo, J., and Graham, A.G. , Handbook for shipboard sedimentologists. Ocean Drilling Program Technical Note. 8: 44–67. **https://doi.org/10.2973/odp.tn.8.1988**

Miller, K.G., Aubry, M.-P., Khan, M.J., Melillo, A.J., Kent, D.V., and Berggren, W.A., 1985. Oligocene-Miocene biostratigraphy, magnetostratigraphy, and isotopic stratigraphy of the western North Atlantic. Geology, 13(4):257–261. **https://doi.org/10.1130/0091-7613(1985)13<257:OBMAIS>2.0.CO;2**

Mitchell, N., Beier, C., Rosin, P., Quartau, R., and Tempera, F., 2008. Lava penetrating water: submarine lava flows around the coasts of Pico Island, Azores. Geochemistry Geophysics Geosystems, 9:Q03024. **https://doi.org/10.1029/2007GC001725**

Mix, A.C., Le, J., and Shackleton, N.J., 1995. Benthic foraminiferal stable isotope stratigraphy of Site 846: 0–1.8 Ma. In Pisias, N.G., Mayer, L.A., Janecek, T.R., Palmer-Julson, A., and van Andel, T.H. (Eds.), Proceedings of the Ocean Drilling Program, Scientific Results. 138: College Station, TX (Ocean Drilling Program), 839–854. **https://doi.org/10.2973/odp.proc.sr.138.160.1995**

Mohr, B.A.R., and Mao, S., 1997. Maastrichtian dinocyst floras from Maud Rise and Georgia Basin (Southern Ocean): their stratigraphic and paleoenvironmental implications. Palynology, 21(1):41–65. **https://doi.org/10.1080/01916122.1997.9989486**

Morgan, R., 1978. Albian to Senonian palynology of Site 364, Angola Basin. In Bolli, H.M., Ryan, W.B.F., et al., Initial Reports of the Deep Sea Drilling Project. 40: Washington, DC (US Government Printing Office), 915–951. **https://doi.org/10.2973/dsdp.proc.40.126.1978**

Morris, A., Gee, J.S., Pressling, N., John, B.E., MacLeod, C.J., Grimes, C.B., and Searle, R.C., 2009. Footwall rotation in an oceanic core complex quantified using reoriented Integrated Ocean Drilling Program core samples. Earth and Planetary Science Letters, 287(1–2):217–228. **https://doi.org/10.1016/j.epsl.2009.08.007**

Murray, R.W., Miller, D.J., and Kryc, K.A., 2000. Analysis of major and trace elements in rocks, sediments, and interstitial waters by inductively coupled plasma–atomic emission spectrometry (ICP-AES). Ocean Drilling Program Technical Note, 29. **https://doi.org/10.2973/odp.tn.29.2000**

Ogg, J.G., 2020. Geomagnetic Polarity Time Scale. In Gradstein, F.M., Ogg, J.G., Schmitz, M., and Ogg, G. (Eds.), Geologic Time Scale 2020. Amsterdam (Elsevier), 159–192. **https://doi.org/10.1016/B978-0-12-824360-2.00005-X**

Olsson, R.K., Berggren, W.A., Hemleben, C., and Huber, B.T., 1999. Atlas of Paleocene Planktonic Foraminifera: Washington, DC (Smithsonian Institution Press). **https://doi.org/10.5479/si.00810266.85.1**

Paillet, F.L., and Kim, K., 1987. Character and distribution of borehole breakouts and their relationship to in situ stresses in deep Columbia River basalts. Journal of Geophysical Research: Solid Earth, 92(B7):6223–6234. **https://doi.org/10.1029/JB092iB07p06223**

Passchier, C.W., and Trouw, R.A.J., 1996. Microtectonics: Berlin (Springer-Verlag).

Payros, A., Orue-Etxebarria, X., Bernaola, G., Apellaniz, E., Dinars-Turell, J., Tosquella, J., and Caballero, F., 2009. Characterization and astronomically calibrated age of the first occurrence of Turborotalia frontosa in the Gorrondatxe section, a prospective Lutetian GSSP: implications for the Eocene time scale. Lethaia, 42(3):255-264. **https://doi.org/10.1111/j.1502-3931.2008.00142.x**

Pearce, M.A., 2000. Palynology and chemostratigraphy of the Cenomanian to lower Campanian chalk of southern and eastern England [PhD dissertation]. Kingston University, London. **https://eprints.kingston.ac.uk/id/eprint/20657/**

Pearce, M.A., Jarvis, I., Ball, P.J., and Laurin, J., 2020. Palynology of the Cenomanian to lowermost Campanian (Upper Cretaceous) Chalk of the Trunch Borehole (Norfolk, UK) and a new dinoflagellate cyst bioevent stratigraphy for NW Europe. Review of Palaeobotany and Palynology, 278:104188. **https://doi.org/10.1016/j.revpalbo.2020.104188**

Pearson, P.N., 1995. Planktonic foraminifer biostratigraphy and the development of pelagic caps on guyots in the Marshall Islands group. In Haggerty, J.A., Premoli Suva, L, Rack, R, and McNutt, M.K. (Eds.), Proceedings of the Ocean

Drilling Program, Scientific Results. 144: College Station, TX (Ocean Drilling Program), 21–59. **https://doi.org/10.2973/odp.proc.sr.144.013.1995**

Pearson, P.N., and Chaisson, W.P., 1997. Late Paleocene to Middle Miocene planktonic foraminifer biostratigraphy of the Ceara Rise. In Shackleton, N.J., Curry, W.B., Richter, C., and Bralower, T.J. (Eds.), Proceedings of the Ocean Drilling Program, Scientific Results. 154: College Station, TX (Ocean Drilling Program), 33–68. **https://doi.org/10.2973/odp.proc.sr.154.106.1997**

Pearson, P.N., Nicholas, C.J., Singano, J.M., Bown, P.R., Coxall, H.K., van Dongen, B.E., Huber, B.T., Karega, A., Lees, J.A., Msaky, E., Pancost, R.D., Pearson, M., and Roberts, A.P., 2004. Paleogene and Cretaceous sediment cores from the Kilwa and Lindi areas of coastal Tanzania: Tanzania Drilling Project Sites 1–5. Journal of African Earth Sciences, 39(1–2):25–62. **https://doi.org/10.1016/j.jafrearsci.2004.05.001**

Pearson, P.N., Olsson, R.K., Huber, B.T., Hemleben, C., and Berggren, W.A., 2006. Atlas of Eocene planktonic foraminifera. Special Publication - Cushman Foundation for Foraminiferal Research, 41.

Perch-Nielsen, K., 1985a. Cenozoic calcareous nannofossils. In Bolli, H.M., Saunders, J.B., and Perch-Nielsen, K. (Eds.), Plankton Stratigraphy (Volume 1). Cambridge, UK (Cambridge University Press), 427–554.

Perch-Nielsen, K., 1985b. Mesozoic calcareous nannofossils. In Bolli, H.M., Saunders, J.B., and Perch-Nielsen, K., Plankton Stratigraphy (Volume 1). Cambridge, UK (Cambridge University Press), 329–426.

Petrizzo, M.R., Falzoni, F., and Silva, I.P., 2011. Identification of the base of the lower-to-middle Campanian Globotruncana ventricosa zone: comments on reliability and global correlations. Cretaceous Research, 32(3):387–405. **https://doi.org/10.1016/j.cretres.2011.01.010**

Petrizzo, M.R., MacLeod, K.G., Watkins, D.K., Wolfgring, E., and Huber, B.T., 2022. Late Cretaceous paleoceanographic evolution and the onset of cooling in the Santonian at southern high latitudes (IODP Site U1513, SE Indian Ocean). Paleoceanography and Paleoclimatology, 37(1):e2021PA004353. **https://doi.org/10.1029/2021PA004353**

Pettijohn, F.J., and Siever, R., 1987. Sand and Sandstone: New York (Springer-Verlag). **https://doi.org/10.1007/978-1-4612-1066-5**

Piasecki, S., Larsen, L.M., Pedersen, A.K., and Pedersen, G.K., 1992. Palynostratigraphy of the lower Tertiary volcanics and marine clastic sediments in the southern part of the West Greenland Basin: implications for the timing and duration of the volcanism. Rapport Grønlands Geologiske Undersøgelse, 154:13–31. **https://doi.org/10.34194/rapggu.v154.8166**

Poore, R.Z., Tauxe, L., Percival, S.F., Jr., and LaBrecque, J.L., 1982. Late Eocene–Oligocene magnetostratigraphy and biostratigraphy at South Atlantic DSDP Site 522. Geology, 10(10):508–511. **https://doi.org/10.1130/0091-7613(1982)10<508:LEMABA>2.0.CO;2**

Pospichal, J.J., and Wise, S.W., Jr., 1990. Maestrichtian calcareous nannofossil biostratigraphy of Maud Rise, ODP Leg 113 Sites 689 and 690, Weddell Sea. In Barker, P.F., Kennett, J. P., et al., Proceedings of the Ocean Drilling Program, Scientific Results. 113: College Station, TX (Ocean Drilling Program), 465–487. **https://doi.org/10.2973/odp.proc.sr.113.124.1990**

Powell, A.J., 1992. Dinoflagellate cysts of the Tertiary System. In Powell, A.J., A Stratigraphix Index of Dinoflagellate Cysts. British Micropaleontological Society Publication.

Prebble, J.G., Crouch, E.M., Carter, L., Cortese, G., Bostock, H., and Neil, H., 2013. An expanded modern dinoflagellate cyst dataset for the Southwest Pacific and Southern Hemisphere with environmental associations. Marine Micropaleontology, 101:33–48. **https://doi.org/10.1016/j.marmicro.2013.04.004**

Premoli Silva, I., Orlando, M., Monechi, S., Madile, M., Napoleone, G., and Ripepe, M., 1987. Calcareous plankton biostratigraphy and magnetostratigraphy at the Eocene-Oligocene transition in the Gubbio area. Presented at the International Subcommittee on Paleogene Stratigraphy Eocene/OIigocene Meeting, Ancona, Italy, October 1987.

Pribnow, D.F.C., Kinoshita, M., and Stein, C.A., 2000. Thermal data collection and heat flow recalculations for ODP Legs 101-180: Hannover, Germany (Institute for Joint Geoscientific Research). **http://www-odp.tamu.edu/publications/heatflow/**

Prince, I.M., Jarvis, I., Pearce, M.A., and Tocher, B.A., 2008. Dinoflagellate cyst biostratigraphy of the Coniacian–Santonian (Upper Cretaceous): new data from the English chalk. Review of Palaeobotany and Palynology, 150(1–4):59–96. **https://doi.org/10.1016/j.revpalbo.2008.01.005**

Pujol, C., and Duprat, J., 1983. Quaternary planktonic foraminifers of the southwestern Atlantic (Rio Grande Rise): Deep Sea Drilling Project Leg 72. In Barker, P.F., Carlson, R. L., Johnson, D. A., et al., Initial Reports of the Deep Sea Drilling Project. 72: Washington, DC (US Government Printing Office), 601–622. **https://doi.org/10.2973/dsdp.proc.72.128.1983**

R Core Team, 2018. R: A language and environment for statistical computing. R Foundation for Statistical Computing. **https://www.r-project.org/**

Raffi, I., 1999. Precision and accuracy of nannofossil biostratigraphic correlation. Philosophical Transactions of the Royal Society of London A, Mathematical and Physical Sciences, 357(1757):1975–1993. **https://doi.org/10.1098/rsta.1999.0410**

Raffi, I., 2002. Revision of the Early-Middle Pleistocene calcareous nannofossil biochronology (1.75–0.85 Ma). Marine Micropaleontology, 45(1):25–55. **https://doi.org/10.1016/S0377-8398(01)00044-5**

Raffi, I., Backman, J., Fornaciari, E., Pälike, H., Rio, D., Lourens, L., and Hilgen, F., 2006. A review of calcareous nannofossil astrobiochronology encompassing the past 25 million years. Quaternary Science Reviews, 25(23):3113–3137. **https://doi.org/10.1016/j.quascirev.2006.07.007**

Raffi, I., Backman, J., Rio, D., and Shackleton, N.J., 1993. Plio-Pleistocene nannofossil biostratigraphy and calibration to oxygen isotope stratigraphies from Deep Sea Drilling Project Site 607 and Ocean Drilling Program Site 677. Paleoceanography and Paleoclimatology, 8(3):387–408. **https://doi.org/10.1029/93PA00755**

Raffi, I., and Flores, J.-A., 1995. Pleistocene through Miocene calcareous nannofossils from eastern equatorial Pacific Ocean (Leg 138). In Pisias, N.G., Mayer, L.A., Janecek, T.R., Palmer-Julson, A., and van Andel, T.H. (Eds.), Proceed-

ings of the Ocean Drilling Program, Scientific Results. 138: College Station, TX (Ocean Drilling Program), 233–286. **https://doi.org/10.2973/odp.proc.sr.138.112.1995**

Raffi, I., Mozzato, C., Fornaciari, E., Hilgen, F.J., and Rio, D., 2003. Late Miocene calcareous nannofossil biostratigraphy and astrobiochronology for the Mediterranean region. Micropaleontology, 49(1):1–26. **https://doi.org/10.2113/49.1.1**

Raffi, I., Rio, D., d'Atri, A., Fornaciari, E., and Rocchetti, S., 1995. Quantitative distribution patterns and biomagnetostratigraphy of middle and late Miocene calcareous nannofossils from equatorial Indian and Pacific oceans (Legs 115, 130, and 138). In Pisias, N.G., Mayer, L.A., Janecek, T.R., Palmer-Julson, A., and van Andel, T.H. (Eds.), Proceedings of the Ocean Drilling Program, Scientific Results. 138: College Station, TX (Ocean Drilling Program), 479–502. **https://doi.org/10.2973/odp.proc.sr.138.125.1995**

Ramsay, J.G., and Huber, M.I., 1987. The Techniques of Modern Structural Geology: Folds and Fractures: Cambridge, MA (Academic Press).

Reagan, M.K., Pearce, J.A., Petronotis, K., Almeev, R., Avery, A.A., Carvallo, C., Chapman, T., Christeson, G.L., Ferré, E.C., Godard, M., Heaton, D.E., Kirchenbaur, M., Kurz, W., Kutterolf, S., Li, H.Y., Li, Y., Michibayashi, K., Morgan, S., Nelson, W.R., Prytulak, J., Python, M., Robertson, A.H.F., Ryan, J.G., Sager, W.W., Sakuyama, T., Shervais, J.W., Shimizu, K., and Whattam, S.A., 2015. Expedition 352 methods. In Reagan, M.K., Pearce, J.A., Petronotis, K., and the Expedition 352 Scientists, Izu-Bonin-Mariana Fore Arc. Proceedings of the International Ocean Discovery Program, 352: College Station, TX (International Ocean Discovery Program). **https://doi.org/10.14379/iodp.proc.352.102.2015**

Renaudie, J., Drews, E.L., and Böhne, S., 2018. The Paleocene record of marine diatoms in deep-sea sediments. Fossil Record, 21(2):183–205. **https://doi.org/10.5194/fr-21-183-2018**

Reynolds, R.C., Jr., 1963. Matrix corrections in trace element analysis by X-ray fluorescence: estimation of the mass absorption coefficient by Compton scattering. American Mineralogist, 48(9–10):1133–1143. **http://www.minsocam.org/ammin/AM48/AM48_1133.pdf**

Rider, M.H., 1996. The Geological Interpretation of Well Logs (Second edition): Houston, TX (Gulf Publishing Company).

Rio, D., 1982. The fossil distribution of coccolithophore genus Gephyrocapsa Kamptner and related Plio-Pleistocene chronostratigraphic problems. In Prell, W.L., Gardner, J. V., et al., Initial Reports of the Deep Sea Drilling Project. 68: Washington, DC (US Government Printing Office), 325–343. **https://doi.org/10.2973/dsdp.proc.68.109.1982**

Rio, D., Raffi, I., and Villa, G., 1990. Pliocene-Pleistocene calcareous nannofossil distribution patterns in the western Mediterranean. In Kastens, K.A., Mascle, J., et al., Proceedings of the Ocean Drilling Program, Scientific Results. 107: College Station, TX (Ocean Drilling Program), 513–533. **https://doi.org/10.2973/odp.proc.sr.107.164.1990**

Robaszynski, F., 1998. Planktonic foraminifera column. In de Graciansky, P.-C., Hardenbol, J., Jacquin, T., and Vail, P.R. (Eds.), Mesozoic-Cenozoic Sequence Stratigraphy of European Basins. Special Publication - SEPM (Society for Sedimentary Geology), 60.

Ruddiman, W.F., Kidd, R.B., Baldauf, J.G., Clement, B.M., Dolan, J.F., Eggers, M.R., Hill, P.R., Keigwin, L.D., Jr., Mitchell, M., Philipps, I., Robinson, F., Salehipour, S.A., Takayama, T., Thomas, E., Unsold, G., and Weaver, P.P.E., 1987. Initial Reports of the Deep Sea Drilling Project, 94: College Station, TX (Ocean Drilling Program). **https://doi.org/10.2973/dsdp.proc.94.1987**

Sager, W., Hoernle, K., Höfig, T.W., Avery, A.J., Bhutani, R., Carvallo, C.A., Class, C., Dai, Y., Dalla Valle, G., Del Gaudio, A.V., Fielding, S., Gaastra, K.M., Han, S., Heaton, D., Homrighausen, S., Kubota, Y., Li, C.-F., Nelson, W.R., Petrou, E., Potter, K.E., Pujatti, S., Scholpp, J., Shervais, J.W., Thoram, S., Tikoo-Schantz, S.M., Tshiningayamwe, M., Wang, X.-J., and Widdowson, M., 2023. Expedition 391 methods. In Sager, W., Hoernle, K., Höfig, T.W., and the Expedition 391 Scientists, Walvis Ridge Hotspot. Proceedings of the International Ocean Discovery Program, 391: College Station, TX (International Ocean Discovery Program). **https://doi.org/10.14379/iodp.proc.391.102.2023**

Salimullah, A.R.M., and Stow, D.A.V., 1992. Application of FMS images in poorly recovered coring intervals; examples from ODP Leg 129. In Hurst, A., Griffiths, C.M., and Worthington, P.F. (Eds.), Geological Applications of Wireline Logs II. Geological Society Special Publication, 65: 71–86. **https://doi.org/10.1144/GSL.SP.1992.065.01.06**

Samtleben, C., 1980. Die Evolution der Coccolithophoriden-Gattung Gephyrocapsa nach Befunden im Atlantik. Paläontologische Zeitschrift, 54(1):91–127. **https://doi.org/10.1007/BF02985885**

Sánchez Goñi, M.F., Desprat, S., Fletcher, W.J., Morales-Molino, C., Naughton, F., Oliveira, D., Urrego, D.H., and Zorzi, C., 2018. Pollen from the deep-sea: a breakthrough in the mystery of the ice ages. Frontiers in Plant Science, 9. **https://doi.org/10.3389/fpls.2018.00038**

Scherer, R.P., Gladenkov, A.Y., and Barron, J.A., 2007. Methods and applications of Cenozoic marine diatom biostratigraphy. The Paleontological Society Papers, 13: 61–83. **https://doi.org/10.1017/S1089332600001467**

Scherer, R.P., Sjunneskog, C.M., Iverson, N.R., and Hooyer, T.S., 2004. Assessing subglacial processes from diatom fragmentation patterns. Geology, 32(7):557–560. **https://doi.org/10.1130/G20423.1**

Schlumberger, 1989. Log Interpretation Principles/Applications, SMP-7017: Houston (Schlumberger Education Services).

Schlumberger, 1994. IPL Integrated Porosity Lithology, SMP-9270: Houston (Schlumberger Education Services).

Schmidt, D.N., Thomas, E., Authier, E., Saunders, D., and Ridgwell, A., 2018. Strategies in times of crisis—insights into the benthic foraminiferal record of the Palaeocene–Eocene Thermal Maximum. Philosophical Transactions of the Royal Society A: Mathematical Physical and Engineering Sciences, 376(2130):20170328. **https://doi.org/10.1098/rsta.2017.0328**

Schrader, H., and Gersonde, R., 1978. Diatoms and silicoflagellates. In Zachariasse, W.J., Riedel, W.R., Sanfilippo, A., Schmidt, R.R., Brolsma, M.J., Schrader, H.J., Gersonde, R., Drooger, M.M., and Broekman, J.A. (Eds.), Micropaleontological Counting Methods and Techniques: an Exercise on an Eight Metres Section of the Lower Pliocene of Capo Rossello, Sicily. Utrecht Micropaleontological Bulletin, 17: 129–176.

Serra, O., 1984. Fundamentals of Well-log Interpretation: The acquisition of logging data: (Elsevier).
Serra, O., 1986. Fundamentals of Well-Log Interpretation (Volume 2): The Interpretation of Logging Data: Amsterdam (Elsevier).
Serra, O., 1989. Formation MicroScanner Image Interpretation: Houston (Schlumberger Education Services).
Shepard, F.P., 1954. Nomenclature based on sand-silt-clay ratios. Journal of Sedimentary Research, 24(3):151–158. **https://doi.org/10.1306/D4269774-2B26-11D7-8648000102C1865D**
Shackleton, N.J., Crowhurst, S.J., Weedon, G.P., and Laskar, J., 1999. Astronomical calibration of Oligocene–Miocene time. In Shackleton N.J., McCave, I.N., and Graham, P.W. (Eds.), Astronomical (Milankovitch) Calibration of the Geological Time-Scale. Philos. Trans. R. Soc., Ser. A., 357(1757):1907–1929. **https://doi.org/10.1098/rsta.1999.0407**
Shipboard Scientific Party, 1993. Explanatory notes. In Rea, D.K., Basov, I.A., Janecek, T.R., Palmer-Julson, A., et al., Proceedings of the Ocean Drilling Program, Initial Reports. 145: College Station, TX (Ocean Drilling Program), 9–33. **https://doi.org/10.2973/odp.proc.ir.145.104.1993**
Shipboard Scientific Party, 1995. Leg 154 synthesis. In Curry, W.B., Shackleton, N.J., Richter, C, et al., Proceedings of the Ocean Drilling Program, Initial Reports. 154: College Station, TX (Ocean Drilling Program), 421–442. **https://doi.org/10.2973/odp.proc.ir.154.109.1995**
Shipboard Scientific Party, 1998. Explanatory notes. In Norris, R.D., Kroon, D., Klaus, A., et al., Proceedings of the Ocean Drilling Program, Initial Reports. 171B: College Station, TX (Ocean Drilling Program), 11–44. **https://doi.org/10.2973/odp.proc.ir.171B.102.1998**
Shipboard Scientific Party, 2000. Leg 182 summary: Great Australian Bight—Cenozoic cool-water carbonates. In Feary, D.A., Hine, A.C., Malone, M.J., et al., Proceedings of the Ocean Drilling Program, Initial Reports, 182. College Station, TX (Ocean Drilling Program). **https://doi.org/10.2973/odp.proc.ir.182.101.2000**
Shipboard Scientific Party, 2002. Leg 199 summary. In Lyle, M., Wilson, P.A., Janecek, T.R., et al., Proceedings of the Ocean Drilling Program, Initial Reports. 199: College Station, TX (Ocean Drilling Program). **https://doi.org/10.2973/odp.proc.ir.199.101.2002**
Shipboard Scientific Party, 2003a. Explanatory notes. In Wilson, D.S., Teagle, D.A.H., Acton, G.D., et al., Proceedings of the Ocean Drilling Program, Initial Reports. 206: College Station, TX (Ocean Drilling Program). **https://doi.org/10.2973/odp.proc.ir.206.102.2003**
Shipboard Scientific Party, 2003b. Leg 202 summary. In Mix, A.C., Tiedemann, R., Blum, P., et al., Proceedings of the Ocean Drilling Program, Initial Reports. 202: College Station, TX (Ocean Drilling Program). **https://doi.org/10.2973/odp.proc.ir.202.101.2003**
Sissingh, W., 1977. Biostratigraphy of Cretaceous calcareous nannoplankton. Geologie en Mijnbouw, 56:37–65.
Skilling, I.P., White, J.D.L., and McPhie, J., 2002. Peperite: a review of magma–sediment mingling. Journal of Volcanology and Geothermal Research, 114(1–2):1–17. **https://doi.org/10.1016/S0377-0273(01)00278-5**
Sluijs, A., Pross, J., and Brinkhuis, H., 2005. From greenhouse to icehouse; organic-walled dinoflagellate cysts as paleoenvironmental indicators in the Paleogene. Earth-Science Reviews, 68(3):281–315. **https://doi.org/10.1016/j.earscirev.2004.06.001**
Stow, D.A.V., 2005. Sedimentary Rocks in the Field. A Colour Guide: London (Manson Publishing).
Su, X., 1996. Development of late Tertiary and Quaternary coccolith assemblages in the Northeast Atlantic [PhD dissertation]. Christian-Albrechts-Universitä, Kiel, Germany. **https://doi.org/10.3289/GEOMAR_Report_48_1996**
Sutherland, R., Dickens, G.R., Blum, P., Agnini, C., Alegret, L., Asatryan, G., Bhattacharya, J., Bordenave, A., Chang, L., Collot, J., Cramwinckel, M.J., Dallanave, E., Drake, M.K., Etienne, S.J.G., Giorgioni, M., Gurnis, M., Harper, D.T., Huang, H.-H.M., Keller, A.L., Lam, A.R., Li, H., Matsui, H., Morgans, H.E.G., Newsam, C., Park, Y.-H., Pascher, K.M., Pekar, S.F., Penman, D.E., Saito, S., Stratford, W.R., Westerhold, T., and Zhou, X., 2019. Expedition 371 methods. In Sutherland, R., Dickens, G.R., Blum, P., and the Expedition 371 Scientists, Tasman Frontier Subduction Initiation and Paleogene Climate. Proceedings of the International Ocean Discovery Program, 371: (International Ocean Discovery Program). **https://doi.org/10.14379/iodp.proc.371.102.2019**
Tauxe, L., 2010. Essentials of Paleomagnetism: Oakland, CA (University of California Press).
Theodoridis, S., 1984. Calcareous nannofossil biozonation of the Miocene and revision of the helicoliths and discoasters [PhD dissertation]. Christian-Albrechts-Universitä, Kiel, Germany. **https://dspace.library.uu.nl/handle/1874/205891**
Thierstein, H.R., Geitzenauer, K.R., Molfino, B., and Shackleton, N.J., 1977. Global synchroneity of late Quaternary coccolith datum levels Validation by oxygen isotopes. Geology, 5(7):400–404. **https://doi.org/10.1130/0091-7613(1977)5<400:GSOLQC>2.0.CO;2**
Turco, E., Bambini, A.M., Foresi, L., Iaccarino, S., Lirer, F., Mazzei, R., and Salvatorini, G., 2002. Middle Miocene high-resolution calcareous plankton biostratigraphy at Site 926 (Leg 154, equatorial Atlantic Ocean): palaeoecological and palaeobiogeographical implications. Geobios, 35:257–276. **https://doi.org/10.1016/S0016-6995(02)00064-5**
Vacquier, V., 1985. The measurement of thermal conductivity of solids with a transient linear heat source on the plane surface of a poorly conducting body. Earth and Planetary Science Letters, 74(2–3):275–279. **https://doi.org/10.1016/0012-821X(85)90027-5**
van Andel, T.H., and Ballard, R.D., 1979. The Galapagos Rift at 86°W: 2. Volcanism, structure, and evolution of the Rift Valley. Journal of Geophysical Research: Solid Earth, 84(B10):5390–5406. **https://doi.org/10.1029/JB084iB10p05390**
Van Morkhoven, F.M., Berggren, W.A., and Edwards, A.S., 1986. Cenozoic cosmopolitan deep-water benthic foraminifera. Bulletin des centres de Recherches exploration-production elf-aquitaine, 11.
van Sprang, H.A., 2000. Fundamental parameter methods in XRF spectroscopy. Advances in X-ray Analysis, 42:1–10.

Vasiliev, M.A., Blum, P., Chubarian, G., Olsen, R., Bennight, C., Cobine, T., Fackler, D., Hastedt, M., Houpt, D., Mateo, Z., and Vasilieva, Y.B., 2011. A new natural gamma radiation measurement system for marine sediment and rock analysis. Journal of Applied Geophysics, 75(3):455–463. **https://doi.org/10.1016/j.jappgeo.2011.08.008**

Villa, G., Fioroni, C., Pea, L., Bohaty, S., and Persico, D., 2008. Middle Eocene–late Oligocene climate variability: calcareous nannofossil response at Kerguelen Plateau, Site 748. Marine Micropaleontology, 69(2):173–192. **https://doi.org/10.1016/j.marmicro.2008.07.006**

Voigt, S., Gale, A.S., Jung, C., and Jenkyns, H.C., 2012. Global correlation of Upper Campanian - Maastrichtian successions using carbon-isotope stratigraphy: development of a new Maastrichtian timescale. Newsletters on Stratigraphy, 45(1):25–53. **https://doi.org/10.1127/0078-0421/2012/0016**

Von Herzen, R., and Maxwell, A.E., 1959. The measurement of thermal conductivity of deep-sea sediments by a needle-probe method. Journal of Geophysical Research, 64(10):1557–1563. **https://doi.org/10.1029/JZ064i010p01557**

von Salis, K., 1998. Calcareous nannofossils column for Triassic and Cretaceous charts, Mesozoic and Cenozoic sequence chronostratigraphic framework of European basins. In de Graciansky, P.-C., Hardenbol, J., Jacquin, T., and Vail, P.R. (Eds.), Mesozoic and Cenozoic Sequence Stratigraphy of European Basins. Special Publication - SEPM (Society for Sedimentary Geology), 60.

Wade, B.S., 2004. Planktonic foraminiferal biostratigraphy and mechanisms in the extinction of Morozovella in the late middle Eocene. Marine Micropaleontology, 51(1–2):23–38. **https://doi.org/10.1016/j.marmicro.2003.09.001**

Wade, B.S., Berggren, W.A., and Olsson, R.K., 2007. The biostratigraphy and paleobiology of Oligocene planktonic foraminifera from the equatorial Pacific Ocean (ODP Site 1218). Marine Micropaleontology, 62(3):167–179. **https://doi.org/10.1016/j.marmicro.2006.08.005**

Wade, B.S., Olsson, R.K., Pearson, P.N., Huber, B.T., and Berggren, W.A., 2018. Atlas of Oligocene Planktonic Foraminifera. Special Publication - Cushman Foundation for Foraminiferal Research, 46.

Wade, B.S., and Pearson, P.N., 2008. Planktonic foraminiferal turnover, diversity fluctuations and geochemical signals across the Eocene/Oligocene boundary in Tanzania. Marine Micropaleontology, 68(3–4):244–255. **https://doi.org/10.1016/j.marmicro.2008.04.002**

Wade, B.S., Pearson, P.N., Berggren, W.A., and Pälike, H., 2011. Review and revision of Cenozoic tropical planktonic foraminiferal biostratigraphy and calibration to the geomagnetic polarity and astronomical time scale. Earth-Science Reviews, 104(1–3):111–142. **https://doi.org/10.1016/j.earscirev.2010.09.003**

Wallace, P.J., 1998. Pre-eruptive H_2O and CO_2 contents of mafic magmas from the submarine to emergent shield stages of Gran Canaria. In Weaver, P.P.E., Schmincke, H.-U., Firth, J.V., and Duffield, W. (Eds.), Proceedings of the Ocean Drilling Program, Scientific Results. 157: College Station, TX (Ocean Drilling Program), 411–420. **https://doi.org/10.2973/odp.proc.sr.157.146.1998**

Warnock, J.P., and Scherer, R.P., 2015. Diatom species abundance and morphologically-based dissolution proxies in coastal Southern Ocean assemblages. Continental Shelf Research, 102:1–8. **https://doi.org/10.1016/j.csr.2015.04.012**

Watkins, D.K., 1992. Upper Cretaceous nannofossils from Leg 120, Kerguelen Plateau, Southern Ocean. In Wise, S.W., Jr., Schlich, R., et al., Proceedings of the Ocean Drilling Program, Scientific Results. 120: College Station, TX (Ocean Drilling Program), 343–370. **https://doi.org/10.2973/odp.proc.sr.120.180.1992**

Watkins, D.K., and Guerra, R.M., 2020. Calcareous nannofossils from the Great Australian Bight (IODP Site U1512) as a record of the peak and early decline of the mid-Cretaceous super greenhouse. Marine Micropaleontology, 158:101893. **https://doi.org/10.1016/j.marmicro.2020.101893**

Watkins, D.K., Wise, S.W., Jr., Popsichal, J.J., and Crux, J., 1996. Upper Cretaceous calcareous nannofossil biostratigraphy and paleoceanography of the Southern Ocean. Presented at the Microfossils and Oceanic Environments, Aberstwyth, Wales, 19–21 April 1994.

Wei, W., 1993. Calibration of Upper Pliocene-Lower Pleistocene nannofossil events with oxygen isotope stratigraphy. Paleoceanography and Paleoclimatology, 8(1):85–99. **https://doi.org/10.1029/92PA02504**

Wei, W., and Thierstein, H.R., 1991. Upper Cretaceous and Cenozoic calcareous nannofossils of the Kerguelen Plateau (southern Indian Ocean) and Prydz Bay (East Antarctica). In Barron, J., Larsen, B., et al., Proceedings of the Ocean Drilling Program, Scientific Results. 119: College Station, TX (Ocean Drilling Program), 467–493. **https://doi.org/10.2973/odp.proc.sr.119.165.1991**

Wentworth, C.K., 1922. A scale of grade and class terms for clastic sediments. The Journal of Geology, 30(5):377–392. **https://doi.org/10.1086/622910**

White, J.D.L., Bryan, S.E., Ross, P.-S., Self, S., and Thordarson, T., 2009. Physical volcanology of continentallarge igneous provinces. In Thordarson, T., Self, S., Larsen, G., Rowland, S.K., and Hoskuldsson, A., (Eds.), Studies in Volcanology: The Legacy of George Walker. Special Publications of IAVCEI, 2: 291–321.

Wickham, H., Averick, M., Bryan, J., Chang, W., D'Agostino McGowan, L., François, R., Grolemund, G., Hayes, A., Henry, L., Hester, J., Kuhn, M., Lin Pedersen, T., Miller, E., Milton Bache, S., Müller, K., Ooms, J., Robinson, D., Seidel, D.P., Spinu, V., Takahashi, K., Vaughan, D., Wilke, C., Woo, K., and Yutani, H., 2019. Welcome to the Tidyverse. Journal of Open Source Software, 4(43):1686. **https://doi.org/10.21105/joss.01686**

Williams, G.L., Brinkhuis, H., Pearce, M.A., Fensome, R.A., and Weegink, J.W., 2004. Southern Ocean and global dinoflagellate cyst events compared; index events for the Late Cretaceous-Neogene. In Exon, N.F., Kennett, J.P., and Malone, M.J. (Eds.), Proceedings of the Ocean Drilling Program, Scientific Results. 189: College Station, TX (Ocean Drilling Program). **https://doi.org/10.2973/odp.proc.sr.189.107.2004**

Williams, G.L., Fensome, R.A., and MacRae, R.A., 2017. The Lentin and Williams Index of Fossil Dinoflagellates 2017 Edition. AASP Contributions Series, 48. **https://palynology.org/contribution-series-number-48-the-new-lentin-and-williams-index-2017/**

Williams, G.L., Stover, L.E., and Kidson, E.J., 1993. Morphology and stratigraphic ranges of selected Mesozoic–Cenozoic dinoflagellate taxa in the Northern Hemisphere. Geological Survey of Canada Paper, 92-10. **https://doi.org/10.4095/183916**

Willumsen, P.S., 2012. Three new species of dinoflagellate cyst from Cretaceous–Paleogene (K-Pg) boundary sections at mid-Waipara River and Fairfield Quarry, South Island, New Zealand. Palynology, 36(sup1):48–62. **https://doi.org/10.1080/01916122.2011.642260**

Wise, S.W., Jr., 1988. Mesozoic-cenozoic history of calcareous nannofossils in the region of the southern ocean. Palaeogeography, Palaeoclimatology, Palaeoecology, 67(1–2):157–179. **https://doi.org/10.1016/0031-0182(88)90127-7**

Young, J.R., 1998. Neogene nannofossils. In Bown, P.R., Calcareous Nannofossil Biostratigraphy. Dordrecht, The Netherlands (Kluwer Academic Publishing), 225–265.

Young, J.R., Bown, P.R., and Lees, J.A., 2022. Nannotax3 website. International Nannoplankton Association. **https://www.mikrotax.org/Nannotax3**

Zeeden, C., Hilgen, F., Westerhold, T., Lourens, L., Röhl, U., and Bickert, T., 2013. Revised Miocene splice, astronomical tuning and calcareous plankton biochronology of ODP Site 926 between 5 and 14.4Ma. Palaeogeography, Palaeoclimatology, Palaeoecology, 369:430–451. **https://doi.org/10.1016/j.palaeo.2012.11.009**

Zielinski, U., and Gersonde, R., 2002. Plio-Pleistocene diatom biostratigraphy from ODP Leg 177, Atlantic sector of the Southern Ocean. Marine Micropaleontology, 45(3–4):225–268. **https://doi.org/10.1016/S0377-8398(02)00031-2**

Zonneveld, K.A.F., Marret, F., Versteegh, G.J.M., Bogus, K., Bonnet, S., Bouimetarhan, I., Crouch, E., de Vernal, A., Elshanawany, R., Edwards, L., Esper, O., Forke, S., Grøsfjeld, K., Henry, M., Holzwarth, U., Kielt, J.-F., Kim, S.-Y., Ladouceur, S., Ledu, D., Chen, L., Limoges, A., Londeix, L., Lu, S.H., Mahmoud, M.S., Marino, G., Matsouka, K., Matthiessen, J., Mildenhal, D.C., Mudie, P., Neil, H.L., Pospelova, V., Qi, Y., Radi, T., Richerol, T., Rochon, A., Sangiorgi, F., Solignac, S., Turon, J.-L., Verleye, T., Wang, Y., Wang, Z., and Young, M., 2013. Atlas of modern dinoflagellate cyst distribution based on 2405 data points. Review of Palaeobotany and Palynology, 191:1–197. **https://doi.org/10.1016/j.revpalbo.2012.08.003**